Measuring and characterizing ultrafast quantum states using nanophotonic optical parametric amplifiers

Thesis by
Elina Maria Sendonaris

In Partial Fulfillment of the Requirements for the
Degree of
Doctor of Philosophy

CALIFORNIA INSTITUTE OF TECHNOLOGY
Pasadena, California

2026
Defended May 26, 2026

Elina Maria Sendonaris
ORCID: 0009-0003-4209-2783

ACKNOWLEDGEMENTS

This thesis would not be possible, or in remotely as good of a shape as it is currently, without the support of my colleagues, friends, and family, and for that I am extremely grateful.

I would first like to acknowledge my colleagues for their help in learning the field of quantum optics. James Williams is an experimental wizard who showed me that everything can be automated, and he taught me the benefits both of patience and dedication and of thinking outside the box when determination alone was not enough. His expertise in electrical engineering and vacuum systems was invaluable in our work together, and I thank him for being patient with me as I asked interminable questions about experimental setups. His work outside the lab on organizing the graduate student union showed me just how much a small group of dedicated people can change the lives of many for the better, and it has inspired me to try to bring about even a fraction of that positive change. He was there with me through thick and thin during our time at the Nonlinear Photonics Lab, and I am truly grateful to call him not only a colleague but also a friend. Thomas Zacharias is another colleague and friend that I am thankful to have shared my time in the lab with. His dedication to doing meaningful research that is impactful to other researchers is truly admirable and has helped me re-contextualize much of my work. I also thank him for challenging me in my assumptions and being willing to have long discussions so that I can arrive at a better understanding of everything from matrix formulations of equations to AI ethics. I am also grateful to spend time hiking and camping with him which has helped maintain a semblance of work-life balance.

Another colleague with whom I share both an office and hikes with is Rithvik Ramesh, and his calmness and commitment to positivity has inspired me to face adversity with a similar grace. Max Shen's and Arda Deger's willingness to go skiing at an alarmingly high rate is always appreciated. I have to also thank Rajveer Nehra for teaching me almost everything I know about continuous-variable quantum optics and aligning to chips in the lab. Nico Englebert's mentorship and support has helped me gain a clearer picture of academia and given me a role model of how to be a successful mentor in a lab. I also have to thank Ben Gutierrez, my cohort-mate in the lab, for always being willing to lend a sympathetic ear. My colleagues and successors in the quantum subgroup, Ofir Yesharim and Po Han Wang, have already made so much progress in less than a year that I can't wait to see where they go; I'm sure they will achieve great things. My other colleagues through the years, Arkhadev Roy, Luis Ledezma, Luis Costa, Qiushi Guo, Midya Parto, Christian Leefmans, Mingchen Liu, Robert Gray, Selina Zhou, Gordon Li, Yingchu Xu, Justin Widjaja, and Yiting Wang, Eleanor Kim, Shivam Mundhra, Rahul Chawlani, Jennifer Solgaard, Parthorn Ammawat, Adelynn Tang, and Louise Schul have taught me perhaps more than they know, and their advice and company is one of the biggest reasons that this thesis exists.

I have to of course also thank my advisor, Prof. Alireza Marandi, for helping me along the path to becoming an independent researcher. His insights and commitment to telling a story with the research have taught me a lot about academia and how to communicate effectively. I thank him for letting me bring a dose of quantum optics and theory to his group, and I learned quite a bit about research at the small- and large-scale level from him.

My mentors from before my time at Caltech are the reason I have made it this far. Jamison Sloan has been a constant mentor and friend, and I thank him for teaching me how to write a CLEO abstract and make figures with reasonable color schemes. I admire Nicholas Rivera's creativity and ability to understand any concept that I was trying to convey, no matter in how convoluted a fashion. Their support during the pandemic and after and push for me to reapply to graduate school got me to where I am today. I will be forever grateful for Prof. Marin Soljačić's support and taking me as a research assistant at that crucial point in my research career. My undergrad research with Prof. Aram Harrow introduced me to research in quantum information theory and allows me to at least partially comprehend theory papers, for which I am also grateful. I would also like to thank the kind folks at PsiQuantum for taking a chance on me and giving me an internship when I knew almost nothing about quantum optics, including Jeremy O'Brien and my mentors Mihai Vidrighin, Alessandro Farsi, and Dylan Saunders for believing in me and teaching me about theoretical and experimental quantum photonics. A summer research project in Prof. James Fujimoto's lab placed me on the path towards optics research that has culminated in this thesis, so I have to thank him for giving me that opportunity.

I am beyond appreciative of all the friends I've made during my time at Caltech. I thank Catherine Felce for being my friend from day one and for being there for me through every possible high and low that graduate school can throw at us. We may be an ocean apart, but her love and support is still with me and kept me going more times than I can count. I also thank Su Direkci for her constant friendship, dry humor, honesty, and letting me play with her cat. I am shocked that she let me convince her to go camping (twice!), and I appreciate that greatly. I appreciate Elie Bataille for being an adventure partner and being down for all kinds of outdoorsy trips. Thank you to Ina Sorensen for introducing me to aerial silks and improving my finger strength so I can type this thesis more effectively. My bandmates, Tal Hershko, Liam Ordner, Ray Wynne, and Tommy Sievert, all provided such a great creative outlet in the form of playing and creating music, and I'm going to sorely miss our jam sessions and Mag House Tuesdays.

Last but certainly not least I have to thank my parents, Asta and Andrew Sendonaris, without whom this thesis would not be possible. Their love and support has kept me going, not to mention their practical advice and home-cooked food. Thank you so much for everything you've done for me.

ABSTRACT

Photonics offers the potential for large-scale, room-temperature, and ultrafast quantum operations. Multiplexing pulses of light allows for high throughput speeds and dense encoding, with tens of thousands of optical modes being present in a time as short as a microsecond. However, the measurement speed of electronic devices such as photodetectors is currently one bottleneck in such time-multiplexed scalability, because many quantum optical protocols rely on measurement, including state preparation, feed-forward, and feedback. Furthermore, characterization of quantum states and modes is essential for their effective use. Using nanophotonic optical parametric amplifiers (OPAs) presents one way to circumvent the measurement limitations of current quantum photonic schemes. Their large amplification bandwidth, enabled by dispersion engineering on nanophotonic integrated platforms, allows information encoded in femtosecond-scale, THz-bandwidth, multimode quantum optical states to be accessed with nonlinear optical interactions.

In this work, we show how ultra-broadband integrated nanophotonic OPAs can be used to measure ultrafast and multimode quantum states of light. First, we explore the single-photon detection capabilities of OPAs, showing that current OPAs operating in the Gaussian regime are capable of 250 MHz photon count rates with 26% efficiency and a 2% dark count probability. We also show how non-Gaussian operation through pump depletion, with performance that approaches state-of-the-art photon detectors in terms of efficiency and dark count rate while retaining ultrafast operation, can become experimentally possible with a higher nonlinear coupling rate and lower loss. Next, we use nanophotonic OPAs to both generate and characterize multimode ultrafast squeezed vacuum. We use the photocurrent distribution of amplified squeezed vacuum to recover 2.41 dB of squeezing in one mode of a 154-fs multimode squeezed pulse and reconstruct its Wigner distribution. Finally, we investigate the capabilities of broadband nanophotonic OPAs to determine the temporal mode structure and quadrature variances of ultra-broadband temporally multimode quantum states by adapting frequency-resolved optical gating to the quantum regime. We numerically show the successful full characterization of a multimode squeezed state, even in the presence of noise. Together, these results establish OPAs as a valuable measurement device for measuring ultrafast quantum pulses and learning the structure of multimode quantum states, and they provide one building block towards a framework for scalable continuous-variable quantum photonics in which state generation, manipulation, and characterization occur within the same nanophotonic platform.

PUBLISHED CONTENT AND CONTRIBUTIONS

[1] Elina Sendonaris, Thomas Zacharias, Robert Gray, James Williams, and Alireza Marandi. *Frequency resolved optical gating using parametric amplification for characterizing ultrafast temporally multimode squeezed states*. Apr. 9, 2026. DOI: 10.48550/arXiv.2604.08717. arXiv: 2604.08717[quant-ph].
E.S. participated in the conception of the project, performed the theoretical and numerical analysis, and wrote the manuscript.

[2] Elina Sendonaris*, James Williams*, Rajveer Nehra, Robert Gray, Ryoto Sekine, Luis Ledezma, and Alireza Marandi. "Ultrafast single-photon detector based on a nanophotonic parametric amplifier". In: *Physical Review Applied* 25.4 (Apr. 27, 2026), p. 044078. DOI: 10.1103/c58l-h1gh.
E.S. participated in the conception of the project, performed the theoretical and numerical analysis, performed the experiments, analyzed the data, and wrote the manuscript.

[3] Thomas Zacharias, Elina Sendonaris, Robert Gray, James Williams, Ryoto Sekine, Maximilian Shen, Selina Zhou, and Alireza Marandi. *Quantum Frequency Resolved Optical Gating of Few-Cycle Squeezed Vacuum*. Apr. 8, 2026. DOI: 10.48550/arXiv.2604.07637. arXiv: 2604.07637[physics.optics].
E.S. assisted with the theoretical analysis.

[4] Shivam Mundhra, Elina Sendonaris, Robert M. Gray, James Williams, and Alireza Marandi. *Optimizing for a Near Single-Mode Type-0 Optical Parametric Amplifier in Nanophotonics*. Jan. 6, 2025. DOI: 10.48550/arXiv.2412.07004. arXiv: 2412.07004[physics.optics].
E.S. participated in the conception of the project and assisted with the numerical analysis and writing of the manuscript.

[5] Elina Sendonaris, James Williams, Rajveer Nehra, Robert Gray, Ryoto Sekine, Luis Ledezma, and Alireza Marandi. "Quantum detector tomography of ultrafast nanophotonic parametric amplifiers single photon detector". In: *SMT 2025*. APS, 2025.
E.S. participated in the conception of the project, performed the theoretical and numerical analysis and experiments and analyzed the experimental data.

[6] Elina Sendonaris, Thomas Zacharias, Robert Gray, James Williams, and Alireza Marandi. "Characterizing a Temporally Multimode Squeezed State Using Frequency Resolved Optical Gating". In: *2025 Conference on Lasers and Electro-Optics (CLEO)*. 2025 Conference on Lasers and Electro-Optics (CLEO). ISSN: 2160-8989. May 2025, pp. 1–2.
E.S. participated in the conception of the project and performed the theoretical and numerical analysis.

[7] James Williams*, Elina Sendonaris*, Rajveer Nehra, Robert M. Gray, Ryoto Sekine, Luis Ledezma, and Alireza Marandi. "Ultrafast all-optical measurement of squeezed vacuum in a lithium niobate nanophotonic circuit". In: *Physical Review Research* 7.4 (Oct. 1, 2025), p. 043006. DOI: 10.1103/rvmb-ljd3.
E.S. performed the theoretical analysis and assisted with the data analysis.

[8] Thomas Zacharias, Robert Gray, Elina Sendonaris, James Williams, Maximilian Shen, Selina Zhou, and Alireza Marandi. "Temporal Characterization of Ultrashort-Pulse Squeezed Vacuum Using Frequency Resolved Optical Gating". In: *2025 Conference on Lasers and Electro-Optics (CLEO)*. 2025 Conference on Lasers and Electro-Optics (CLEO). ISSN: 2160-8989. May 2025, pp. 1–2.
E.S. assisted with the theoretical analysis.

[9] James Williams, Rajveer Nehra, **Sendonaris, Elina**, Luis Ledezma, Robert M. Gray, Ryoto Sekine, and Alireza Marandi. "Ultrashort pulse biphoton source in lithium niobate nanophotonics at 2 μm". In: *Nanophotonics* 13.18 (Aug. 1, 2024), pp. 3535–3544. DOI: 10.1515/nanoph-2024-0054.
E.S. assisted with the data analysis.

[10] Elina Sendonaris, Rajveer Nehra, James Williams, Robert Gray, Luis Ledezma, Ryoto Sekine, and Alireza Marandi. "Toward Single Photon Detection using Nanophotonic Parametric Amplifiers". In: *CLEO 2023*. CLEO: Fundamental Science. San Jose, CA: Optica Publishing Group, 2023, FTh3A.5. DOI: 10.1364/CLEO_FS.2023.FTh3A.5.
E.S. participated in the conception of the project, performed the theoretical and numerical analysis and experiments and analyzed the experimental data.

TABLE OF CONTENTS

LIST OF ILLUSTRATIONS

NOMENCLATURE

BPF. Band-pass filter.

CV. Continuous variable.

DV. Discrete variable.

FC. Fiber coupler.

FROG. Frequency-resolved optical gating.

GKP state. Gottesman-Kitaev-Preskill state.

GVD. Group velocity dispersion.

GVM. Group velocity mismatch.

HD. Homodyne detector.

JSA. Joint spectral amplitude.

JSI. Joint spectral intensity.

LN. Lithium niobate.

LP. Long-pass wavelength filter.

LPF. Low-pass filter.

MLL. Mode-locked laser.

MMG. Multimode Gaussian.

MMG-OPA-FROG. Multimode Gaussian optical parametric amplifier frequency-resolved optical gating.

OPA. Optical parametric amplifier.

OPAD. OPA detector.

OPG. Optical parametric generation.

OPO. Optical parametric oscillator.

OSA. Optical spectrum analyzer.

PBS. Polarizing beamsplitter.

PD. Photodetector.

PDC. Parametric down-conversion.

PMMA. Poly methyl methacrylate.

POVM. Positive operator-valued measure.

PVM. Projection valued measure.

QIP. Quantum information processing.

QND. Quantum non-demolition.

SNR. Signal-to-noise ratio.

SNSPD. Superconducting nanowire single photon detector.

SP. Short-pass wavelength filter.

SPAD. Single-photon avalanche diode.

SPDC. Spontaneous parametric down-conversion.

SV. Squeezed vacuum.

SVD. Singular value decomposition.

TES. Transition-edge sensor.

TFLN. Thin-film lithium niobate.

VND. Variable neutral density filter.

Chapter 1

INTRODUCTION

It is not clear which technology will pull ahead in the race towards useful quantum computers, and it is not clear whether only one technology will be used. However, in many if not all current quantum technologies, light plays a role, be it to control atoms, measure qubits, or communicate quantum information and distribute entanglement. Thus, improving the generation and measurement of quantum light will have far-reaching benefits for all quantum technologies, not only those based on light itself. This thesis will explore one building block in a quantum optical infrastructure, ultrafast all-optical quantum measurement, which may prove beneficial for photonic quantum computation and, more broadly, for any system that makes use of quantum light.

1.1 Nonlinear quantum optics

The benefits of using light with quantum properties such as squeezing and entanglement are many, including higher sensitivity while sensing [16, 49, 84], more efficient and secure communication [40, 67, 100], and the potential to perform calculations that would be infeasible using classical computers [54, 101]. Many quantum technologies rely on light for control, measurement, and communication. Light as an information carrier has the benefit that it does not interact as much with the environment as matter-based quantum states, and thus can be used at room temperature and atmospheric pressure without the need for vacuum chambers or cryostats. Furthermore, the fact that it travels at a high speed makes it the carrier of choice for quantum communication [40] and enables the packing of quantum information in a short time-frame through time multiplexing [5, 47]. In addition, light has many degrees of freedom available to it, such as polarization [14, 35, 45, 56], spatial modes [8], and frequency modes [34]. All in all, photonics is attractive because it combines room-temperature operation, compatibility with communication networks, and access to large Hilbert spaces through multiple optical degrees of freedom.

However, light's low interaction strength with the environment and itself leads to the issue of reliably and deterministically enacting nonlinear operations and creating the states needed for universal quantum computation. There have been many works which deal with the issue of probabilistic state production and gate operation [9, 43, 46, 66], which is typical of working with single photons and their detection (although research into quantum dots is focused on their ability to generate single photons on-demand [33, 61, 76, 87]). One option for deterministic quantum light manipulation is to use nonlinear optical elements to mediate interactions between photons, generating such states as squeezed states, which are the most commonly generated and utilized quantum optical state exclusively using nonlinear optical interactions [16, 62, 88]. Squeezed states can be generated through parametric down-conversion (PDC), a process by which one photon splits into two photons whose frequencies add up to that of the original photon. Degenerate spontaneous PDC generates squeezed vacuum, which has noise in one quadrature that is less than that of vacuum. Squeezed states are important for quantum communication, sensing, and computation because of the reduced noise and the generation of entangled states by sending two of them into a beamsplitter, which can be used for generating large entangled states called cluster states [5, 47, 60]. The reduced noise is useful for lowering the noise in optical detections which have an open vacuum port, such as in heterodyne detection or other interferometers such as those used for gravitational wave detection [17, 84].

Nonlinear optical interactions are one of the most common ways of generating photons, by heralding a photon detection on one arm after splitting up a low-amplitude squeezed state, which contains mostly vacuum and a two-photon term [20, 57, 79, 90]. Unfortunately, squeezed states and second-order nonlinear interactions are insufficient for universal quantum computing, and a higher-order nonlinear interaction or a non-Gaussian operation such as single-photon detection is necessary to obtain an advantage over classical computers [58]. Nevertheless, improving squeezed state and other Gaussian state generation and characterization will lead to advances in quantum optical sensing, communication, and information processing due to their utility for generating large entangled states deterministically and for noise reduction [5, 47, 49, 54, 94, 95].

1.2 The case for ultrafast multimode quantum light

Ultrafast quantum light encompasses short pulses with lengths on the order of femtoseconds to hundreds of femtoseconds. They allow for a high peak power while retaining a low average power. In nonlinear optical processes, since the efficiency of the interaction scales nonlinearly with the peak power, pulses enable efficient processes while avoiding damage to the nonlinear crystal. A main consideration while using ultrashort pulses is their extremely broad bandwidth, which allows for high temporal resolution but requires the dispersion in the nonlinear material to be low for the pump pulse to retain its shape and the nonlinear process to be phase-matched throughout the bandwidth [50].

The usefulness of ultrafast classical light has led to an interest in ultrafast and attosecond quantum light [23]. For example, the fluctuations of the quantum vacuum have been probed with subcycle resolution using electro-optic sampling [42, 72], and attosecond squeezed high-harmonic pulses have been generated using bright squeezed vacuum as the pump [85, 86]. Generating ultrashort quantum pulses is also possible in broadband optical parametric amplifiers (OPAs), a nonlinear device whose broad phase-matching bandwidth allows for squeezed light to be generated across a large frequency range [50, 80]. These devices must be pumped by ultrashort pulses in order to take advantage of this broad bandwidth, and when this is done, the modes in which this squeezed light is generated can have bandwidths in the tens of THz range.

OPAs are commonly integrated into photonic chips that move light along nonlinear waveguides in which the light is tightly confined [12, 50, 102]. The shape of the waveguide controls the frequency-dependent dispersion, allowing for matching of group velocity between different wavelengths and minimization of higher-order dispersion. The preservation of the shape of ultra-short broadband pulses is crucial for achieving broadband and high-amplitude gain [50]. Integrated nonlinear optical components also have the benefits of scalable manufacturing and higher nonlinear efficiency due to the spatial confinement [95, 96]. Much work is being done to integrate entire circuits and optical setups, including detectors, onto photonic chips for these reasons, which has the benefit of circumventing the optical loss that comes with coupling the light out of the chip [22, 26, 46, 83]

Thin-film lithium niobate (TFLN) is a particularly popular material due to its high second-order nonlinear and electro-optic coefficients and increasingly large variety of available integrated devices, in addition to its favorable dispersion engineering capabilities and low propagation loss [25, 51, 102]. Thus, it is the ideal platform for ultrafast quantum optics, with its large bandwidth enabling both generation and measurement of ultrafast quantum light, and its large gain (over 100 dB/cm in some cases [50]) amplifying the entire bandwidth of the state to a macroscopically detectable level. The high gain and favorable dispersion allow for the on-chip measurement of squeezing, for example in [62].

Using broadband squeezed states for optical quantum communication and computation is one path towards THz clock rates in these domains. By having shorter pulses, it is possible to pack more pulses in a shorter time, which opens new paths for larger-scale computations using large entangled states. For example, the biggest continuous-variable

(CV) cluster states that have been created using squeezed states are made in the time-multiplexed basis [5, 47], and their size is limited by the phase stability of the setups as their sensitive alignment worsens over short timescales. Making the nodes closer together in time would allow the size of the cluster state to increase dramatically without improving the setup at all.

Another option for increasing the size of cluster states is to combine the time-multiplexed dimension with another degree of freedom, such as spectrotemporal modes. Pulses of squeezed vacuum generated by broadband OPAs typically contain many spectrotemporal modes, which are orthogonal modes that are localized in time and frequency and overlap with each other in both, and they generally resemble Hermite-Gaussian functions [13]. These modes offer another degree of freedom, or synthetic dimension, for information to be encoded in and entanglement structures to be generated in. Synthetic dimensions are popular in optics because light has many degrees of freedom, such as polarization [14, 35, 45, 56], spatial modes [3, 8], and frequency [34, 89], many of which can be used in conjunction. Using these temporal modes concurrently with other information encodings, it is possible to scale up the amount of modes significantly by multiplicative factors of the number of modes in use, and to increase the dimensionality of the state. Currently, there already have been temporally multiplexed optical cluster states generated with tens of thousands of modes [5, 47], and including a temporal mode encoding in the setup can potentially increase the number of modes by an order of magnitude.

A multimode squeezed state, and indeed any multimode Gaussian state, has at least one basis in which the states are uncorrelated, called the principal basis, and measuring correlations in other bases shows correlations between the modes [30]. It is the basis in which the state consists of multiple squeezed or thermal modes. It is beneficial to measure a quantum state in its principal basis, if such a basis exists, because in other bases the entanglement with other modes causes thermalization and introduces noise when those modes are traced out [30]. For a multimode squeezed state, for example, the highest squeezing that can be measured of this state exists in the first principal mode [38, 63, 75].

Cluster states in the temporal mode basis have been generated by measuring multimode squeezed states in a non-principal basis [15, 73]. Finding this principal mode basis and characterizing the states in this basis is a crucial next step to take advantage of this synthetic dimension, but the same broad bandwidth and multimode structure that make these states useful also make them difficult to verify and control experimentally. The usefulness of ultrafast multimode quantum states therefore depends not only on generating them, but on identifying the basis in which their modal structure and quantum correlations can be taken advantage of best.

1.3 Quantum optical measurements

Measurements for characterizing quantum light range from characterizing the light in terms of its modal structure and state content, as mentioned above, to performing measurements during a quantum computation. For example, operating on an ultrafast quantum state in the measurement-based quantum computing scheme necessitates an ultrafast measurement that can measure one node of a cluster state [69]. Recently, ultrafast quantum teleportation has been implemented using an all-optical measurement scheme using OPAs to measure the quadrature correlations and feed them forward [81]. As another example, photon detection is commonly used to generate photons from a biphoton state [91] and to herald other non-Gaussian states through photon subtraction [44, 46, 65]. To generate an ultrafast non-Gaussian state, an ultrafast non-Gaussian operation is needed. In both of these cases, to achieve THz rates of operations in quantum optics and take advantage of ultrafast light's large bandwidth, such as gate operations in measurement-based quantum computing, THz-rate measurements, which can be achieved through optical means, are crucial.

Photon detection

While there are a variety of photon detection mechanisms, the most common ones today are single-photon avalanche diodes (SPADs) [18], superconducting nanowire single-photon detectors (SNSPDs) [29], and transition edge sensors (TESs) [53]. Each of these detectors works by the photon causing a qualitative change in a material (either causing an avalanche through impact ionization or breaking superconductivity through absorption of the photon). Due to this material change and the necessity to reset the change before the next photon detection, these detectors have both a timing jitter which causes uncertainty in the detection time and a longer reset or dead time during which no photons can be detected. These times come from fundamental physical limitations associated with the processes of absorption; for example, in an SNSPD, the theoretical physical limit for timing jitter is estimated to be 0.8 ps for current architectures [24].

The most important figures of merit for these detectors are the efficiency, which is the probability of detecting a photon given a photon arrived at the detector, and the dark count rate, or the rate of erroneous clicks given no photons incident on the detector.

These figures of merit determine the quality of non-Gaussianity which can be generated using these detectors and the rate at which it can be generated [44, 46, 65], in addition to determining the effectiveness of implementing quantum communication protocols [67] and showing quantum advantage in protocols such as Gaussian boson sampling [64]. Thus, these metrics have been optimized for, leading to SNSPDs reaching single-photon detection efficiencies of over 99% [19, 70] and dark count rates as low as 6×10^{-6} counts/s [21], with SPADs having slightly lower efficiencies and higher dark count rates [18]. Furthermore TESs have been reported with photon-number resolution of up to 100 photons [27].

These detectors have been optimized extremely well for their regimes of operation because of the importance of these metrics for practical applications. However, their timing jitter and dead time make them incompatible with ultrafast quantum operations in the THz regime. SPADs have been reported with count rates of 2.5 GHz [32] and SNSPDs with count rates in the GHz range [71, 99], but the dead times are limiting the speed of these detectors. One alternative to these detectors is to measure the photon using homodyne detection, which increases the amplitude of the signal optically through interaction with a local oscillator, and thus makes it possible to take advantage of the higher speeds of photodetectors relative to single photon detectors [31]. However, even the fastest photodetectors' bandwidths [52] pale in comparison to the bandwidths of the broadband OPAs which are being fabricated today in thin-film lithium niobate. Thus, an ultra-broadband, perhaps all-optical, measurement system is needed for measuring photons in this ultrafast regime.

Multimode pulsed measurements

There are both time-resolved methods for measuring multimode pulses of quantum light, such as electro-optic sampling [41, 72, 97], and mode-resolved characterization methods. We will focus here on the mode-resolved measurements, although a study of how multimode states respond to time-resolved measurements has been made [97], and one can view time-resolved measurements as measurements in the time-bin mode basis. Separating a multimode state into its constituent modes allows for operations on individual modes, allowing for computation in the spectrotemporal mode, also known as the supermode, basis [13, 38, 74, 77].

Homodyne detection with a shaped local oscillator is an extremely common way to measure the quadrature of a quantum state in a specific mode [15, 68, 73]. The shape of the mode which will be measured is determined by the local oscillator shape. This method has the benefit of amplifying the signal by a factor of the amplitude of the local oscillator and being inherently single-mode, as long as the local oscillator is single-mode as well. As mentioned above, measuring the nullifier of a temporal-mode cluster state involves measuring the quadrature variance of a combination of principal modes, which is done by shaping the local oscillator to be the linear combination of the modes which defines one node of a cluster state [5, 47]. Shaping the local oscillator is done with a pulse shaper, such as a spatial light modulator. The downside of using this method is that the resolution of the measurement is limited by the resolution of the pulse-shaping technique, and that for the optimal measurement results, the principal mode basis must be known in advance. It is possible to recover this basis by diagonalizing the covariance matrix from measurements in a non-principal basis [75], but, once again, the resolution of these recovered modes is determined by the pulse-shaping technique. Lastly, the bandwidth of the local oscillator and photodetectors limits the bandwidth of the modes and the rate at which the modes can be measured to GHz, although amplifying the state using a broadband OPA prior to detection can help circumvent the bandwidth restriction [80].

Diagonalizing the joint spectral amplitude, which is a measure of the correlations between the signal and idler photon emitted during PDC, is another way of determining the principal mode basis [79]. In the low-gain or biphoton regime, this technique requires single-photon spectrometers and knowledge of the complex phase of the pump pulse which was used to generate the squeezed state. Furthermore, for higher gain, it is necessary to measure the correlations of higher numbers of photons than just the signal and idler, which only requires two-photon coincidences.

Another way of splitting up a multimode state into constituent modes is to use a quantum pulse gate [1, 2, 11, 28]. These devices can be single-output [28] or multi-output [77], and in either case, they act similarly to homodyne detection in the sense that the shape of the pump pulse at the input determines which mode is selected for at the output. Quantum pulse gates separate a mode from the others while still retaining access to the unselected modes, as orthogonal modes are unaffected, which can be beneficial for cascaded processing. Once again, the pump pulse must be shaped, which determines the maximum bandwidth and resolution of the modes that can be selected for. While this is a mode-selective measurement and not a measurement of the modes, a quantum pulse gate has been used in conjunction with a closed-loop optimization method in order to determine the temporal mode shape of a photon [78].

Closed-loop iterative optimization has also been proposed for sorting multimode squeezed light into its most-squeezed supermodes based on self-configuring optics [38, 74]. An algorithmic approach to determining the temporal mode shape of non-Gaussian states has been implemented using continuous-wave dual-homodyne measurement [82].

In general, there is a plethora of options by which to measure multimode quantum light, each with its own benefits and downsides, which can be applied on different platforms. However, the entire bandwidths of ultrafast optical pulses are still much broader than the electronic photodetectors being used in these implementations. What is missing is a broadband measurement technique that can directly recover both the modal structure and quantum statistics of broadband multimode Gaussian states, without requiring knowledge of the mode basis or narrow-band electronic detection.

All-optical measurements

Because of the bandwidth limitations of electronic detection mentioned previously that limit the measurement of light to 100s of MHz, a few all-optical measurement schemes with a large bandwidth have been devised and implemented to circumvent this limitation. OPAs have been used for broadband phase-sensitive amplification in conjunction with photodetectors in squeezed state characterization [62, 80, 92] and non-Gaussian quantum state tomography [39]. They have also been used for all-optical feedforward without any photodetection systems in quantum operations such as controlling a squeezing gate [93] and implementing optical quantum teleportation [81]. These implementations not having a photodetector allows them to operate at rates limited by the bandwidths of the OPA and pulses, in this case reaching the milestone of 1 THz. These works show how lifting the limit on measurement rates allows for ultrafast quantum information processing, as inline measurements are a part of most quantum computational protocols, so speeding them up is of vital importance to reaching ultrafast operation and surpassing classical computational speeds, which take advantage of the GHz clock rates of classical computers [64]. Besides information processing, quantum communication is also currently being limited by electronic and electro-optic bandwidths [6, 10] and could also potentially benefit from an all-optical measurement approach.

Another benefit of using optical amplification rather than electronic amplification is that amplifying a quantum state optically brings it from the quantum to the classical domain, in which optical losses do not qualitatively change the state (i.e. losses introduce vacuum, which reduces or removes Wigner negativity and non-Gaussianity from quantum states).

Optical phase-sensitive amplification, such as that achieved using OPAs, imprints the quantum statistics of the state onto the amplified state, which allows state tomography to be performed even with significant optical losses between the OPA and photodetector [36, 62, 92]. Furthermore, amplifying the multimode squeezed state with a multimode OPA and characterizing the state using knowledge of the OPA's mode structure takes advantage of the broadband and high-gain amplification and multimode nature of the OPA [37]. As long as the loss between the state generated and the OPA is minimal, the state can be faithfully reconstructed. For all these reasons, we believe that OPAs have a strong position in the world of optical quantum computation, sensing, and communication and can enable ultrafast operations through their quantum-to-classical conversion and phase-sensitive amplification.

1.4 Dissertation overview

In this thesis, we discuss new avenues for ultrafast quantum measurements using ultra-broadband integrated nanophotonic OPAs on thin-film lithium niobate. We investigate three different measurement schemes that all rely on an OPA to amplify a quantum state to a macroscopic level rather than a photon-absorption or electronic spectral measurement. The large bandwidths of these OPAs, achieved through dispersion engineering, span many THz, which opens the door to ultrafast quantum optical information processing and communication. Two of these schemes are implemented experimentally, and the last is a forward-looking study on the possibilities in mode characterization enabled by this platform.

In Chapter 2, we briefly give an overview of the theory of continuous-variable quantum optics, second-order nonlinearities in quantum optics, multimode quantum optics, and quantum detector tomography. We begin with the notation of annihilation and quadrature operators and describe how quantum states act under the $\chi^{(2)}$ nonlinearity. We then introduce the concept of spectrotemporal modes and show how they relate to the annihilation operators in the time-bin and frequency-bin basis and how the principal mode basis can be obtained for a pulse-pumped broadband OPA. Finally, we describe how a quantum detection system can be characterized through quantum detector tomography.

In Chapter 3, we show how OPAs can be used as room-temperature ultrafast single-photon detectors. We experimentally demonstrate quantum detector tomography of an OPA detector (OPAD) consisting of an OPA and a photodetector. The performance extracted indicates a single-photon detection efficiency of 26.5% for a dark-count probability of 2.2%, which falls short of state-of-the-art photon detectors. The detector, however, was operated at 250 MHz, which is on the upper end of state-of-the-art detectors, with the potential for increasing the speed to 18 GHz when limited by the photodetector. This OPAD's performance is not sufficient to generate non-Gaussianity from a Gaussian state such as squeezed vacuum. Looking forward, we also present a path towards non-Gaussian operation by performing a quantum non-demolition measurement by post-selecting on a homodyne measurement of the pump at the output of the OPA. This system can be achieved with a higher nonlinearity-to-loss ratio (g/κ) of about two orders of magnitude greater than what our OPA exhibits and one order of magnitude greater than the current highest ratio achieved in lithium niobate [55].

In Chapter 4, we experimentally demonstrate multimode ultrafast squeezed vacuum measurements using an OPA. The squeezed vacuum is both generated and measured on the same chip using broadband OPAs, so both of these OPAs amplify light in multiple modes. In this chapter, we take into account this multimode nature of the light and extract the squeezing value both of a mode-averaged measurement based on the photon number distribution and of the principal squeezing mode, finding 2.41 dB of squeezing in the highest principal mode and 2 dB of squeezing for the mode-averaged measurement. The measurements were again taken using an 18 GHz photodetector that can distinguish between individual pulses, indicating the potential for ultrafast integrated quantum light processing, and we show how the speed can be improved even further by multiplexing photodetectors at the output of the chip. We also discuss the effects of pump depletion on the measured light and account for it in our analysis. While high squeezing can be measured without accounting for the multiple modes of broadband OPAs [62], we show here how accounting for this characteristic can improve the performance of the system.

In Chapter 5, we show how to further characterize multimode quantum light not only in its quadrature variances but also in its temporal mode shapes by adapting frequency-resolved optical gating (FROG) to quantum states and using a broadband OPA as the optical nonlinearity in the system. The OPA has the dual benefits of amplifying quantum light to a macroscopically detectable level and performing ultra-broadband phase-sensitive amplification that can amplify the whole spectrum of ultrafast quantum pulses. We numerically simulate the retrieval of mode shapes of four squeezed modes using an adapted iterative FROG algorithm and show that it functions even with a reduced signal-to-noise ratio (SNR), with mode shape fidelities of over 0.85 at 15 dB of SNR. Furthermore, we show that all second-order quadrature moments of a multimode state (i.e. the entire covariance matrix) can be characterized using this method. It is possible to completely characterize a zero-mean-field multimode Gaussian state with this method. This method works for non-Gaussian states as well, but does not provide the full information on the state. With this method, the complete information of a multimode Gaussian state can be obtained with a single measurement without pulse-shaping or closed loops, and the bandwidth is not limited by pulse-shaping techniques or electronic photodetector bandwidths, which is in stark contrast to current mode-shape measurements and selections.

Finally, in Chapter 6 we will discuss future directions that may become available to nonlinear quantum optics, and quantum optics in general. In the near term, performing operations on multimode ultrafast quantum optical states in the temporal mode basis offers a convenient way to generate large entangled states simply by changing the measurement basis, which opens the door to performing quantum optical information processing through measurement-based quantum computing, as has been done in time-multiplexed cluster states [4, 48]. The advances in fabrication technology on lithium niobate and other materials have already allowed the field to progress in terms of achievable operating regimes, and further such advances are likely to open up regimes such as deterministic non-Gaussianity [94, 95] or probabilistic large-scale quantum information processing [7, 59]. Furthermore, inhomogeneous material integration allows for combining multiple materials in order to take advantage most fully of the benefits of each material [98].

References

[1] Vahid Ansari, Benjamin Brecht, Jano Gil-Lopez, John M. Donohue, Jaroslav Řeháček, Zdeněk Hradil, Luis L. Sánchez-Soto, and Christine Silberhorn. "Achieving the Ultimate Quantum Timing Resolution". In: *PRX Quantum* 2.1 (Jan. 4, 2021), p. 010301. DOI: 10.1103/PRXQuantum.2.010301.

[2] Vahid Ansari, John M. Donohue, Benjamin Brecht, and Christine Silberhorn. "Tailoring nonlinear processes for quantum optics with pulsed temporal-mode encodings". In: *Optica* 5.5 (May 20, 2018), pp. 534–550. DOI: 10.1364/OPTICA.5.000534.

[3] Seiji Armstrong, Jean-François Morizur, Jiri Janousek, Boris Hage, Nicolas Treps, Ping Koy Lam, and Hans-A. Bachor. "Programmable multimode quantum networks". In: *Nature Communications* 3.1 (Aug. 28, 2012), p. 1026. DOI: 10.1038/ncomms2033.

[4] Warit Asavanant, Baramee Charoensombutamon, Shota Yokoyama, Takeru Ebihara, Tomohiro Nakamura, Rafael N. Alexander, Mamoru Endo, Jun-ichi Yoshikawa,

Nicolas C. Menicucci, Hidehiro Yonezawa, and Akira Furusawa. “Time-Domain-Multiplexed Measurement-Based Quantum Operations with 25-MHz Clock Frequency”. In: *Physical Review Applied* 16.3 (Sept. 2, 2021), p. 034005. DOI: 10.1103/PhysRevApplied.16.034005.

[5] Warit Asavanant, Yu Shiozawa, Shota Yokoyama, Baramee Charoensombutamon, Hiroki Emura, Rafael N. Alexander, Shuntaro Takeda, Jun-ichi Yoshikawa, Nicolas C. Menicucci, Hidehiro Yonezawa, and Akira Furusawa. “Generation of time-domain-multiplexed two-dimensional cluster state”. In: *Science* 366.6463 (Oct. 18, 2019), pp. 373–376. DOI: 10.1126/science.aay2645.

[6] Daniel Assumpcao, Dylan Renaud, Aida Baradari, Beibei Zeng, Chawina De-Eknamkul, C. J. Xin, Amirhassan Shams-Ansari, David Barton, Bartholomeus Machielse, and Marko Loncar. “A thin film lithium niobate near-infrared platform for multiplexing quantum nodes”. In: *Nature Communications* 15.1 (Dec. 2, 2024), p. 10459. DOI: 10.1038/s41467-024-54541-2.

[7] Ben Q. Baragiola, Giacomo Pantaleoni, Rafael N. Alexander, Angela Karanjai, and Nicolas C. Menicucci. “All-Gaussian Universality and Fault Tolerance with the Gottesman-Kitaev-Preskill Code”. In: *Physical Review Letters* 123.20 (Nov. 13, 2019), p. 200502. DOI: 10.1103/PhysRevLett.123.200502.

[8] Ismail Barakat, Mahmoud Kalash, Dennis Scharwald, Polina Sharapova, Norbert Lindlein, and Maria Chekhova. *Simultaneous measurement of multimode squeezing*. Feb. 24, 2024. arXiv: 2402.15786[quant-ph].

[9] Sara Bartolucci, Patrick Birchall, Hector Bombín, Hugo Cable, Chris Dawson, Mercedes Gimeno-Segovia, Eric Johnston, Konrad Kieling, Naomi Nickerson, Mihir Pant, Fernando Pastawski, Terry Rudolph, and Chris Sparrow. “Fusion-based quantum computation”. In: *Nature Communications* 14.1 (Feb. 17, 2023), p. 912. DOI: 10.1038/s41467-023-36493-1.

[10] Andrea Bernardi, Marco Clementi, Marcello Bacchi, Matías Rubén Bolaños, Sara Congia, Francesco Garrisi, Andrea Martellosio, Marco Passoni, Alexander Wrobel, Costantino Agnesi, Giuseppe Vallone, Paolo Villoresi, Federico Andrea Sabattoli, Matteo Galli, and Daniele Bajoni. *Gigahertz-rate thin-film lithium niobate receiver for time-bin quantum communication*. Apr. 17, 2026. DOI: 10.48550/arXiv.2604.16695. arXiv: 2604.16695[quant-ph].

[11] Abhinandan Bhattacharjee, Patrick Folge, Laura Serino, Jaroslav Řeháček, Zdeněk Hradil, Christine Silberhorn, and Benjamin Brecht. “Pulse characterization at the single-photon level through chronocyclic Q-function measurements”. In: *Optics Express* 33.3 (Feb. 10, 2025), pp. 5551–5561. DOI: 10.1364/OE.540125.

[12] Andreas Boes, Lin Chang, Carsten Langrock, Mengjie Yu, Mian Zhang, Qiang Lin, Marko Lončar, Martin Fejer, John Bowers, and Arnan Mitchell. “Lithium niobate photonics: Unlocking the electromagnetic spectrum”. In: *Science* 379.6627 (Jan. 6, 2023), eabj4396. DOI: 10.1126/science.abj4396.

[13] B. Brecht, Dileep V. Reddy, C. Silberhorn, and M. G. Raymer. “Photon Temporal Modes: A Complete Framework for Quantum Information Science”. In: *Physical Review X* 5.4 (Oct. 30, 2015), p. 041017. DOI: 10.1103/PhysRevX.5.041017.

[14] A. V. Burlakov, M. V. Chekhova, O. A. Karabutova, and S. P. Kulik. “Collinear two-photon state with spectral properties of type-I and polarization properties of type-II spontaneous parametric down-conversion: Preparation and testing”. In: *Physical Review A* 64.4 (Sept. 17, 2001), p. 041803. DOI: 10.1103/PhysRevA.64.041803.

[15] Y. Cai, J. Roslund, G. Ferrini, F. Arzani, X. Xu, C. Fabre, and N. Treps. “Multimode entanglement in reconfigurable graph states using optical frequency combs”. In: *Nature Communications* 8.1 (June 6, 2017), p. 15645. DOI: 10.1038/ncomms15645.

[16] Catxere A. Casacio, Lars S. Madsen, Alex Terrasson, Muhammad Waleed, Kai Barnscheidt, Boris Hage, Michael A. Taylor, and Warwick P. Bowen. “Quantum-enhanced nonlinear microscopy”. In: *Nature* 594.7862 (June 2021), pp. 201–206. DOI: 10.1038/s41586-021-03528-w.

[17] Carlton M. Caves. “Quantum-mechanical noise in an interferometer”. In: *Physical Review D* 23.8 (Apr. 15, 1981), pp. 1693–1708. DOI: 10.1103/PhysRevD.23.1693.

[18] Francesco Ceccarelli, Giulia Acconcia, Angelo Gulinatti, Massimo Ghioni, Ivan Rech, and Roberto Osellame. “Recent Advances and Future Perspectives of Single-Photon Avalanche Diodes for Quantum Photonics Applications”. In: *Advanced Quantum Technologies* 4.2 (2021). _eprint: https://onlinelibrary.wiley.com/doi/pdf/10.1002/qute.20 p. 2000102. DOI: 10.1002/qute.202000102.

[19] J. Chang, J. W. N. Los, J. O. Tenorio-Pearl, N. Noordzij, R. Gourgues, A. Guardiani, J. R. Zichi, S. F. Pereira, H. P. Urbach, V. Zwiller, S. N. Dorenbos, and I. Esmaeil Zadeh. “Detecting telecom single photons with 99.52.07+0.5% system detection efficiency and high time resolution”. In: *APL Photonics* 6.3 (Mar. 30, 2021), p. 036114. DOI: 10.1063/5.0039772.

[20] Jia-Mou Chen, Chia-Yu Hsu, Wei-Kai Huang, Shih-Si Hsiao, Fu-Chen Huang, Yi-Hsin Chen, Chih-Sung Chuu, Ying-Cheng Chen, Yong-Fan Chen, and Ite A. Yu. “Room-temperature biphoton source with a spectral brightness near the ultimate limit”. In: *Physical Review Research* 4.2 (May 18, 2022), p. 023132. DOI: 10.1103/PhysRevResearch.4.023132.

[21] Jeff Chiles, Ilya Charaev, Robert Lasenby, Masha Baryakhtar, Junwu Huang, Alexana Roshko, George Burton, Marco Colangelo, Ken Van Tilburg, Asimina Arvanitaki, Sae Woo Nam, and Karl K. Berggren. “New Constraints on Dark Photon Dark Matter with Superconducting Nanowire Detectors in an Optical Haloscope”. In: *Physical Review Letters* 128.23 (June 10, 2022), p. 231802. DOI: 10.1103/PhysRevLett.128.231802.

[22] Rachel N. Clark, Bethany Puzio, Oliver M. Green, Siva T. Pradyumna, Oliver Trojak, Alberto Politi, and Jonathan C. F. Matthews. “Integrated photonics for continuous-variable quantum optics”. In: *Nature Photonics* (Apr. 27, 2026), pp. 1–15. DOI: 10.1038/s41566-026-01864-9.

[23] Lidice Cruz-Rodriguez, Diptesh Dey, Antonia Freibert, and Philipp Stammer. “Quantum phenomena in attosecond science”. In: *Nature Reviews Physics* 6.11 (Nov. 2024), pp. 691–704. DOI: 10.1038/s42254-024-00769-2.

[24] J. Demsar. “Non-equilibrium Phenomena in Superconductors Probed by Femtosecond Time-Domain Spectroscopy”. In: *Journal of Low Temperature Physics* 201.5 (Dec. 1, 2020), pp. 676–709. DOI: 10.1007/s10909-020-02461-y.

[25] Boris Desiatov and Marko Lončar. “Silicon photodetector for integrated lithium niobate photonics”. In: *Applied Physics Letters* 115.12 (Sept. 20, 2019), p. 121108. DOI: 10.1063/1.5118901.

[26] Pierre Didier, Prakhar Jain, Mathieu Bertrand, Jost Kellner, Oliver Pitz, Zhecheng Dai, Tristan Kuttner, Mattias Beck, Baile Chen, Jérôme Faist, and Rachel Grange. “Thin film lithium niobate on sapphire for integrated mid-infrared modulator”. en. In: *Nature Communications* 17.1 (Feb. 2026), p. 3050. DOI: 10.1038/s41467-026-69880-5.

[27] Miller Eaton, Amr Hossameldin, Richard J. Birrittella, Paul M. Alsing, Christopher C. Gerry, Hai Dong, Chris Cuevas, and Olivier Pfister. “Resolution of 100 photons and quantum generation of unbiased random numbers”. In: *Nature Photonics* 17.1 (Jan. 2023), pp. 106–111. DOI: 10.1038/s41566-022-01105-9.

[28] Andreas Eckstein, Benjamin Brecht, and Christine Silberhorn. “A quantum pulse gate based on spectrally engineered sum frequency generation”. In: *Optics Express* 19.15 (July 18, 2011), pp. 13770–13778. DOI: 10.1364/OE.19.013770.

[29] Iman Esmaeil Zadeh, J. Chang, Johannes W. N. Los, Samuel Gyger, Ali W. Elshaari, Stephan Steinhauer, Sander N. Dorenbos, and Val Zwiller. “Superconducting nanowire single-photon detectors: A perspective on evolution, state-of-the-art, future developments, and applications”. In: *Applied Physics Letters* 118.19 (May 10, 2021), p. 190502. DOI: 10.1063/5.0045990.

[30] C. Fabre and N. Treps. “Modes and states in quantum optics”. In: *Reviews of Modern Physics* 92.3 (Sept. 10, 2020), p. 035005. DOI: 10.1103/RevModPhys.92.035005.

[31] Warren Grice and Ian A. Walmsley. “Homodyne detection in a photon counting application”. In: *Journal of Modern Optics* 43.4 (Apr. 1, 1996), pp. 795–805. DOI: 10.1080/09500349608232783.

[32] De-Yong He, Shuang Wang, Jia-Lin Chen, Wei Chen, Zhen-Qiang Yin, Guan-Jie Fan-Yuan, Zheng Zhou, Guang-Can Guo, and Zheng-Fu Han. "2.5 GHz Gated InGaAs/InP Single-Photon Avalanche Diode with 44 ps Time Jitter". In: *Advanced Devices & Instrumentation* 4 (Sept. 13, 2023), p. 0020. DOI: `10.34133/adi.0020`.

[33] D. Istrati, Y. Pilnyak, J. C. Loredo, C. Antón, N. Somaschi, P. Hilaire, H. Ollivier, M. Esmann, L. Cohen, L. Vidro, C. Millet, A. Lemaître, I. Sagnes, A. Harouri, L. Lanco, P. Senellart, and H. S. Eisenberg. "Sequential generation of linear cluster states from a single photon emitter". In: *Nature Communications* 11.1 (Oct. 30, 2020). Number: 1, p. 5501. DOI: `10.1038/s41467-020-19341-4`.

[34] Usman A. Javid, Raymond Lopez-Rios, Jingwei Ling, Austin Graf, Jeremy Staffa, and Qiang Lin. "Chip-scale simulations in a quantum-correlated synthetic space". In: *Nature Photonics* 17.10 (Oct. 2023), pp. 883–890. DOI: `10.1038/s41566-023-01236-7`.

[35] Wenhe Jia, Grégoire Saerens, Ülle-Linda Talts, Helena Weigand, Robert J. Chapman, Liu Li, Rachel Grange, and Yuanmu Yang. *Polarization-entangled photon pair generation from an epsilon-near-zero metasurface*. June 13, 2024. DOI: `10.48550/arXiv.2405.03493`. arXiv: `2405.03493[physics]`.

[36] Mahmoud Kalash and Maria V. Chekhova. "Wigner function tomography via optical parametric amplification". In: *Optica* 10.9 (Sept. 20, 2023), p. 1142. DOI: `10.1364/OPTICA.488697`.

[37] Mahmoud Kalash, Ui-Nyung Han, Young-Sik Ra, and Maria V. Chekhova. *Efficient detection of spectrally multimode squeezed light through optical parametric amplification*. Aug. 6, 2025. DOI: `10.48550/arXiv.2508.04502`. arXiv: `2508.04502[quant-ph]`.

[38] Aviv Karnieli, Paul-Alexis Mor, Charles Roques-Carmes, Eran Lustig, Jamison Sloan, Jelena Vučković, David A. B. Miller, and Shanhui Fan. *Variational processing of multimode squeezed light*. Sept. 20, 2025. DOI: `10.48550/arXiv.2509.16753`. arXiv: `2509.16753[quant-ph]`.

[39] Akito Kawasaki, Ryuhoh Ide, Hector Brunel, Takumi Suzuki, Rajveer Nehra, Katsuki Nakashima, Takahiro Kashiwazaki, Asuka Inoue, Takeshi Umeki, Fumihiro China, Masahiro Yabuno, Shigehito Miki, Hirotaka Terai, Taichi Yamashima, Atsushi Sakaguchi, Kan Takase, Mamoru Endo, Warit Asavanant, and Akira Furusawa. "Broadband generation and tomography of non-Gaussian states for ultrafast optical quantum processors". In: *Nature Communications* 15.1 (Nov. 1, 2024), p. 9075. DOI: `10.1038/s41467-024-53408-w`.

[40] H. J. Kimble. "The quantum internet". In: *Nature* 453.7198 (June 2008), pp. 1023–1030. DOI: `10.1038/nature07127`.

[41] Matthias Kizmann, Thiago Lucena De M. Guedes, Denis V. Seletskiy, Andrey S. Moskalenko, Alfred Leitenstorfer, and Guido Burkard. "Subcycle squeezing of light from a time flow perspective - Supp". In: *Nature Physics* 15.9 (Sept. 2019), pp. 960–966. DOI: 10.1038/s41567-019-0560-2.

[42] Matthias Kizmann, Thiago Lucena de M. Guedes, Denis V. Seletskiy, Andrey S. Moskalenko, Alfred Leitenstorfer, and Guido Burkard. "Subcycle squeezing of light from a time flow perspective". In: *Nature Physics* 15.9 (Sept. 2019), pp. 960–966. DOI: 10.1038/s41567-019-0560-2.

[43] Emanuel Knill, Raymond Laflamme, and Gerard Milburn. "A scheme for efficient quantum computation with linear optics". In: 409 (2001).

[44] Shunya Konno, Warit Asavanant, Fumiya Hanamura, Hironari Nagayoshi, Kosuke Fukui, Atsushi Sakaguchi, Ryuhoh Ide, Fumihiro China, Masahiro Yabuno, Shigehito Miki, Hirotaka Terai, Kan Takase, Mamoru Endo, Petr Marek, Radim Filip, Peter van Loock, and Akira Furusawa. "Logical states for fault-tolerant quantum computation with propagating light". In: *Science* 383.6680 (Jan. 19, 2024), pp. 289–293. DOI: 10.1126/science.adk7560.

[45] Paul G. Kwiat, Edo Waks, Andrew G. White, Ian Appelbaum, and Philippe H. Eberhard. "Ultrabright source of polarization-entangled photons". In: *Physical Review A* 60.2 (Aug. 1, 1999), R773–R776. DOI: 10.1103/PhysRevA.60.R773.

[46] M. V. Larsen, J. E. Bourassa, S. Kocsis, J. F. Tasker, R. S. Chadwick, C. González-Arciniegas, J. Hastrup, C. E. Lopetegui-González, F. M. Miatto, A. Motamedi, R. Noro, G. Roeland, R. Baby, H. Chen, P. Contu, I. Di Luch, C. Drago, M. Giesbrecht, T. Grainge, I. Krasnokutska, M. Menotti, B. Morrison, C. Puviraj, K. Rezaei Shad, B. Hussain, J. McMahon, J. E. Ortmann, M. J. Collins, C. Ma, D. S. Phillips, M. Seymour, Q. Y. Tang, B. Yang, Z. Vernon, R. N. Alexander, and D. H. Mahler. "Integrated photonic source of Gottesman–Kitaev–Preskill qubits". In: *Nature* 642.8068 (June 2025), pp. 587–591. DOI: 10.1038/s41586-025-09044-5.

[47] Mikkel V. Larsen, Xueshi Guo, Casper R. Breum, Jonas S. Neergaard-Nielsen, and Ulrik L. Andersen. "Deterministic generation of a two-dimensional cluster state". In: *Science* 366.6463 (Oct. 18, 2019), pp. 369–372. DOI: 10.1126/science.aay4354.

[48] Mikkel V. Larsen, Xueshi Guo, Casper R. Breum, Jonas S. Neergaard-Nielsen, and Ulrik L. Andersen. "Deterministic multi-mode gates on a scalable photonic quantum computing platform". In: *Nature Physics* 17.9 (Sept. 2021), pp. 1018–1023. DOI: 10.1038/s41567-021-01296-y.

[49] B. J. Lawrie, P. D. Lett, A. M. Marino, and R. C. Pooser. "Quantum Sensing with Squeezed Light". In: *ACS Photonics* 6.6 (June 19, 2019), pp. 1307–1318. DOI: 10.1021/acsphotonics.9b00250.

[50] Luis Ledezma, Ryoto Sekine, Qiushi Guo, Rajveer Nehra, Saman Jahani, and Alireza Marandi. “Intense optical parametric amplification in dispersion-engineered nanophotonic lithium niobate waveguides”. In: *Optica* 9.3 (Mar. 20, 2022), p. 303. DOI: 10.1364/OPTICA.442332.

[51] Gordon H.Y. Li, Ryoto Sekine, Rajveer Nehra, Robert M. Gray, Luis Ledezma, Qiushi Guo, and Alireza Marandi. “All-optical ultrafast ReLU function for energy-efficient nanophotonic deep learning”. In: *Nanophotonics* 12.5 (Mar. 10, 2023), pp. 847–855. DOI: 10.1515/nanoph-2022-0137.

[52] S. Lischke, A. Peczek, J. S. Morgan, K. Sun, D. Steckler, Y. Yamamoto, F. Korndörfer, C. Mai, S. Marschmeyer, M. Fraschke, A. Krüger, A. Beling, and L. Zimmermann. “Ultra-fast germanium photodiode with 3-dB bandwidth of 265 GHz”. In: *Nature Photonics* 15.12 (Dec. 2021), pp. 925–931. DOI: 10.1038/s41566-021-00893-w.

[53] Adriana E Lita, Aaron J Miller, and Sae Woo Nam. “Counting near-infrared single-photons with 95% efficiency”. In: *Optics express* 16.5 (2008), pp. 3032–3040.

[54] Zheng-Hao Liu, Romain Brunel, Emil E. B. Østergaard, Oscar Cordero, Senrui Chen, Yat Wong, Jens A. H. Nielsen, Axel B. Bregnsbo, Sisi Zhou, Hsin-Yuan Huang, Changhun Oh, Liang Jiang, John Preskill, Jonas S. Neergaard-Nielsen, and Ulrik L. Andersen. “Quantum learning advantage on a scalable photonic platform”. In: *Science* 389.6767 (Sept. 25, 2025), pp. 1332–1335. DOI: 10.1126/science.adv2560.

[55] Juanjuan Lu, Ming Li, Chang-Ling Zou, Ayed Al Sayem, and Hong X. Tang. “Toward 1% single-photon anharmonicity with periodically poled lithium niobate microring resonators”. In: *Optica* 7.12 (Dec. 20, 2020), p. 1654. DOI: 10.1364/OPTICA.403931.

[56] Jinyong Ma, Tongmiao Fan, Tuomas Haggren, Laura Valencia Molina, Matthew Parry, Saniya Shinde, Jihua Zhang, Rocio Camacho Morales, Frank Setzpfandt, Hark Hoe Tan, Chennupati Jagadish, Dragomir N. Neshev, and Andrey A. Sukhorukov. “Generation of tunable quantum entanglement via nonlinearity symmetry breaking in semiconductor metasurfaces”. In: *Science Advances* 11.28 (July 11, 2025), eadu4133. DOI: 10.1126/sciadv.adu4133. arXiv: 2409.10845[physics].

[57] Andreas Maeder, Robert J. Chapman, Alessandra Sabatti, Giovanni Finco, Jost Kellner, and Rachel Grange. *Programmable Bell State Generation in an Integrated Thin Film Lithium Niobate Circuit*. June 22, 2025. DOI: 10.48550/arXiv.2506.18079. arXiv: 2506.18079[quant-ph].

[58] A. Mari and J. Eisert. “Positive Wigner Functions Render Classical Simulation of Quantum Computation Efficient”. In: *Physical Review Letters* 109.23 (Dec. 4, 2012), p. 230503. DOI: 10.1103/PhysRevLett.109.230503.

[59] Nicolas C. Menicucci. "Fault-Tolerant Measurement-Based Quantum Computing with Continuous-Variable Cluster States". In: *Physical Review Letters* 112.12 (Mar. 26, 2014), p. 120504. DOI: 10.1103/PhysRevLett.112.120504.

[60] Nicolas C. Menicucci, Peter Van Loock, Mile Gu, Christian Weedbrook, Timothy C. Ralph, and Michael A. Nielsen. "Universal Quantum Computation with Continuous-Variable Cluster States". In: *Physical Review Letters* 97.11 (Sept. 13, 2006), p. 110501. DOI: 10.1103/PhysRevLett.97.110501.

[61] M. Müller, S. Bounouar, K. D. Jöns, M. Glässl, and P. Michler. "On-demand generation of indistinguishable polarization-entangled photon pairs". In: *Nature Photonics* 8.3 (Mar. 2014). Number: 3, pp. 224–228. DOI: 10.1038/nphoton.2013.377.

[62] Rajveer Nehra, Ryoto Sekine, Luis Ledezma, Qiushi Guo, Robert M. Gray, Arkadev Roy, and Alireza Marandi. "Few-cycle vacuum squeezing in nanophotonics". In: *Science* 377.6612 (Sept. 16, 2022), pp. 1333–1337. DOI: 10.1126/science.abo6213.

[63] Edwin Ng, Ryotatsu Yanagimoto, Marc Jankowski, M. M. Fejer, and Hideo Mabuchi. *Quantum noise dynamics in nonlinear pulse propagation*. July 11, 2023. arXiv: 2307.05464[physics,physics:quant-ph].

[64] Changhun Oh, Minzhao Liu, Yuri Alexeev, Bill Fefferman, and Liang Jiang. "Classical algorithm for simulating experimental Gaussian boson sampling". In: *Nature Physics* 20.9 (Sept. 2024), pp. 1461–1468. DOI: 10.1038/s41567-024-02535-8.

[65] Alexei Ourjoumtsev, Rosa Tualle-Brouri, Julien Laurat, and Philippe Grangier. "Generating Optical Schrödinger Kittens for Quantum Information Processing". In: *Science* 312.5770 (Apr. 7, 2006), pp. 83–86. DOI: 10.1126/science.1122858.

[66] Federico Pegoraro, Philip Held, Jonas Lammers, Benjamin Brecht, and Christine Silberhorn. *Demonstration of a Photonic Time-Multiplexed C-NOT Gate*. Dec. 3, 2024. DOI: 10.48550/arXiv.2412.02478. arXiv: 2412.02478[quant-ph].

[67] S. Pirandola, U. L. Andersen, L. Banchi, M. Berta, D. Bunandar, R. Colbeck, D. Englund, T. Gehring, C. Lupo, C. Ottaviani, J. L. Pereira, M. Razavi, J. Shamsul Shaari, M. Tomamichel, V. C. Usenko, G. Vallone, P. Villoresi, and P. Wallden. "Advances in quantum cryptography". In: *Advances in Optics and Photonics* 12.4 (Dec. 31, 2020), pp. 1012–1236. DOI: 10.1364/AOP.361502.

[68] Young-Sik Ra, Adrien Dufour, Mattia Walschaers, Clément Jacquard, Thibault Michel, Claude Fabre, and Nicolas Treps. "Non-Gaussian quantum states of a multimode light field". In: *Nature Physics* 16.2 (Feb. 2020), pp. 144–147. DOI: 10.1038/s41567-019-0726-y.

[69] Robert Raussendorf and Hans J. Briegel. "A One-Way Quantum Computer". In: *Physical Review Letters* 86.22 (May 28, 2001), pp. 5188–5191. DOI: 10.1103/PhysRevLett.86.5188.

[70] Dileep V. Reddy, Robert R. Nerem, Sae Woo Nam, Richard P. Mirin, and Varun B. Verma. "Superconducting nanowire single-photon detectors with 98% system detection efficiency at 1550 nm". In: *Optica* 7.12 (Dec. 20, 2020), p. 1649. DOI: 10.1364/OPTICA.400751.

[71] Giovanni V. Resta, Lorenzo Stasi, Matthieu Perrenoud, Sylvain El-Khoury, Tiff Brydges, Rob Thew, Hugo Zbinden, and Félix Bussières. "GHz detection rates and dynamic photon-number resolution with superconducting nanowire arrays". In: *Nano Letters* 23.13 (July 12, 2023), pp. 6018–6026. DOI: 10.1021/acs.nanolett.3c01228. arXiv: 2303.17401[physics,physics:quant-ph].

[72] C. Riek, P. Sulzer, M. Seeger, A. S. Moskalenko, G. Burkard, D. V. Seletskiy, and A. Leitenstorfer. "Subcycle quantum electrodynamics". In: *Nature* 541.7637 (Jan. 2017), pp. 376–379. DOI: 10.1038/nature21024.

[73] Chan Roh, Geunhee Gwak, Young-Do Yoon, and Young-Sik Ra. "Generation of three-dimensional cluster entangled state". In: *Nature Photonics* 19.5 (May 2025), pp. 526–532. DOI: 10.1038/s41566-025-01631-2.

[74] Charles Roques-Carmes, Shanhui Fan, and David A. B. Miller. "Measuring, processing, and generating partially coherent light with self-configuring optics". In: *Light: Science & Applications* 13.1 (Sept. 20, 2024), p. 260. DOI: 10.1038/s41377-024-01622-y.

[75] Jonathan Roslund, Renné Medeiros de Araújo, Shifeng Jiang, Claude Fabre, and Nicolas Treps. "Wavelength-multiplexed quantum networks with ultrafast frequency combs". In: *Nature Photonics* 8.2 (Feb. 2014), pp. 109–112. DOI: 10.1038/nphoton.2013.340.

[76] Pascale Senellart, Glenn Solomon, and Andrew White. "High-performance semiconductor quantum-dot single-photon sources". In: *Nature Nanotechnology* 12.11 (Nov. 2017), pp. 1026–1039. DOI: 10.1038/nnano.2017.218.

[77] Laura Serino, Jano Gil-Lopez, Michael Stefszky, Raimund Ricken, Christof Eigner, Benjamin Brecht, and Christine Silberhorn. "Realization of a Multi-Output Quantum Pulse Gate for Decoding High-Dimensional Temporal Modes of Single-Photon States". In: *PRX Quantum* 4.2 (Apr. 12, 2023), p. 020306. DOI: 10.1103/PRXQuantum.4.020306.

[78] Laura Serino, Markus Rambach, Benjamin Brecht, Jacquiline Romero, and Christine Silberhorn. "Self-guided tomography of time-frequency qudits". In: *Quantum Science and Technology* 10.2 (Apr. 1, 2025), p. 025024. DOI: 10.1088/2058-9565/adb0ea.

[79] Laura Serino, Werner Ridder, Abhinandan Bhattacharjee, Jano Gil-Lopez, Benjamin Brecht, and Christine Silberhorn. "Orchestrating time and color: a programmable source of high-dimensional entanglement". In: *Optica Quantum* 2.5 (Oct. 25, 2024), pp. 339–345. DOI: 10.1364/OPTICAQ.532334.

[80] Yaakov Shaked, Yoad Michael, Rafi Z. Vered, Leon Bello, Michael Rosenbluh, and Avi Pe'er. "Lifting the bandwidth limit of optical homodyne measurement with broadband parametric amplification". In: *Nature Communications* 9.1 (Feb. 9, 2018), p. 609. DOI: `10.1038/s41467-018-03083-5`.

[81] Takumi Suzuki, Takaya Hoshi, Akito Kawasaki, Shotaro Oki, Konhi Ichii, Hironari Nagayoshi, Kazuma Takahashi, Takahiro Kashiwazaki, Taichi Yamashima, Asuka Inoue, Takeshi Umeki, Tatsuki Sonoyama, Kan Takase, Warit Asavanant, Mamoru Endo, and Akira Furusawa. *Ultrafast all-optical quantum teleportation*. Apr. 16, 2026. DOI: `10.48550/arXiv.2604.14959`. arXiv: `2604.14959[quant-ph]`.

[82] Kan Takase, Masanori Okada, Takahiro Serikawa, Shuntaro Takeda, Jun-ichi Yoshikawa, and Akira Furusawa. "Complete temporal mode characterization of non-Gaussian states by a dual homodyne measurement". In: *Physical Review A* 99.3 (Mar. 18, 2019), p. 033832. DOI: `10.1103/PhysRevA.99.033832`.

[83] Sjoerd Telkamp, Odiel Hooybergs, Myriam Rihani, Giovanni Finco, Tummas Napoleon Arge, Robin N. Dür, Victor Mougel, Daniel Scheffler, Filip Krizek, Rachel Grange, Robert J. Chapman, and Werner Wegscheider. *High-temperature growth of ultra thin NbTiN films on lithium niobate for integrated single photon detection*. Version Number: 1. 2025. DOI: `10.48550/ARXIV.2509.07870`.

[84] M. Tse, Haocun Yu, N. Kijbunchoo, A. Fernandez-Galiana, P. Dupej, L. Barsotti, C. D. Blair, D. D. Brown, S. E. Dwyer, A. Effler, M. Evans, P. Fritschel, V. V. Frolov, A. C. Green, G. L. Mansell, F. Matichard, N. Mavalvala, D. E. McClelland, L. McCuller, T. McRae, J. Miller, A. Mullavey, E. Oelker, I. Y. Phinney, D. Sigg, B. J. J. Slagmolen, T. Vo, R. L. Ward, C. Whittle, R. Abbott, C. Adams, R. X. Adhikari, A. Ananyeva, S. Appert, K. Arai, J. S. Areeda, Y. Asali, S. M. Aston, C. Austin, A. M. Baer, M. Ball, S. W. Ballmer, S. Banagiri, D. Barker, J. Bartlett, B. K. Berger, J. Betzwieser, D. Bhattacharjee, G. Billingsley, S. Biscans, R. M. Blair, N. Bode, P. Booker, R. Bork, A. Bramley, A. F. Brooks, A. Buikema, C. Cahillane, K. C. Cannon, X. Chen, A. A. Ciobanu, F. Clara, S. J. Cooper, K. R. Corley, S. T. Countryman, P. B. Covas, D. C. Coyne, L. E. H. Datrier, D. Davis, C. Di Fronzo, J. C. Driggers, T. Etzel, T. M. Evans, J. Feicht, P. Fulda, M. Fyffe, J. A. Giaime, K. D. Giardina, P. Godwin, E. Goetz, S. Gras, C. Gray, R. Gray, Anchal Gupta, E. K. Gustafson, R. Gustafson, J. Hanks, J. Hanson, T. Hardwick, R. K. Hasskew, M. C. Heintze, A. F. Helmling-Cornell, N. A. Holland, J. D. Jones, S. Kandhasamy, S. Karki, M. Kasprzack, K. Kawabe, P. J. King, et al. "Quantum-Enhanced Advanced LIGO Detectors in the Era of Gravitational-Wave Astronomy". In: *Physical Review Letters* 123.23 (Dec. 5, 2019), p. 231107. DOI: `10.1103/PhysRevLett.123.231107`.

[85] Matan Even Tzur, Chen Mor, Noa Yaffe, Michael Birk, Andrei Rasputnyi, Omer Kneller, Ido Nisim, Ido Kaminer, Maria Chekhova, Michael Krueger, Misha Ivanov, Nirit Dudovich, and Oren Cohen. *Attosecond-resolved quantum fluctuations of light*

and matter. Nov. 23, 2025. DOI: 10.48550/arXiv.2511.18362. arXiv: 2511.18362[physics].

[86] Matan Even Tzur, Chen Mor, Noa Yaffe, Michael Birk, Andrei Rasputnyi, Omer Kneller, Ido Nisim, Ido Kaminer, Michael Krüger, Nirit Dudovich, and Oren Cohen. *Measuring and controlling the birth of quantum attosecond pulses*. Feb. 13, 2025. DOI: 10.48550/arXiv.2502.09427. arXiv: 2502.09427[physics].

[87] Ravitej Uppu, Freja T. Pedersen, Ying Wang, Cecilie T. Olesen, Camille Papon, Xiaoyan Zhou, Leonardo Midolo, Sven Scholz, Andreas D. Wieck, Arne Ludwig, and Peter Lodahl. "Scalable integrated single-photon source". In: *Science Advances* 6.50 (Dec. 9, 2020), eabc8268. DOI: 10.1126/sciadv.abc8268.

[88] Henning Vahlbruch, Moritz Mehmet, Karsten Danzmann, and Roman Schnabel. "Detection of 15 dB Squeezed States of Light and their Application for the Absolute Calibration of Photoelectric Quantum Efficiency". In: *Physical Review Letters* 117.11 (Sept. 6, 2016), p. 110801. DOI: 10.1103/PhysRevLett.117.110801.

[89] Ze Wang, Kangkang Li, Yue Wang, Xin Zhou, Yinke Cheng, Boxuan Jing, Fengxiao Sun, Jincheng Li, Zhilin Li, Qihuang Gong, Qiongyi He, Bei-Bei Li, and Qi-Fan Yang. *Chip-scale generation of 60-mode continuous-variable cluster states*. June 15, 2024. DOI: 10.48550/arXiv.2406.10715. arXiv: 2406.10715.

[90] James Williams, Rajveer Nehra, Elina Sendonaris, Luis Ledezma, Robert M. Gray, Ryoto Sekine, and Alireza Marandi. "High Brightness Broadband Photon-Pairs at 2 m in Lithium Niobate Nanophotonics". In: *CLEO 2023 (2023), paper FF2L.2*. CLEO: Fundamental Science. Optica Publishing Group, May 7, 2023, FF2L.2. DOI: 10.1364/CLEO_FS.2023.FF2L.2.

[91] James Williams, Rajveer Nehra, **Sendonaris, Elina**, Luis Ledezma, Robert M. Gray, Ryoto Sekine, and Alireza Marandi. "Ultrashort pulse biphoton source in lithium niobate nanophotonics at 2 μm". In: *Nanophotonics* 13.18 (Aug. 1, 2024), pp. 3535–3544. DOI: 10.1515/nanoph-2024-0054.

[92] James Williams*, Elina Sendonaris*, Rajveer Nehra, Robert M. Gray, Ryoto Sekine, Luis Ledezma, and Alireza Marandi. "Ultrafast all-optical measurement of squeezed vacuum in a lithium niobate nanophotonic circuit". In: *Physical Review Research* 7.4 (Oct. 1, 2025), p. 043006. DOI: 10.1103/rvmb-ljd3.

[93] Taichi Yamashima, Takahiro Kashiwazaki, Takumi Suzuki, Rajveer Nehra, Tomohiro Nakamura, Asuka Inoue, Takeshi Umeki, Kan Takase, Warit Asavanant, Mamoru Endo, and Akira Furusawa. "All-optical measurement-device-free feedforward enabling ultra-fast quantum information processing". In: *Optics Express* 33.3 (Feb. 10, 2025), pp. 5769–5780. DOI: 10.1364/OE.550832.

[94] Ryotatsu Yanagimoto, Rajveer Nehra, Ryan Hamerly, Edwin Ng, Alireza Marandi, and Hideo Mabuchi. "Quantum Nondemolition Measurements with Optical Parametric Amplifiers for Ultrafast Universal Quantum Information Processing". In:

PRX Quantum 4.1 (Mar. 29, 2023), p. 010333. DOI: 10.1103/PRXQuantum.4.010333.

[95] Ryotatsu Yanagimoto, Edwin Ng, Marc Jankowski, Hideo Mabuchi, and Ryan Hamerly. "Temporal trapping: a route to strong coupling and deterministic optical quantum computation". In: *Optica* 9.11 (Nov. 20, 2022), pp. 1289–1296. DOI: 10.1364/OPTICA.473276.

[96] Ryotatsu Yanagimoto, Edwin Ng, Marc Jankowski, Rajveer Nehra, Timothy P. McKenna, Tatsuhiro Onodera, Logan G. Wright, Ryan Hamerly, Alireza Marandi, M. M. Fejer, and Hideo Mabuchi. "Mesoscopic ultrafast nonlinear optics—the emergence of multimode quantum non-Gaussian physics". In: *Optica* 11.7 (July 20, 2024), pp. 896–918. DOI: 10.1364/OPTICA.514075.

[97] Geehyun Yang, Matthias Kizmann, Alfred Leitenstorfer, and Andrey S. Moskalenko. "Subcycle tomography of quantum light". In: *Physical Review A* 113.4 (Apr. 1, 2026), p. 043703. DOI: 10.1103/m5ln-m31l.

[98] Can Yu, Meng Zhang, Lei Liang, Li Qin, Yongyi Chen, Yuxin Lei, Yubing Wang, Yue Song, Cheng Qiu, Peng Jia, Dabing Li, and Lijun Wang. "Advancements in transfer printing techniques and their applications in photonic integrated circuits". In: *Light: Science & Applications* 14.1 (Dec. 5, 2025), p. 396. DOI: 10.1038/s41377-025-02064-w.

[99] Weijun Zhang, Jia Huang, Chengjun Zhang, Lixing You, Chaolin Lv, Lu Zhang, Hao Li, Zhen Wang, and Xiaoming Xie. "A 16-Pixel Interleaved Superconducting Nanowire Single-Photon Detector Array With A Maximum Count Rate Exceeding 1.5 GHz". In: *IEEE Transactions on Applied Superconductivity* 29.5 (Aug. 2019). Conference Name: IEEE Transactions on Applied Superconductivity, pp. 1–4. DOI: 10.1109/TASC.2019.2895621.

[100] Yichen Zhang, Yiming Bian, Zhengyu Li, Song Yu, and Hong Guo. "Continuous-variable quantum key distribution system: Past, present, and future". In: *Applied Physics Reviews* 11.1 (Mar. 1, 2024), p. 011318. DOI: 10.1063/5.0179566.

[101] Han-Sen Zhong, Hui Wang, Yu-Hao Deng, Ming-Cheng Chen, Li-Chao Peng, Yi-Han Luo, Jian Qin, Dian Wu, Xing Ding, Yi Hu, Peng Hu, Xiao-Yan Yang, Wei-Jun Zhang, Hao Li, Yuxuan Li, Xiao Jiang, Lin Gan, Guangwen Yang, Lixing You, Zhen Wang, Li Li, Nai-Le Liu, Chao-Yang Lu, and Jian-Wei Pan. "Quantum computational advantage using photons". In: *Science* 370.6523 (Dec. 18, 2020), pp. 1460–1463. DOI: 10.1126/science.abe8770.

[102] Di Zhu, Linbo Shao, Mengjie Yu, Rebecca Cheng, Boris Desiatov, C. J. Xin, Yaowen Hu, Jeffrey Holzgrafe, Soumya Ghosh, Amirhassan Shams-Ansari, Eric Puma, Neil Sinclair, Christian Reimer, Mian Zhang, and Marko Lončar. "Integrated photonics on thin-film lithium niobate". In: *Advances in Optics and Photonics* 13.2 (June 30, 2021), pp. 242–352. DOI: 10.1364/AOP.411024.

Chapter 2

BACKGROUND ON QUANTUM, NONLINEAR, AND ULTRAFAST OPTICS

2.1 A brief introduction to continuous-variable quantum optics

We will first go over the basics of quantum optics and define the useful operators and concepts that will be central to the thesis.

We denote a pure quantum state by its state vector $|\psi\rangle$. Pure and mixed states can be described using a density matrix $\hat{\rho}$, which is in general the sum of the density matrices of pure states:

$$\hat{\rho} = \sum_n p_n |\psi_n\rangle \langle\psi_n| \,, \tag{2.1}$$

where p_n is the probability of the system to be in the state $|\psi_n\rangle$. As the density matrix has trace 1, the probabilities p_n must sum to 1. The purity of the state is $p = \mathrm{Tr}[\hat{\rho}^2]$ which simplifies to $p = \sum_n p_n^2$, which is a measure of the amount of pure states that contribute in the sum.

In the case of light, a common basis in which to describe a state is the photon-number, or Fock basis. We denote the photon number states, or Fock states, by their number as $|n\rangle$, such as $|0\rangle$ for the vacuum state and $|1\rangle$ for a single photon.

The annihilation operator $\hat{a}$ acts on a Fock state as

$$\hat{a}\,|n\rangle = \sqrt{n}\,|n-1\rangle \,. \tag{2.2}$$

The creation operator is the adjoint of the annihilation operator and acts on Fock states as

$$\hat{a}^\dagger\,|n\rangle = \sqrt{n+1}\,|n+1\rangle \,. \tag{2.3}$$

The canonical commutation relation is $[\hat{a}, \hat{a}^\dagger] = 1$.

As these operators are not Hermitian, they are not observables. Commonly measured observables of quantum light include the quadratures, which are defined as

$$\hat{x} = \frac{1}{2}(\hat{a} + \hat{a}^\dagger) \tag{2.4}$$

$$\hat{p} = \frac{1}{2i}(\hat{a} - \hat{a}^\dagger), \tag{2.5}$$

up to a normalization constant (sometimes the constant factor in front is $1/\sqrt{2}$). These can be thought of as the in-phase and out-of-phase parts of a single mode of the electromagnetic field. Arbitrary quadratures which mix these are sometimes used:

$$\hat{x}(\theta) = \hat{x}\cos\theta - \hat{p}\sin\theta \tag{2.6}$$

$$\hat{p}(\theta) = \hat{p}\cos\theta + \hat{x}\sin\theta. \tag{2.7}$$

In this normalization using natural units ($\hbar = 1$) the commutation relation for these is $[\hat{x}(\theta), \hat{p}(\theta)] = \frac{i}{2}$ for all angles θ. The vacuum variance is

$$\Delta\hat{x}^2_{\text{vac}} = \Delta\hat{p}^2_{\text{vac}} = \frac{1}{4} \tag{2.8}$$

for $\Delta\hat{x}^2 = \langle\hat{x}^2\rangle - \langle\hat{x}\rangle^2$ and $\langle\hat{A}\rangle$ denoting the expectation value over a state $|\psi\rangle$ of some operator $\hat{A}$ as $\langle\hat{A}\rangle = \langle\psi|\,\hat{A}\,|\psi\rangle$. The quadratures can take on any continuous value when they are measured, and thus they are commonly manipulated and measured in continuous-variable (CV) quantum optics.

The other most commonly measured observable is the photon number

$$\hat{N} = \hat{a}^\dagger\hat{a}. \tag{2.9}$$

Unlike the quadratures, this observable takes on discrete values when measured (as it's possible to measure only discrete numbers of photons when projecting onto the photon number basis), but adding and subtracting photons is still commonly done in CV quantum optics.

Quantum optical states can be depicted in optical phase space, using the Wigner quasi-probability distribution

$$W(\alpha) = \frac{1}{\pi^2}\int e^{\zeta^*\alpha - \zeta\alpha^*}\mathrm{Tr}[\hat{\rho}e^{\zeta\hat{a}^\dagger - \zeta^*\hat{a}}]\mathrm{d}^2\zeta, \tag{2.10}$$

where $\alpha = x + ip$ is the coordinate in the phase space spanned by the quadratures x and p, ζ is a complex number, and Tr is the trace operation. Some example Wigner functions are shown in Fig. 2.1(b-e). It is not an actual probability distribution because it can take on negative values for some quantum states, such as photons (Fig. 2.1(d)). This distribution shows the effects of Gaussian operations quite intuitively (such as the squeezing operator squeezing and stretching the distribution and the displacement operator moving the distribution around), making it a useful representation of a quantum state in CV quantum optics. In addition, Gaussian states have Wigner distributions that

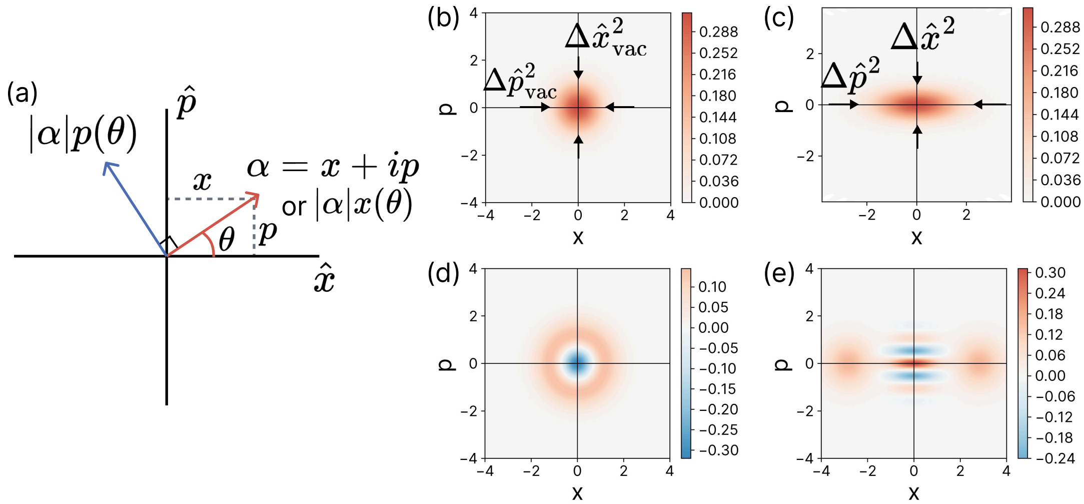

Figure 2.1: Description of phase space and example Wigner functions. (a) Phase space and two vectors in it. The space is spanned by the quadratures x and p, and a location in it α is defined by two coordinates, either the x and p values or the distance from the origin $|\alpha|$ and the direction θ. Rotating the quadratures in phase space as defined in Eqn. 2.7 is shown as well, with $x(\theta)$ and $p(\theta)$ being orthogonal to each other. (b-e) Wigner functions of (b) vacuum, (c) 4-dB squeezed vacuum, (d) a single photon, and (e) a Schrödinger's cat state ($\propto |-\alpha\rangle + |\alpha\rangle$ for $\alpha = 0.8$). The approximate vacuum quadrature variances $\Delta\hat{x}^2$ and $\Delta\hat{p}^2$ and quadrature variances of the squeezed vacuum $\Delta\hat{x}^2$ and $\Delta\hat{p}^2$ are shown in plots (b) and (c), respectively.

are two-dimensional Gaussians in this space. Finally, negativity in the Wigner function is an indicator of the usefulness of the state for quantum information processing beyond Gaussian protocols, including universal quantum computation that is accelerated beyond the capabilities of classical computers [1, 6, 10].

2.2 Nonlinear optical interactions

The polarization P of a material can be dependent nonlinearly on the electric field E which is applied to it. That is,

$$P = \varepsilon_0(\chi^{(1)}E + \chi^{(2)}E^2 + \chi^{(3)}E^3 + \dots), \tag{2.11}$$

where ε_0 is the vacuum permittivity and $\chi^{(n)}$ is the n^{th}-order nonlinear susceptibility (except for the first-order $\chi^{(1)}$, which is the linear susceptibility). The magnitudes of the susceptibilities decrease as their order increases, and thus it suffices to study the largest order which exists in the material. We focus on the second-order nonlinearity, which is present in lithium niobate which is central to this work.

A second-order nonlinear material enables three-wave mixing processes such as sum-frequency generation, in which two photons combine to form one with higher energy, and parametric down-conversion (PDC), in which one photon (the pump) becomes two (the signal and idler). We focus on PDC. Energy is conserved in PDC, as the frequencies of the signal and idler photons must sum to the frequency of the pump photon:

$$\omega_p = \omega_s + \omega_i. \tag{2.12}$$

Momentum is also conserved. The wavevectors of the photons are related to their momenta and thus must satisfy the relation

$$\mathbf{k}_p - \mathbf{k}_s - \mathbf{k}_i = 0, \tag{2.13}$$

where $\mathbf{k}$ are the momentum vectors for the pump, signal, and idler. Achieving this so-called phase-matching condition is done using many methods, but the one employed in this work is quasi-phase-matching through periodic poling [8]. In this technique, the orientation of the crystal domains are flipped at regular intervals in order to generate a first-order approximation of an additional momentum vector. This additional vector's length is proportional to the interval at which the domains are flipped, and thus periodic poling is a flexible way to satisfy this condition.

We mainly consider degenerate type-0 PDC, in which $\omega_s = \omega_i = \omega_p/2$ and the polarization of the signal, idler, and pump photons is identical. In this special case, the signal and idler are indistinguishable, and a material with $\chi^{(2)}$ implements the interaction-picture Hamiltonian

$$\hat{H} = i\kappa(\hat{a}^{\dagger 2}\hat{b} - \hat{a}^2\hat{b}^\dagger), \tag{2.14}$$

where $\hat{a}$ is the annihilation operator of the signal and idler and $\hat{b}$ is that of the pump. κ is the nonlinear coupling strength and depends on $\chi^{(2)}$. We also typically make the approximation that the pump is very strong and thus is not depleted significantly by the PDC, so that the operator $\hat{b}$ becomes a complex constant β which depends on the pump strength.

Under the undepleted-pump approximation, this Hamiltonian enacts the squeezing operator $\hat{S}(\xi) = \exp\left(\frac{1}{2}(\xi^*\hat{a}^2 - \xi\hat{a}^{\dagger 2})\right)$ on the signal state for complex squeezing parameter $\xi \propto \kappa\beta t$ for interaction time t. The input state at the signal frequency will be amplified in one quadrature and de-amplified in the other. The angle at which the state is squeezed is determined by the relative phase of the pump and signal beams. This squeezing operation amplifies the state in one quadrature and squeezes it in the orthogonal quadrature, implementing a phase-sensitive amplification. If there is no input signal, then the process is called spontaneous PDC (SPDC) the squeezing angle is determined by the relative phase of the pump and measurement laser beams for typical measurement techniques such as homodyne.

The amount of squeezing is typically reported as the ratio of the variance in the most squeezed quadrature of the state to the variance of vacuum:

$$Sq = \frac{\Delta \hat{x}^2_{\mathrm{sq}}}{\Delta \hat{x}^2_{\mathrm{vac}}} \tag{2.15}$$

and also extremely commonly reported in dB:

$$Sq_{\mathrm{dB}} = 10 \log_{10}(Sq). \tag{2.16}$$

Anti-squeezing is similarly reported as the ratio of the variance of the most anti-squeezed quadrature to that of vacuum.

The amount of squeezing for a certain amount of anti-squeezing is limited by the Heisenberg uncertainty principle, which states that for non-commuting observables (such as $\hat{x}$ and $\hat{p}$ in this case),

$$\Delta \hat{x}^2 \Delta \hat{p}^2 \geq \frac{1}{4} |\langle [\hat{x}, \hat{p}] \rangle|^2 = \frac{1}{16} \tag{2.17}$$

in our normalization. This relation implies that the absolute value of the amount of squeezing in dB cannot exceed the amount of anti-squeezing in dB. However, the amount of anti-squeezing for a certain level of squeezing has no upper bound. As the state becomes more thermalized, or mixed, the amount of squeezing decreases while the amount of anti-squeezing does not decrease as much. For a single-mode Gaussian state, the purity of the state can be written as

$$p = \frac{1}{4\sqrt{\Delta \hat{q}^2_{\mathrm{sq}} \Delta \hat{q}^2_{\mathrm{asq}}}} \tag{2.18}$$

for $\hat{q}_{\mathrm{sq}}$ being the squeezed quadrature and $\hat{q}_{\mathrm{asq}}$ being the anti-squeezed quadrature.

One way of describing squeezing is using the Heisenberg picture. In this case, the annihilation operator undergoes the Bogoliubov transform

$$\hat{a}' = \hat{a} \cosh r + \hat{a}^\dagger e^{-i\theta} \sinh r \tag{2.19}$$

where $\xi = re^{i\theta}$. It acts on the rotated quadrature operators in a particularly convenient way:

$$\hat{x}'(\theta) = e^r \hat{x}(\theta) \tag{2.20}$$

$$\hat{p}'(\theta) = e^{-r} \hat{p}(\theta) \tag{2.21}$$

When the input state is vacuum, a second-order nonlinear device such as an OPA that is phase-matched for PDC will generate squeezed vacuum when pumped at the second harmonic. In the Fock basis, squeezed vacuum takes the form of

$$\hat{S}(\xi)|0\rangle = \frac{1}{\sqrt{\cosh r}} \sum_{n=0}^{\infty} (-e^{i\theta}\tanh r)^n \frac{\sqrt{(2n)!}}{2^n n!} |2n\rangle \,, \tag{2.22}$$

which indicates that this state consists of a superposition of the even-photon-number Fock states $|2n\rangle$. For weak squeezing ($r \ll 1$), only the vacuum and two-photon contributions are significant, and we can approximate the state as a biphoton state.

For strong squeezing, the OPA acts as a phase-sensitive amplifier of only one quadrature. This can be seen when considering the photon number at the output of an OPA:

$$\hat{N} = (\hat{x}'(\theta))^2 + (\hat{p}'(\theta))^2 - \frac{1}{2} = e^{2r}\hat{x}^2(\theta) + e^{-2r}\hat{p}^2(\theta) - \frac{1}{2}. \tag{2.23}$$

For a high-gain OPA, $e^{2r} \gg \frac{1}{2} \gg e^{-2r}$ and

$$\hat{N} \approx e^{2r}\hat{x}^2(\theta), \tag{2.24}$$

so when measuring the photons using a photodetector or another photon-number measurement, only the amplified quadrature $\hat{x}(\theta)$ contributes. Most importantly, the quadrature statistics of the state are preserved, as the probability distribution of photon numbers follows

$$P(N) = \frac{e^{-r}}{\sqrt{N}} P(\hat{x}(\theta)), \tag{2.25}$$

so measuring the photon number distribution gives one-sided information (no negative values) on the distribution of the amplified quadrature, which can be used for state tomography of symmetric states like in [5].

The variance of an input state is proportional to the state's variance

$$\langle\hat{N}\rangle = e^{2r}\langle\hat{x}^2\rangle. \tag{2.26}$$

For example, an OPA can be used to measure squeezing by comparing the average photon number of the squeezed quadrature to that of vacuum, which leads to

$$\frac{\langle\hat{N}\rangle}{\langle\hat{N}_{\text{vac}}\rangle} = \frac{e^{2r}\langle\hat{x}^2\rangle}{e^{2r}\langle\hat{x}^2_{\text{vac}}\rangle} = Sq, \tag{2.27}$$

which works because both states are amplified by the same amount e^{2r}.

2.3 Multimode and ultrafast quantum light

In the pulsed regime, quantum states can be thought of as living in a temporal mode. One interpretation of these modes is that if you measure when the state arrives, it will follow a certain distribution determined by the mode. Another interpretation is that in order to measure or manipulate the state with as little loss as possible, the operation must be mode-matched (e.g. homodyne detection must use a local oscillator pulse of the same shape).

An annihilation operator can be assigned to a temporal mode shape $\psi(t)$ as

$$\hat{a}_\psi = \int \psi(t)\hat{a}(t)\mathrm{d}t, \tag{2.28}$$

where $\hat{a}(t)$ is the time-bin annihilation operator for time t. As these modes typically have significant support in both time and frequency, they are called spectrotemporal modes and can be referred to in both domains. For example $\hat{a}_\psi$ can also be written as

$$\hat{a}_\psi = \int \psi(\omega)\hat{a}(\omega)\mathrm{d}\omega, \tag{2.29}$$

where $\psi(\omega) = \mathfrak{F}\{\psi(t)\}$ and $\hat{a}(\omega)$ is the frequency-dependent annihilation operator. In this thesis these modes may also be called temporal modes.

A broadband OPA pumped by an ultrafast pulse is typically multimode [11], which means it emits squeezed light in many spectrotemporal modes. These modes each act as a separate OPA that enacts the Bogoliubov transform on that temporal mode as

$$\hat{a}_n^{\mathrm{out}} = \hat{a}_n^{\mathrm{in}} \cosh r_n + \hat{a}_n^{\mathrm{in}\dagger} e^{-i\theta_n} \sinh r_n, \tag{2.30}$$

for input modes

$$\hat{a}_n^{\mathrm{in}} = \int \psi_n^{\mathrm{in}}(t)\hat{a}(t)\mathrm{d}t \tag{2.31}$$

and output modes

$$\hat{a}_n^{\mathrm{out}} = \int \psi_n^{\mathrm{out}}(t)\hat{a}(t)\mathrm{d}t. \tag{2.32}$$

These modes can be thought of as the eigenmodes of the OPA's squeezing transformation. If an input pulse is sent in an input eigenmode, then the output will be in a single output eigenmode. In general, the input and output modes of an OPA are different, but in the special case where the pump is unchirped (has a flat spectral phase) in the center of the OPA, then the modes become complex conjugates of each other in the frequency domain ($\psi_n^{\mathrm{out}}(\omega) = \psi_n^{\mathrm{in}*}(\omega)$), or time-reversed with respect to each other in the time-domain

[11]. Due to the requirement of satisfying the commutation relation $[\hat{a}_m, \hat{a}_n^\dagger] = \delta_{mn}$, these modes are orthonormal and satisfy the relation

$$\int \psi_m^{\text{in}}(t)\psi_n^{\text{in}*}(t)\mathrm{d}t = \int \psi_m^{\text{out}}(t)\psi_n^{\text{out}*}(t)\mathrm{d}t = \delta_{mn} \tag{2.33}$$

for δ_{mn} being the Kronecker delta.

The shape of the modes can be determined by performing a Schmidt or singular value decomposition (SVD) and diagonalizing the joint spectral amplitude (JSA) $J(\omega_s, \omega_i)$. The JSA is a complex function of the signal and idler frequencies that governs the spectral distribution of creation of pairs of photons in PDC, and the interaction Hamiltonian in this broadband case is

$$\hat{H}_{\text{int}} \propto \iint J(\omega_s, \omega_i)\hat{a}^\dagger(\omega_s)\hat{a}^\dagger(\omega_i)\mathrm{d}\omega_s \mathrm{d}\omega_i + \text{h.c.} \tag{2.34}$$

In the weak-squeezing biphoton regime, the JSA governs the frequency correlations between the emitted photons:

$$|\Psi_{\text{SPDC}}\rangle = |00\rangle + \iint J(\omega_s, \omega_i)\,|1_{\omega_s}1_{\omega_i}\rangle\,\mathrm{d}\omega_s \mathrm{d}\omega_i, \tag{2.35}$$

up to a normalization constant, where $|00\rangle$ is the vacuum state and $|1_{\omega_s}1_{\omega_i}\rangle$ is the biphoton state with photons at frequencies ω_s and ω_i.

The JSA can be approximated in the low-gain regime as the product between the phase-matching condition $\Phi(\Delta k(\omega_s, \omega_i))$, where $\Delta k(\omega_s, \omega_i)$ is the phase mismatch, and the energy-conservation condition $\alpha(\omega_s + \omega_i)$. The phase-matching term is typically of the form $e^{i(k(\omega_s)-k(\omega_i))L/2}\,\text{sinc}(L\Delta k/2)$ for an OPA of length L. The energy-conservation condition's form depends on the shape and frequency of the pump, as it exists to ensure that $\omega_s + \omega_i = \omega_p$, and typically it is a Gaussian shape smeared along the anti-diagonal of the frequency correlation matrix. A simulated example of these matrices can be seen in Figs. 2.2(a-c) for a waveguide OPA on thin-film lithium niobate with waveguide top width 900 nm, thin-film thickness 680 nm, and etch depth of 420 nm.

To identify the principal modes of the system in the weak squeezing limit, we perform a Schmidt decomposition on the biphoton state. Mathematically, this is equivalent to performing an SVD on the JSA. The resulting singular vectors define the orthonormal basis of spectrotemporal supermodes, while the singular values determine the weight and squeezing level of each individual mode. Performing an SVD on the JSA yields three matrices:

$$J = U\Sigma V^\dagger, \tag{2.36}$$

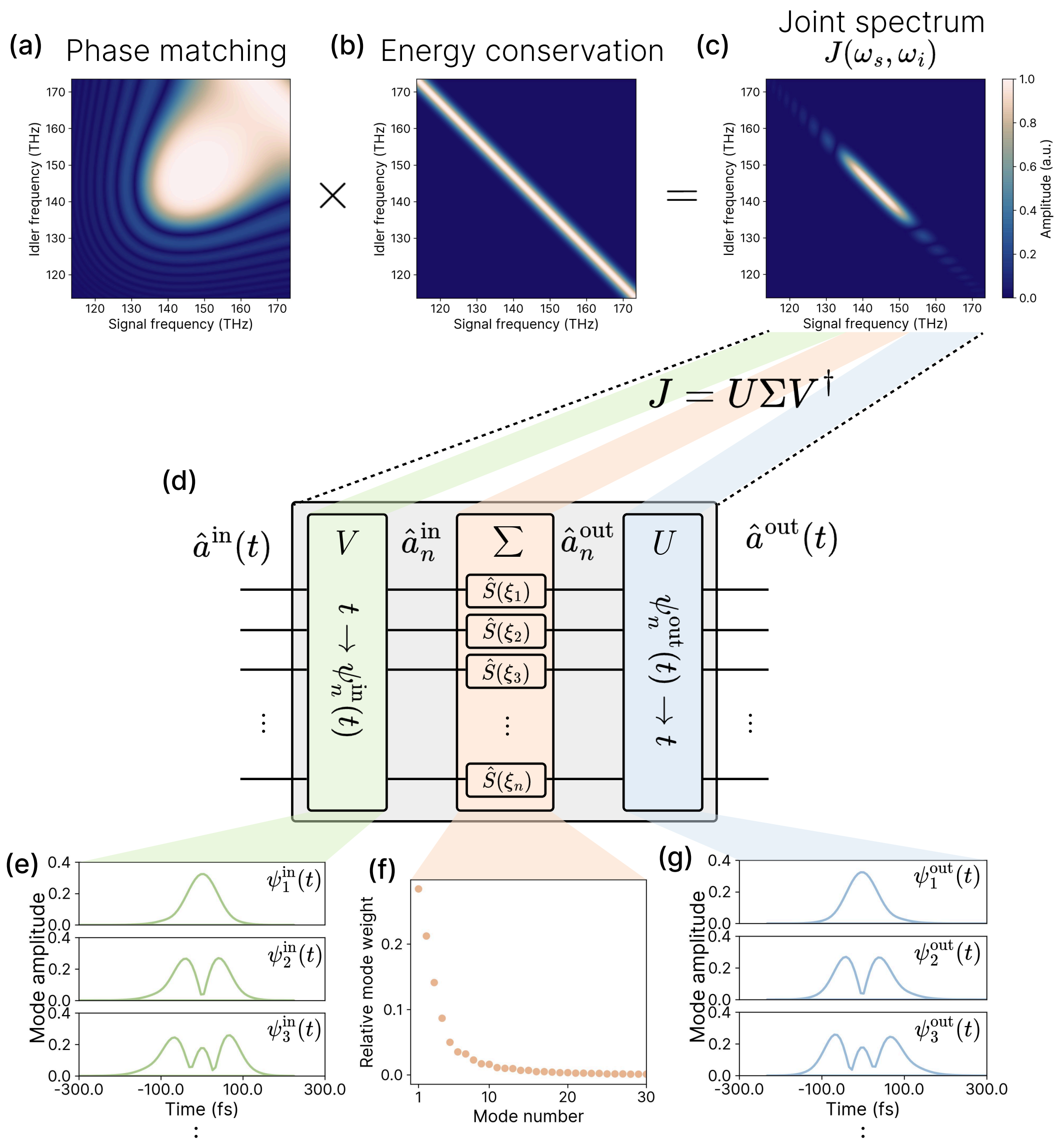

Figure 2.2: Simulated joint spectral amplitude of a broadband OPA in the low-gain regime and its singular value decomposition. (a) The phase-matching term $\Phi(\Delta k(\omega_s, \omega_i)) = \mathrm{sinc}(\Delta k L/(2\pi))$ for a waveguide OPA in thin-film lithium niobate with waveguide top width 900 nm, thin-film thickness 680 nm, and etch depth of 420 nm. (b) Energy conservation term $\alpha(\omega_s + \omega_i)$ for a 100-fs Gaussian pump centered at 1045 nm. (c) Joint spectral amplitude $J(\omega_s, \omega_i) = \Phi(\Delta k(\omega_s, \omega_i))\alpha(\omega_s + \omega_i)$, which is valid in the low-gain regime. (d) Breakdown of how the JSA describes the action of a multimode OPA. The matrices U and V describe the output and input mode shapes, respectively, and the diagonal matrix Σ contains the squeezing parameters ξ_n. (e) The input modes for the OPA. (f) The relative mode weights. (g) The output modes.

where the columns of U contain the output modes (or rather, the linear transformation between the frequency basis and the output mode basis) and the columns of V contain the input modes (also a linear transformation). Σ is a diagonal matrix containing the singular values, which are equal to the squeezing parameters $\sigma_n = r_n = |\xi_n|$, along the diagonal, which, in the weak-squeezing regime is approximately the square root of the mode energy $\sinh^2 r_n$. An illustration of these matrices' roles in the characterization of the broadband OPA and some example modes are shown in Figs. 2.2(d-g). In the weak-squeezing regime, these input and output modes are equivalent to the signal and idler modes of the photons [11].

The Schmidt number K and its inverse, the spectral purity $p_s = 1/K$, are measures of the effective number of modes populated in a multimode squeezed state generated by an OPA. Because there are a theoretically infinite number of modes being emitted, and each mode's contribution to the output state can vary dramatically. Rather than set a cutoff, we would like to see how single- or multimode a state is based on the distribution of the squeezing parameters encoded in Σ. The Schmidt number is defined as

$$K = \frac{\left(\sum_n \sinh^2 r_n\right)^2}{\sum_n \sinh^4 r_n} \approx \frac{\left(\sum_n r_n^2\right)^2}{\sum_n r_n^4} = \frac{\left(\sum_n \sigma_n^2\right)^2}{\sum_n \sigma_n^4} \tag{2.37}$$

where the approximation holds for small squeezing values $r_n \ll 1$ [4]. The purity is equivalent to the purity of a single photon that is heralded by detecting the other photon of a biphoton state generated by weakly pumping the OPA. It is important to note that the effective number of modes K is gain-dependent. In the high-gain regime, the exponential nature of parametric amplification (the $\sinh^2$) leads the primary Schmidt modes dominating the state, reducing the number of modes compared to the low-gain regime.

In addition to describing the number of populated eigenmodes, K is also used to quantify the amount of entanglement present in the system. If $K = p_s = 1$, then the signal and idler photons are uncorrelated and unentangled, and the state is single-mode and no entanglement can be generated from this state alone. The higher K is and the lower p_s is, the more entanglement is present in the system. The entropy of entanglement of such a state is related to the squeezing parameters through

$$S = -\sum_n \lambda_n \log_2 \lambda_n, \tag{2.38}$$

where $\lambda_n \equiv \sinh^2 r_n / \sum_{n'} \sinh^2 r_{n'}$ are the normalized eigenvalues [7, 12].

In order to characterize a multimode Gaussian state (one whose Wigner distribution is Gaussian), it is sufficient to know its covariance matrix and displacement vector. The covariance matrix in terms of quadrature operators is defined as

$$C_{ij} = \frac{1}{2}\langle\{\Delta\hat{q}_i, \Delta\hat{q}_j\}\rangle \tag{2.39}$$

for $\hat{q} \in \{\hat{x}_n, \hat{p}_n\}$ for all modes n and $\{,\}$ denoting the anticommutator. The covariance matrix contains information about the second-order moments of the state. It also contains information about the purity of the state. The more general form of Eqn. 2.18 for multimode Gaussian states is

$$p = \frac{1}{\sqrt{\det C}} \tag{2.40}$$

where det signifies the determinant of a matrix.

Because squeezed states are Gaussian, a multimode squeezed state always has a basis in which the modes are uncorrelated, or, equivalently, in which the covariance matrix is diagonal [2]. This basis is called the principal basis and is important for measuring and manipulating these multimode states. For a covariance matrix that is diagonal, 2.40 simplifies to

$$p = \prod_n \frac{1}{\sqrt{\Delta\hat{q}^2_{\mathrm{sq},n}\Delta\hat{q}^2_{\mathrm{asq},n}}}, \tag{2.41}$$

which is the product of the purity of the state in each mode n. Note that the spectral purity is separate from the state's purity, and a multimode state that has low spectral purity (i.e. contains many modes) may have high purity if the state in each mode has high purity. The reverse is also true, in that a single-mode state has high spectral purity but may be a very mixed state with low purity.

The displacement vector is

$$D_i = \langle\hat{q}_i\rangle \tag{2.42}$$

and measures the displacement of the state from the origin, which is the first-order moment. Because the state is Gaussian, no information about higher-order moments is necessary. In this thesis we will mainly concern ourselves with the characterization of zero-mean-field states, whose displacement vectors are all zero. This is because using a phase-sensitive amplifier such as an OPA followed by a photodetector to measure the quadrature of a state measures $\hat{x}^2$ rather than $\hat{x}$ as homodyne typically does. Thus, full knowledge of the state is only obtained through this measurement if the state is mirror symmetric about two perpendicular axes going through the origin in phase space (e.g.

the x and p axes and their rotations), and this constraint leads to the zero-mean-field assumption. Luckily, many important Gaussian and non-Gaussian states such as vacuum, Fock states, squeezed vacuum, and Schrödinger's cat states all satisfy this constraint.

Non-Gaussian states require information about higher-order moments, and characterizing the Wigner function requires the full probability distribution along many directions in phase space. Quantum state tomography using these probability distributions is the most general method of characterizing a state in phase space, and has been used using inverse methods such as maximum likelihood estimation to determine the state's density matrix [9]. These states can be intrinsically entangled, in which there is no basis in which the modes are uncorrelated. Some examples of non-Gaussian states are single photons and Schrödinger's cat states.

2.4 Quantum detector tomography

A quantum detector can be defined by its positive operator-valued measure (POVM), which is a collection of Hermitian matrices $\{\hat{\Pi}_n\}$ for which

$$\sum_n \Pi_n = \mathbb{1} \tag{2.43}$$

and each matrix is positive semi-definite. They define measurement results, labeled by n, for which the probability of obtaining the result n when measuring a state $\hat{\rho}$ is given by $\mathrm{Tr}\left[\hat{\rho}\hat{\Pi}_n\right]$. The elements $\hat{\Pi}_n$ are not necessarily orthogonal, and the number of elements can be different than the dimension in which they act.

The POVM does not give enough information to obtain the state after measurement. This is because a POVM is the most general description of a measurement. The information about the output state is given by the projection valued measure (PVM) which is actually happening. Much like a pure state generalizes to a mixed state, a POVM gan be thought of as the action of a PVM onto a subsystem of a quantum state. The POVM elements can be decomposed into

$$\hat{\Pi}_n = \hat{A}_n^\dagger \hat{A}_n. \tag{2.44}$$

However, it can be seen that substituting $\hat{A}_n \to U\hat{A}_n$ for any unitary U preserves the equality and thus $\hat{A}_n$ is only defined up to this unitary. The exact unitary can be found by considering the entire PVM.

For some expansion into $\hat{A}_n$, the state after measuring state $\hat{\rho}$ and obtaining result n will be

$$\hat{\rho}' = \frac{\hat{A}_n \hat{\rho} \hat{A}_n^\dagger}{\mathrm{Tr}\left[\hat{A}_n \hat{\rho} \hat{A}_n^\dagger\right]}. \tag{2.45}$$

Performing quantum detector tomography by determining the POVM of a quantum measurement is the most complete way of characterizing a detection system. One way of doing so [3] is to send in a known informationally complete ensemble of states and use the measurement results to invert the following equation:

$$P_{n,\alpha} = \mathrm{Tr}\left[\hat{\rho}_\alpha \hat{\Pi}_n\right] \tag{2.46}$$

where α labels the different states (in anticipation of the fact that most states used for quantum detector tomography are coherent states) and $P_{n,\alpha}$ is the probability of measuring result n from state α, which can be obtained experimentally. Inverting this equation is commonly done using convex optimization, because the requirements of satisfying the above equation, Eqn. 2.43, and that of the matrices being Hermitian and positive semi-definite lend themselves well to this technique. If the measurement is not phase sensitive (such as single-photon detection), then it suffices to measure the diagonals of the POVM matrices, as the off-diagonals are zero. However, for a phase-sensitive measurement, entire matrices must be retrieved.

It is interesting to note that although the probe states may be coherent and thus exhibit no quantum behaviors, as long as they cover the relevant parts of phase space, full quantum information about the detector can be obtained.

References

[1] Francesco Albarelli, Marco G. Genoni, Matteo G. A. Paris, and Alessandro Ferraro. "Resource theory of quantum non-Gaussianity and Wigner negativity". In: *Physical Review A* 98.5 (Nov. 28, 2018), p. 052350. DOI: 10.1103/PhysRevA.98.052350.

[2] C. Fabre and N. Treps. "Modes and states in quantum optics". In: *Reviews of Modern Physics* 92.3 (Sept. 10, 2020), p. 035005. DOI: 10.1103/RevModPhys.92.035005.

[3] A Feito, J S Lundeen, H Coldenstrodt-Ronge, J Eisert, M B Plenio, and I A Walmsley. "Measuring measurement: theory and practice". In: *New Journal of Physics* 11.9 (Sept. 28, 2009), p. 093038. DOI: 10.1088/1367-2630/11/9/093038.

[4] Martin Houde and Nicolás Quesada. "Waveguided sources of consistent, single-temporal-mode squeezed light: the good, the bad, and the ugly". In: *CLEO 2023 (2023), paper FF1L.6*. CLEO: Fundamental Science. Optica Publishing Group, May 7, 2023, FF1L.6. DOI: 10.1364/CLEO_FS.2023.FF1L.6.

[5] Mahmoud Kalash and Maria V. Chekhova. "Wigner function tomography via optical parametric amplification". In: *Optica* 10.9 (Sept. 20, 2023), p. 1142. DOI: 10.1364/OPTICA.488697.

[6] Anatole Kenfack and Karol Życzkowski. "Negativity of the Wigner function as an indicator of non-classicality". In: *Journal of Optics B: Quantum and Semiclassical Optics* 6.10 (Aug. 2004), p. 396. DOI: 10.1088/1464-4266/6/10/003.

[7] C. K. Law, I. A. Walmsley, and J. H. Eberly. "Continuous Frequency Entanglement: Effective Finite Hilbert Space and Entropy Control". In: *Physical Review Letters* 84.23 (June 5, 2000), pp. 5304–5307. DOI: 10.1103/PhysRevLett.84.5304.

[8] Luis Ledezma, Ryoto Sekine, Qiushi Guo, Rajveer Nehra, Saman Jahani, and Alireza Marandi. "Intense optical parametric amplification in dispersion-engineered nanophotonic lithium niobate waveguides". In: *Optica* 9.3 (Mar. 20, 2022), p. 303. DOI: 10.1364/OPTICA.442332.

[9] A. I. Lvovsky. "Continuous-variable optical quantum-state tomography". In: *Reviews of Modern Physics* 81.1 (2009), pp. 299–332. DOI: 10.1103/RevModPhys.81.299.

[10] A. Mari and J. Eisert. "Positive Wigner Functions Render Classical Simulation of Quantum Computation Efficient". In: *Physical Review Letters* 109.23 (Dec. 4, 2012), p. 230503. DOI: 10.1103/PhysRevLett.109.230503.

[11] Wojciech Wasilewski, A. I. Lvovsky, Konrad Banaszek, and Czesław Radzewicz. "Pulsed squeezed light: Simultaneous squeezing of multiple modes". In: *Physical Review A* 73.6 (June 20, 2006), p. 063819. DOI: 10.1103/PhysRevA.73.063819.

[12] Kevin Zielnicki, Karina Garay-Palmett, Daniel Cruz-Delgado, Hector Cruz-Ramirez, Michael F. O'Boyle, Bin Fang, Virginia O. Lorenz, Alfred B. U'Ren, and Paul G. Kwiat. "Joint Spectral Characterization of Photon-Pair Sources". In: *Journal of Modern Optics* 65.10 (June 7, 2018), pp. 1141–1160. DOI: 10.1080/09500340.2018.1437228. arXiv: 1801.01195[quant-ph].

C h a p t e r 3

ULTRAFAST SINGLE-PHOTON DETECTOR BASED ON A NANOPHOTONIC PARAMETRIC AMPLIFIER

[1] Elina Sendonaris*, James Williams*, Rajveer Nehra, Robert Gray, Ryoto Sekine, Luis Ledezma, and Alireza Marandi. "Ultrafast single-photon detector based on a nanophotonic parametric amplifier". In: *Physical Review Applied* 25.4 (Apr. 27, 2026), p. 044078. DOI: 10.1103/c58l-h1gh.

ABSTRACT

Integrated photonic quantum information processing (QIP) has advanced rapidly due to progress in various nanophotonic platforms. Single-photon detectors have been the subject of intense study due to their ubiquity in QIP systems, yet many detectors operate at cryogenic temperatures under vacuum and are limited in operating speed by their dead times. We propose and characterize an all-optical single-photon detection scheme based on optical parametric amplification in nanophotonic lithium niobate (LN) combined with a macroscopic photodetector. We use quantum detector tomography and experimentally determine the positive operator-valued measure of the detector. The detector operates at room temperature at a count rate of 250 MHz and is readily integrated in LN nanophotonics. While the demonstrated experimental performance falls short of existing photon detectors, we show that in the future, by improving the nonlinearity-to-loss ratio and using homodyne detection on a squeezed pump, the detector can achieve a performance sufficient to create non-Gaussian states, such as Schrödinger's cat states. Our results highlight a path towards all-optical photon detection for scalable high-throughput nanophotonic quantum communication and information processing.

3.1 Introduction

Photonic QIP has been the subject of intense research, due to photons' long coherence time and their minimal interaction with thermal noise [37]. In particular, temporal multiplexing schemes have been of interest due to their scalability while using minimal spatial modes [2, 24, 33] and the use of time as a synthetic dimension [4], in addition to the ease of interfacing with optical quantum communication. Single-photon detectors (SPDs) are the most widely used detectors in photonic QIP, for both determining the outcome of a computation in discrete-variable (DV) QIP [21, 37] and for generating non-Gaussian states, necessary for universal continuous-variable (CV) QIP [3, 30], such as Schrödinger cat and kitten states [38] and GKP states [15, 22].

Some of the most widely used single-photon detectors include superconducting nanowire single-photon detectors (SNSPDs) [13], transition-edge sensors (TESs) [29], and single-photon avalanche diodes (SPADs) [6]. SNSPDs benefit from their high efficiency (over 99%) [7, 40], low dark count rates [8], short timing jitter (as low as 3 ps) [23], and high count rates up to the GHz level [41, 54]. TESs can distinguish between different numbers of photons, up to 100 [12], while having high efficiencies but have a longer reset time and timing jitter compared to SNSPDs [25]. SPADs operate at room temperature and atmospheric pressure and have been operated at 2.5 GHz [17] but tend to have higher dark count rates and lower efficiencies than SNSPDs [6]. These technologies are highly optimized for their respective operating regimes and represent mature, continuously improving platforms.

Using an alternative scheme for single-photon detection, such as homodyne detection [16], is a promising direction for circumventing some of these problems with current detectors, such as the speed limitations. Crucially, any new detector must retain the most important characteristic of projecting the incoming state onto the single-photon state.

Moving QIP systems to integrated photonics is of growing interest due to the stability and compactness of the components and their scalability [27, 43, 55]. Spatial confinement in nanophotonics combined with dispersion engineering enables utilization of ultrashort pulses and provides higher peak intensity, leading to higher nonlinear interaction efficiencies. Quantum photonics can benefit from the low loss and strong light-matter interaction offered by integrated platforms [34, 46]. Recently, nanophotonic optical parametric amplifiers (OPAs) with gains of 100 dB/cm have been demonstrated [26], opening up new avenues for quantum state engineering and measurement [19, 36, 48, 53]. Currently, single photons on photonic chips are detected by either outcoupling them to SPDs off chip

[1] or integrating the detector onto the photonic chip and placing it in a cryostat [42, 45]. Unfortunately, outcoupling photons from a chip leads to a lower total detection efficiency due to the outcoupling loss, and integrating an SNSPD onto a photonic chip creates fabrication and performance challenges due to the cryogenic operating temperatures.

In this work, we utilize a high-gain nanophotonic optical parametric amplifier (OPA) to experimentally realize an all-optical room-temperature single-photon OPA detector (OPAD) and analyze its prospects for QIP. We experimentally implement such a detector using a periodically poled thin-film lithium niobate (TFLN) waveguide OPA pumped by a mode-locked laser and a fast InGaAs photodetector (PD). We analyze the PD OPAD's performance using the positive operator-valued measure (POVM) framework and quantum detector tomography [14] to extract the efficiency and dark count rate.

Current experimental limitations do not allow for a high-performance OPAD, limiting its efficiency and dark count rate because it is a Gaussian operation and not able to impart Wigner negativity. The PD OPAD is not intended to outperform SNSPDs, TESs, or SPADs in efficiency or dark counts. Rather, it targets a complementary on-chip room-temperature high-throughput regime, accepting the tradeoffs of using a fundamentally Gaussian operation while taking advantage of the benefits of using a macroscopic photodetector and integrated OPA. These include a potentially higher speed of operation and time-gated operation, which mitigates dark counts arising from amplified vacuum and stray photons and allows for resolution of photons in neighboring time-bins, at the cost of not detecting photons when the pump is absent. The current efficiency and dark count limitations of the OPAD cannot be substantially improved within a purely Gaussian architecture but rather by extending operation into the non-Gaussian regime.

We also propose, as a path to non-Gaussian operation, an advanced variant we call the homodyne detector (HD) OPAD, which achieves an efficiency on par with current single-photon detectors, based on the quantum non-demolition (QND) scheme from [53]. Through simulations, we show that Schrödinger's kitten states can be created using an HD OPAD for photon subtraction from squeezed vacuum. We discuss the experimental advancements needed for implementing this version of the detector in the near future, such as creating single-mode OPAs [52] and increasing the nonlinearity-to-loss ratio [31]. These two detectors show how to extend the utilization of high-gain integrated waveguide OPAs into single-photon detection and further the process of integrating ultrafast optical QIP.

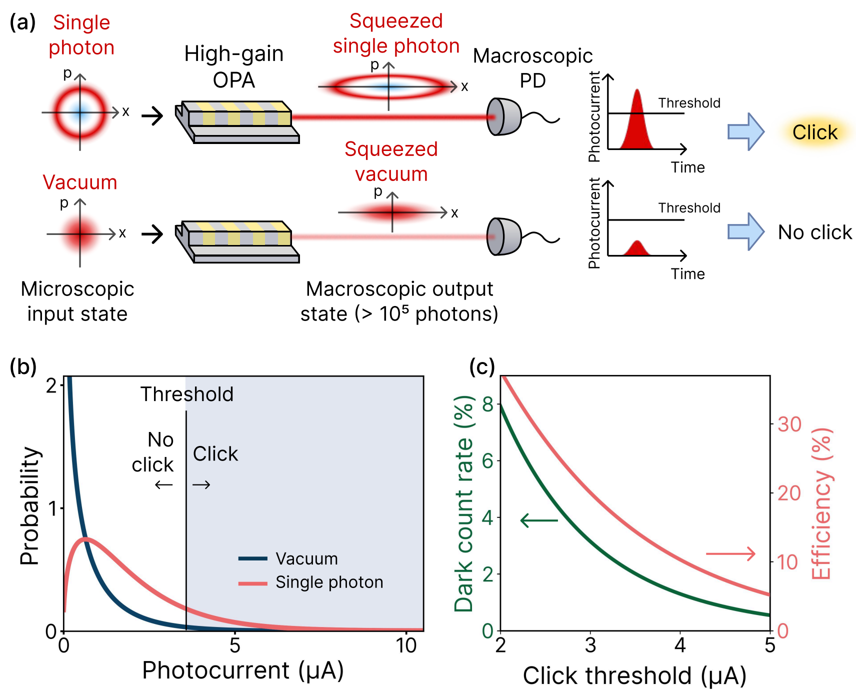

Figure 3.1: Detecting photons with an OPA and a macroscopic photodetector. (a) The concept of the single-photon OPAD. A microscopic quantum state is amplified in a waveguide OPA to levels detectable by a macroscopic PD. A threshold is applied to the detected pulse to categorize the signal as single photon or vacuum. (b) Simulated photocurrent distribution from a PD when the input to the OPA is vacuum (dark blue) or a single photon (red). An example click threshold is shown. (c) Simulated dark count rate (green) and efficiency (red) as a function of photocurrent click threshold.

3.2 Photodetector OPAD Theory

Figure 3.1(a) shows the concept of the OPAD, which uses an OPA followed by a macroscopic photodetector. We define the criteria for a click, as shown in Fig. 3.1(b), to be a threshold in the photocurrent. The photocurrent distributions were calculated for an OPA with 50 dB of gain and for photons at 2.09 µm. The laser repetition rate is 250 MHz, and the PD responsivity is 1.09 A/W. In Fig. 3.1(c), we show how the single-photon detection efficiency and dark count rate are affected by the threshold photocurrent.

In order to more precisely describe the OPAD, which is a phase-sensitive detector due to the phase-sensitive amplification of the OPA, we use the POVM framework, which fully describes any quantum detector [14]. The efficiency and dark count rate are found in the POVM elements of the click detector, as we will show. The POVM of a PD OPAD with imperfect efficiency and Gaussian electronic noise, following [9], is

$$\Pi_n = \sum_{m\geq 0} P(n|m)\hat{S}^\dagger(\xi)\left|m\right\rangle\left\langle m\right|\hat{S}(\xi) \tag{3.1}$$

where $P(n|m)$ is the probability that the PD will register n photons when m photons arrive at the detector. We assume that the OPA is operating at degeneracy in the low pump-depletion, linear gain regime, so that it implements the single-mode squeezing operator $\hat{S}(\xi)$, for squeezing parameter ξ. $P(n|m)$ depends on the PD's efficiency η and sources of Gaussian noise as

$$P(n|m) = \sum_{q\geq 0} P_\sigma(n|q)P_\eta(q|m), \tag{3.2}$$

where

$$P_\sigma(n|q) = \exp\left(\frac{-(n-q)^2}{2\sigma^2}\right) \tag{3.3}$$

is the probability of detecting n photons given q photons arrived at the detector and there is Gaussian noise with standard deviation σ, representing the electronic noise. The term

$$P_\eta(q|m) = \frac{m!}{q!(m-q)!}\eta^q(1-\eta)^{m-q} \tag{3.4}$$

is the probability that q photons are detected after m photons pass through a beam-splitter with transmission η, which models the finite efficiency $\eta \leq 1$ of the PD.

This photon number based POVM model represents the most pertinent aspects of a macroscopic PD. In order to convert photon number to photocurrent, which is the measured quantity, one can multiply the photon number by a constant conversion factor $E_{ph}f_{rep}R$, with E_{ph} the photon energy, f_{rep} the repetition rate if using a mode-locked laser, and R the photodetector responsivity. The lack of photon number resolution of macroscopic PDs comes from the large width of the Gaussian noise.

We model a click detector by setting a threshold number of photons N_{th} above which the detector registers a click. Then, the click POVM is

$$\Pi_{\text{click}} = \sum_{n\geq N_{th}} \Pi_n \tag{3.5}$$

and $\Pi_{\text{no click}} = \mathbf{1} - \Pi_{\text{click}}$. The probability of getting result k is $p_k = \text{Tr}(\rho\Pi_k)$, so the single-photon efficiency is the (1,1) matrix element of Π_{click} in the Fock basis, and the dark count rate is the (0,0) element of the same matrix. All the summations are over all photon numbers, but for computational purposes it suffices to sum over photon numbers within the range where there is significant probability density based on the squeezing parameter and noise standard deviation.

When the macroscopic detection system is simply a photodetector, the performance of the OPAD is limited by how well the system can distinguish between vacuum and a single photon, which is not perfect due to the Gaussian noise erasing the parity information of those states. However, a squeezed single photon has more probability distributed at high photon numbers, and hence photocurrent, than squeezed vacuum does. Therefore, setting the threshold involves a trade off between two sought-after qualities in a single-photon detector: low dark counts, which occur when measuring the amplified vacuum results in a photocurrent above the threshold and causes a click; and high photon detection efficiency, which is the probability that measuring a squeezed single photon results in a click. This trade-off can be seen in Fig. 3.1(c). In the high-gain linear squeezing regime, a PD OPAD is equivalent to setting a threshold on a quadrature measurement. This is a fundamentally Gaussian operation and cannot impart any Wigner negativity on a Gaussian state. Even though the PD OPAD can distinguish imperfectly between vacuum and a single photon due to their different phase-space distributions, it cannot project a state onto the single-photon subspace well enough to create a non-Gaussian state, for example through photon subtraction. Moving to an alternative architecture like the HD OPAD is one path towards non-Gaussian operation.

It is also important to note that the gain of the OPA has almost no effect on the performance; as long as the detector noise is high enough to erase parity information (as it almost always is) and the gain of the OPA is high enough to amplify the signal above the PD's noise floor, then the performance follows Fig. 3.1(b) but with a scaling factor on the photocurrent.

The dark count rate is here presented as a percentage due to the time-gated nature of the OPAD, which amplifies vacuum as well as any signal when the pump is present. Thus, the specific dark count rate depends on the rate of detection and thresholding, with typical rates being very large by the standards of current SPDs [8]. For example, in the case of a typical mode-locked laser repetition rate of 250 MHz, a 4% dark count rate would lead to a dark count rate of 10^7 counts per second. The dark count rate-efficiency tradeoff cannot be eliminated without moving to a non-Gaussian architecture such as the HD OPAD, which we give the details of in Section 3.5.

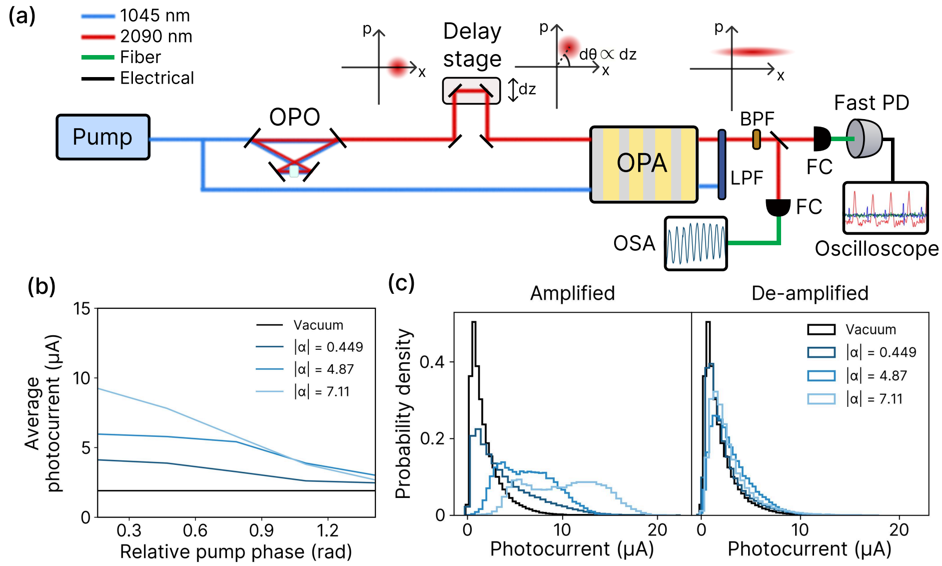

Figure 3.2: Experimental quantum tomography of an OPA-based detector. (a) Experimental setup for quantum tomography, including Wigner functions of the generated coherent and coherent squeezed states (not to scale). BPF: band-pass filter; LPF: low-pass filter; PD: photodetector; FC: fiber coupler; OSA: optical spectrum analyzer. (b) Average photocurrent of pulses as a function of coherent state angle. (c) Histogram of the pulse photocurrents for amplified and de-amplified coherent states and vacuum.

3.3 Experimental realization of phototdetector OPAD

Experimental setup

Using quantum detector tomography [14, 32, 35], we characterized an OPAD made up of an integrated TFLN waveguide OPA (2.4-mm long) and an InGaAs photodetector, as shown in Fig. 3.2(a). The waveguide was dispersion engineered for minimal group velocity mismatch between the signal and the pump and for minimal group velocity dispersion at the signal's and pump's frequencies [26].

The TFLN chip has a thickness of 700 nm, waveguide etch depth of 345 nm, and width of 1.85 μm. The poling period is 5.22 μm. We estimate that the group velocity mismatch between the fundamental and second harmonic is 5.2 fs/mm, and the group velocity dispersion at the fundamental is 120.1 fs^2/mm and at the second harmonic it is 28.4 fs^2/mm.

We characterized the chip's gain and output coupling by measuring the OPG power as a function of pump power. We did so by blocking the signal path from the OPO and adjusting the pump power using a half-wave plate and polarizing beam-splitter. The data we collected is shown in Fig. 3.3. The equation we fit to is

$$P_{OPG,off} = \hbar\omega_s \eta_{OC} f_{rep} \sinh^2(L\sqrt{\eta_{NL}\eta_{IC}P_{pump,off}}) \tag{3.6}$$

$$\approx \frac{\hbar\omega_s \eta_{OC} f_{rep}}{4} e^{2L\sqrt{\eta_{NL}\eta_{IC}P_{pump,off}}}, \tag{3.7}$$

where the last approximation is in the large-gain regime. $P_{OPG,off}$ is the OPG power off-chip, $P_{pump,off}$ is the pump power off-chip, η_{OC} is the output coupling efficiency of the chip, η_{IC} is the input coupling efficiency, ω_s is the signal frequency, f_{rep} is the laser repetition rate, L is the length of the OPA, and η_{NL} is the normalized second harmonic efficiency. We fit to a linearized version of the equation, $\ln(P_{OPG,off}) = \ln(\hbar\omega_s\eta_{OC}f_{rep}/4) + 2b\sqrt{P_{pump,off}}$. We find $\eta_{OC} = 0.102$ and $b = L\sqrt{\eta_{NL}\eta_{IC}} = 16.3$ with standard deviations of the fit $\sigma_{\eta_{OC}} = 0.027$ and $\sigma_b = 0.328$. Thus, the output coupling loss is 9.9 dB. The transmission loss through the chip is 25 dB, which leads to an input coupling loss of approximately 15.1 dB. This is likely due to the mode mismatch between the output of the reflective objective and the waveguide. We find $\eta_{NL} = (1.46 \pm 0.06) \times 10^5$ W^{-1}cm^{-2}.

We sent coherent states of known amplitude and phase created by an optical parametric oscillator (OPO) into the OPAD to gather data for POVM reconstruction, as is typical for characterizing single-photon detectors [14]. We pumped both the OPO and the OPAD with 75-fs pulses at 1.045 μm at 250 MHz from a mode-locked laser. The coherent states' amplitudes were adjusted with a neutral density filter.

To reduce the multi-mode effects in the amplified light and filter the pump out, we used a 48-nm bandwidth band-pass filter centered at 2.09 μm. In addition to this filter, we used one 1330-nm long-pass filter and two 1500 nm long-pass filters, which provided 150 dB of total pump rejection. Both the coherent states and the pump pulses were coupled onto the chip using a reflective objective and outcoupled onto a tapered single-mode fiber.

Using a 90/10 beam-splitter, we recorded both the individual pulse photocurrent amplitudes and a slower signal from an optical spectrum analyzer (OSA) containing the amplification and de-amplification envelope of the signal (amp/de-amp) as the coherent state's phase was swept. The pulse data was recorded using an InGaAs photodetector with an 18 GHz bandwidth with an 80Gs/s 40GHz oscilloscope, enough to resolve individual electronic pulses. The amp/de-amp curve from the OSA was used to determine the phase θ of the coherent state relative to the pump. The phase θ is scanned by tuning the

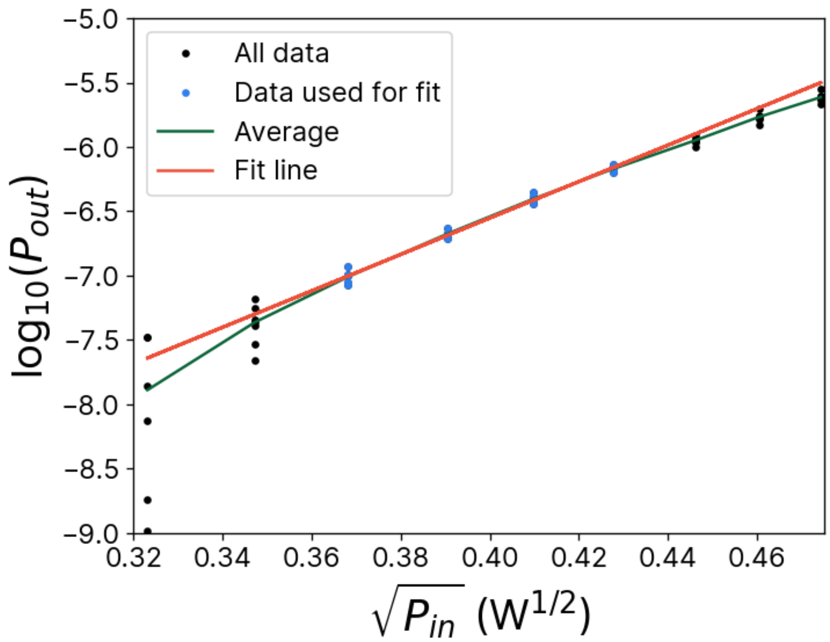

Figure 3.3: OPG power as a function of pump power. We used a subset of the data which is in the undepleted pump regime and also with high enough power to consistently register on our detector, shown in blue. The average power is shown as the green line for illustration purposes. The fit equation with the parameters we found is shown in red.

delay (dz) in the experiment, wherein $\theta = 0$ corresponds to the amplification quadrature and $\theta = \pi/2$ corresponds to the de-amplification quadrature for the OPA.We recorded data from over 4 million pulses and collected over 140,000 pulses of optical parametric generation (OPG) data, in which the signal is the vacuum state.

In order to characterize the amplitude of the coherent states on-chip, we sent the pulses into an SNSPD optimized for operation at 2 μm. Knowing the chip output loss from OPG measurement and the loss from the filters allowed us to calculate the amplitude from the fraction of pulses that caused a click on the SNSPD.

Histograms of the amplified and de-amplified coherent state photocurrents can be seen in Figures 3.2(c), respectively. We classified any pulse with a phase $\theta \leq 0.15$ rad as amplified and any pulse with $|\pi/2 - \theta| \leq 0.15$ rad as de-amplified, as we found this to be a reasonable bin size through variation of the total number of bins. The amplified pulses have a higher average photocurrent and variance than amplified vacuum, and the de-amplified pulses have a similar distribution to amplified vacuum, as expected. The cause of the double-bumped distribution of $|\alpha| = 7.11$ in Figure 3.2(c) is likely pump

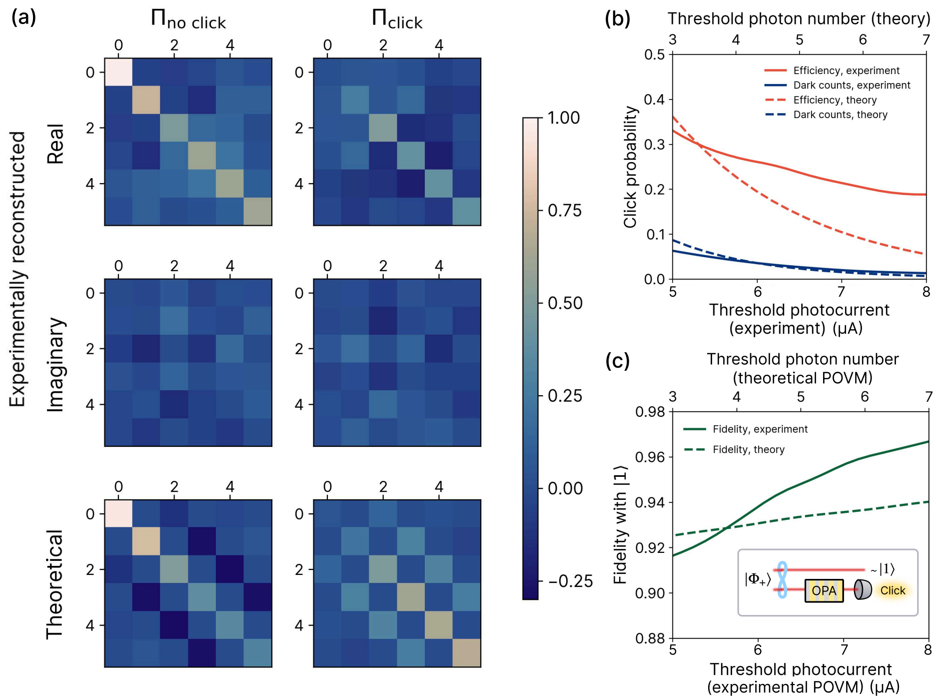

Figure 3.4: Detector tomography results and analysis. (a) The POVM elements of the OPAD, reconstructed through detector tomography (first and second rows) and theoretically calculated using QuTiP (third row). The theoretical POVM elements are real. (b) The efficiency and dark count rate of the detector for both experimentally reconstructed and theoretically calculated POVMs as a function of the threshold photocurrent or photon number. (c) The fidelity with a single-photon state after one mode of the Bell state $(|00\rangle + |11\rangle)/\sqrt{2}$ is measured with an OPAD vs. the threshold photocurrent or photon number, for both experimental and theoretical POVMs. Inset: diagram of the measurement scheme.

depletion, which leads to gain saturation and a bunching of the distributions at higher coherent state amplitudes. The average photocurrent as a function of the coherent state angle θ, with the data binned into 5 angle bins between 0 and $\pi/2$, is plotted in Figure 3.2(b). As θ approaches $\pi/2$, the average approaches that of a squeezed vacuum state, corresponding to the de-amplification of the coherent states.

Quantum detector tomography

We calculated the theoretical click and no-click POVM matrices for a squeezer with 10 dB of squeezing. We used $\eta = \eta_{pd}\eta_f = 0.314$, for photodetector efficiency $\eta_{pd} = 0.629$ and filter loss $\eta_f = 0.5$. In order to determine the appropriate standard deviation σ for

10 dB of squeezing we used the ratio of the standard deviation of the electronic noise to the average photocurrent for squeezed vacuum as a metric for the amount of noise. This metric was 0.172 for our setup and the average photon number for a 10 dB squeezed vacuum contains 2.02 photons, so for the theoretical POVM we used $\sigma = 2.02 \times 0.172 = 0.347$ photons. We summed over photon numbers up to 150 since at 10 dB the average photon number of squeezed vacuum is 2.02 and the probability amplitude at 150 photons is 10^{-7}.

To experimentally reconstruct the POVM of our OPAD, we used the convex optimization process described in [14], but with the full POVM matrices rather than just the diagonal entries, since this is a phase-sensitive measurement. Because of this, we must solve a tensor equation rather than just a matrix one. We seek to invert the following equation:

$$P_{i,n} = F_{i,k,p}\Pi_{k,p,n}, \tag{3.8}$$

where $P_{i,n} = \langle\alpha_i|\,\pi_n\,|\alpha_i\rangle$ is the experimentally determined probability of getting a click or not, with $|\alpha_i\rangle$ being a coherent state with amplitude α_i, and $F_{i,k,p} = \exp(-|\alpha_i|^2)(\alpha_i^*)^k\alpha_i^p/\sqrt{k!p!}$ are the prefactors associated with the type of state being sent in. $\Pi_{k,p,n} = \sum_{k,p}\theta^{(n)}\,|k\rangle\,\langle p|$ are the POVM matrices we are trying to find by performing a convex optimization which minimizes $||P - F\Pi||_2$. The indices k and p are the indices of the matrices, n refers to which measurement result ($n = 0$ for no click, $n = 1$ for a click), and i indexes the coherent state amplitude.

The optimization also involves a regularization constraint which smooths the diagonal entries of the POVM, which takes the form of

$$R = \sum_{k,n}(\theta^{(n)}_{k+1,k+1} - \theta^{(n)}_{k,k})^2. \tag{3.9}$$

We can then perform the minimization over

$$\min(||P - F\Pi||_2 + \gamma R), \tag{3.10}$$

for some regularization constant γ. Here we used $\gamma = 10^{-4}$, a relatively low value, in order to prevent over-smoothing of the POVM, as we expect some sharp characteristics from $|0\rangle\,\langle 0|$ to $|1\rangle\,\langle 1|$ indicating the click-like character of the detector. To ensure we use a value of γ not too high such that it starts to introduce artifacts, we swept γ and found the dark count rate and efficiency as a function of γ. We saw that 10^{-4} was within the region such that changing it did not change the result significantly, so we chose that value.

We used data from coherent states with amplitudes $|\alpha| = 0.449$, 4.87, and 7.11 and binned the phases into five bins between 0 and $\pi/2$, as shown in Fig. 3.2(c), in order to discretize the data enough for the convex optimization. We found that varying the bin sizes did not create large variations in the output, so we concluded that five bins was enough. We used CVXPY, a Python library for solving convex optimization problems, to invert Eqn. 3.8 [11].

The experimentally retrieved and theoretical POVMs are shown in Figure 3.4(a). The experimentally reconstructed POVM has a dark count probability of 2.2% and an efficiency of 26.2%, while the theoretical POVM has a dark count probability of 4.4% and an efficiency of 22.7%.

The theoretical POVM was calculated for an OPA with a scaled down amount of gain (10 dB) in order to be computationally viable, and with proportional noise. Since more squeezing does not change the POVM qualitatively, it is possible to recover the same POVMs from different amounts of gain by choosing appropriate thresholds. We calculated the fidelity between the theoretical and experimental POVMs $F_n = \mathrm{Tr}((\Pi_{n,\mathrm{theo}}^{1/2}\Pi_{n,\mathrm{exp}}\Pi_{n,\mathrm{theo}}^{1/2})^{1/2})^2$ [14], with the trace of each of the POVM elements normalized to 1, for every combination of N_{th} in the theoretical POVM and photocurrent threshold in the experimental reconstruction. The average fidelity of both elements, $(F_{\mathrm{click}} + F_{\mathrm{no\ click}})/2$, was over 0.72 for certain thresholds.

To quantify the trade-off between efficiency and dark counts, we swept the cutoff photocurrent in our convex optimization algorithm and swept N_{th} in the theoretical POVM calculation. The efficiencies and dark counts vs. the threshold photon number (for theory) and threshold photocurrent (for experiment) both for the experimental and theoretical POVMs are plotted in Figure 3.4(b), with the threshold photocurrent adjusted to match the threshold photon number proportionally to the gains of the OPAs. The experimental POVM outperforming the theoretical POVM at higher thresholds is an indication that the pump depletion, which causes the bump in the amplified photocurrent distribution, is improving the performance. This is because as the threshold photocurrent increases, especially above 6 μA, the detection probability does not decrease as quickly as for a squeezed coherent state with no pump depletion.

We considered an example of DV detection in which one mode of a Bell state $|\Phi_+\rangle = (|00\rangle + |11\rangle)/\sqrt{2}$ is sent to the OPAD. We calculated the fidelity of the other mode with a single photon ($|1\rangle$) as a function of the detection efficiency using the theoretical and

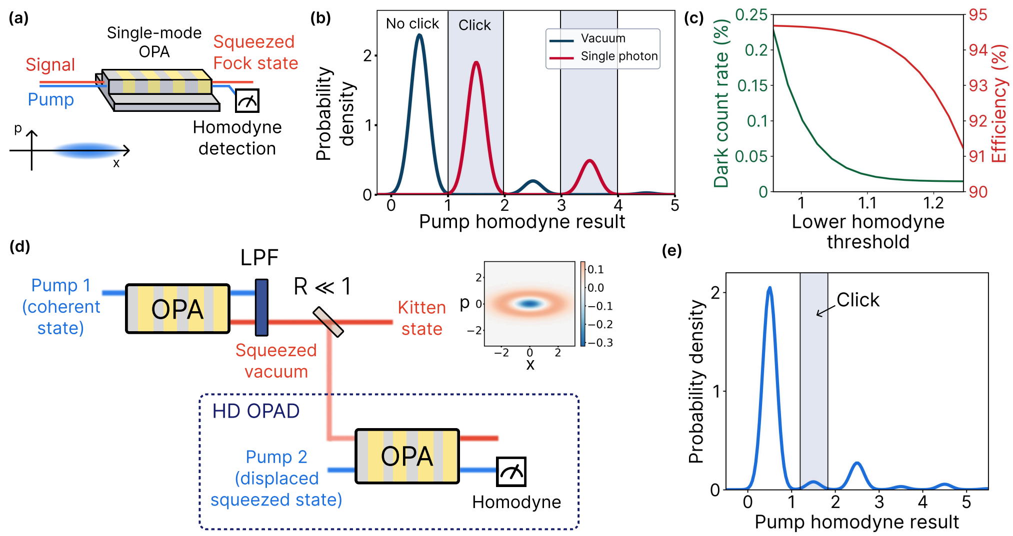

Figure 3.5: Simulation of using a homodyne detector OPAD to create a kitten state. (a) Diagram of the HD OPAD. The displaced squeezed pump's Wigner function is shown in the bottom left. (b) Simulated pump homodyne result distribution of vacuum (dark blue) and a single photon (red) as a function of the homodyne measurement result of the pump's squeezed quadrature. (c) Dark count rate (green) and efficiency (red) of the HD OPAD as a function of the lower homodyne measurement result threshold. (d) Diagram of the kitten state generation scheme. The first OPA creates squeezed vacuum and the second OPA is followed by a homodyne measurement on the depleted pump, triggering a click. The Wigner function of the kitten state is shown in the upper right. (e) The detection probability as a function of the pump homodyne measurement result, with the detection window for creating the kitten state shaded.

experimentally reconstructed POVMS. The numerical results are plotted in Figure 3.4(c). We find that for a detection efficiency of 30%, the fidelity of the other mode with a single photon is over 92%. As expected, the theoretical curve indicates a decrease in fidelity as the detection efficiency increases. This is due to the higher dark count probability. The calculations based on the experimental POVM have a higher fidelity than the theoretical fidelity, which can be explained by the pump depletion. Thus, in a system in which photons have already been generated, the PD OPAD can occupy a niche as an integrated detector that can project entangled states onto single photons.

3.4 Discussion of photodetector OPAD

It is worth noting that the measured dark count and quantum efficiency of the PD OPAD falls short of the established single-photon detectors. However, the OPAD as experimentally realized offers some benefits over conventional SPDs, such as its throughput speed, inherent integrability, and flexibility in wavelength. The fundamental limit of jitter for a typical SNSPD has been estimated to be on the order of 1 ps [13], with less than 3 ps having been demonstrated [23], while for a SPAD the smallest timing jitter demonstrated is in the tens of ps [6]. Unlike electronic SPDs, the OPAD does not rely on avalanche or superconducting switching dynamics, and its temporal resolution is instead linked to the OPA's bandwidth, the photodetection system, and the timing stability of the pump laser. Because the timing jitter is very low for mode-locked lasers and our OPA's bandwidth is on the order of THz [26], we consider the bandwidth of the photodetector to be an accurate measure of the time resolution of the system. The throughput speed of detection is limited by the laser repetition rate. We tested our detector at a click rate of 250 MHz, which is equal to the repetition rate of the pump laser due to the large amplitude of the coherent states we used ($|\alpha| = 7.11$). Higher repetition rates and timing resolution would be accessible with faster photodetection and laser systems. For example, photodetectors have currently achieved 3-dB bandwidths of 265 GHz [28]. With sufficient signal-to-noise ratio, the location of the peak of a pulse can be estimated with sub-cycle precision relative to the pump reference.

It is important to note that because our implementation of the OPAD is time-gated, the photon would have to arrive concurrently with the pump pulse, which in the case of this setup is 75 fs. This type of operation is well-suited for time-multiplexed computing [2, 24] and pulsed sensing [5] and reduces dark counts by not amplifying anything, including vacuum, outside of the pump pulse time window.

Typically, the efficiency of SNSPDs and SPADs decreases as the wavelength increases due to bandgap-related limitations [10], although SNSPDs exist which can detect photons at wavelengths up to 29 μm [44]. It is also possible to use sum-frequency generation to upconvert the photons to a detectable range [47]; however, this method introduces more loss and possibilities for errors. The current version of the PD OPAD can be designed to operate flexibly within the transparency window of LN spanning from the visible (400 nm) to the mid-IR (5 μm). This window can be extended by using other materials exhibiting second-order nonlinearity which are transparent at higher wavelengths, such as gallium arsenide, which is transparent up to 16 μm. Furthermore, the simplicity of the design and availability of integrated photodetectors on TFLN with bandwidths up to 140 GHz [50] and pump-suppression filtering through dichroic beamsplitters [39] means that this detector can be readily integrated into the fast-evolving nonlinear nanophotonic circuits in LN [55]. Additionally, our OPAD scheme is tolerant to losses after the OPA, as the loss affects all amplified states equally and can thus be accounted for by setting a lower threshold photocurrent. The PD OPAD would be well suited for applications emphasizing high repetition rate and post-selected measurements, such as on-chip calibration and characterization of photonic circuits or proof-of-principle experiments.

3.5 Homodyne detector OPAD

As an example of a path to future non-Gaussian operation, we show how using a homodyne on the pump after the OPA, akin to the QND scheme from [51], as shown in Fig. 3.5(a), can enhance the OPAD's performance over the currently feasible PD OPAD. For the HD OPAD, the click criteria is a range or multiple ranges of values of the pump homodyne measurement. This detector operates in the high g/κ (the ratio of the coupling between the fundamental and second harmonic to the single-photon loss) pump-depletion regime, in which the pump and signal become entangled, and non-Gaussian and Wigner negative features begin to emerge. In this regime, it is possible to project the signal state onto a squeezed Fock state through homodyne conditioning on the depleted pump, which is initially a displaced squeezed state.

We numerically simulated an HD OPAD by calculating its POVM using equation 10 from [51], with normalized interaction time $gt = 1$, initial pump squeezing of 5 dB, and single-mode OPA squeezing of 3.88 dB, and found that the measured distributions of vacuum and single photon inputs overlap very little, as can be seen in Fig. 3.5(b), unlike in the PD OPAD. This type of detector would have an efficiency of 94.7% and a dark count rate of 0.1% for the click categorization limits on the homodyne measurement corresponding to the shaded regions in the figure. The purity of the state resulting from a click is 0.94. The performance can be adjusted by changing these thresholds, as can be seen in Fig. 3.5(c). The interaction time t is not time in seconds, as g is normalized differently for a traveling-wave OPA rather than in a cavity. For example, for current OPA gain levels, the interaction time would be on the order of picoseconds to femtoseconds, allowing for low latency. The throughput rate is not limited by the interaction time, because multiple pulses can be amplified by an OPA at the same time. Rather, the throughput rate is limited by the pump pulse width, which determines how closely the pulses can be packed next to each other.

The proposed HD OPAD has a performance that is sufficient for efficient photon subtraction for generation of non-Gaussian states, provided further improvements in the gain and material loss on nanophotonic platforms. We consider creating a Schrödinger kitten state through photon subtraction from a 5-dB squeezed state [38] using an HD OPAD, as shown in Fig. 3.5(d). In this scheme, when the pump homodyne measurement is in a specific range (the shaded region of Fig. 3.5(e)), a click is triggered, projecting the initial squeezed vacuum onto a kitten state. The ensemble average output state purity is numerically estimated to be > 0.999, and the fidelity between the squeezed photon subtracted two-mode squeezed state and a photon subtracted squeezed state is 0.96, with a click probability of 3.1%. An increase in the squeezing of the input state leads to an increase in the click probability, with a 10-dB squeezed state having a 7.5% chance of a click. Because the HD-OPAD projects the state onto a squeezed Fock state subspace with the photon number determined by the homodyne result, a click still leads to a squeezed single-photon subtraction for the right thresholds.

Extracting g/κ from OPG measurements

We calculate both theoretically and from the OPG measurements how far away our system's g/κ is from the required amount. The interaction Hamiltonian for 3-wave mixing is

$$\frac{\hat{H}}{\hbar} = g(\hat{a}^{\dagger 2}\hat{b} + \hat{a}^2\hat{b}^\dagger) \tag{3.11}$$

for interaction strength g, signal annihilation operator $\hat{a}$, and pump annihilation operator $\hat{b}$. In the Heisenberg picture under the undepleted-pump assumption with pump strength $\hat{b} \to \beta$, for an initial state of vacuum, the signal number operator evolves as $\langle \hat{a}^\dagger \hat{a}\rangle(t) = \langle \hat{N}_a\rangle(t) = \sinh^2(2g|\beta|t)$. To compare this to the OPG equation (Eqn. 3.6), we consider how to convert these quantities into the power measurements. $\langle \hat{N}_a\rangle(t) = P_{OPG,on}/(\hbar\omega_s f_{rep})$ and $|\beta| = \sqrt{\langle \hat{N}_b\rangle} = \sqrt{P_{pump,on}/(\hbar\omega_p f_{rep})}$ where the "on" subscript refers to the on-chip power. Substituting, we have

$$P_{\text{OPG, off}} \approx \frac{\hbar\omega_s f_{\text{rep}}\eta_{OC}}{4} e^{4gt\sqrt{\eta_{IC}P_{\text{pump, off}}/(\hbar\omega_p f_{\text{rep}})}} \tag{3.12}$$

Comparing to Eqn. 3.6, we can see $4gt\sqrt{\eta_{IC}P_{\text{pump, off}}/(\hbar\omega_p f_{\text{rep}})} = 2L\sqrt{\eta_{NL}\eta_{IC}P_{\text{pump, off}}}$, so we have $g = L\sqrt{\eta_{NL}\hbar\omega_p f_{\text{rep}}}/(2t)$, and with $t = Ln/c$, finally,

$$g = \frac{c}{2n}\sqrt{\eta_{NL}\hbar\omega_p f_{\text{rep}}}. \tag{3.13}$$

From the value of η_{NL} from the fit, we have $g = 29$ MHz.

However, we must account for multimode effects in our OPA. The simplest, most naive way of dealing with it is to assume that each mode receives an equal amount of the gain. We calculate the spectral purity p_s from the normalized joint spectral intensity by performing a singular value decomposition and adding the squares of the eigenvalues, and obtain the effective mode number $m_{\text{eff}} = 1/p_s \approx 12.6$. We can then calculate $g_{\text{eff}} = g/m_{\text{eff}} = 2.3$ MHz.

We compare this number to the theoretical value using this equation from [52], modified to include the naive multimode effects:

$$g_{\text{eff}} = \frac{4d_{\text{eff}}}{m_{\text{eff}}\lambda^3}\sqrt{\frac{2\pi^3\hbar c^3}{n^3\varepsilon_0\tilde{V}_{sh}}} \tag{3.14}$$

where d_{eff} is the effective quadratic nonlinear coefficient, which is $d_{33}/(2\pi)$, with $d_{33} = 20$ pm/V and $\tilde{V}_{sh}$ is the effective mode volume divided by $(\lambda/n)^3$, with perfect mode overlap resulting in it being exactly the normalized mode volume. We use the size of the waveguide 400 nm by 1780 nm times the pulse width of $\tau_p = 100$ fs equating to $\tau_p c/n = 16.2$ µm for $n = 1.85$. Assuming perfect overlap and plugging in the parameters for our waveguide and pulse width to get the volume, we get an estimate of $g = 2.8$ MHz. This value is very close to the experimentally extracted value.

We estimate the loss in the waveguide of 0.23 dB/cm and a group velocity of $v_g = 1.33 \times 10^8$ m/s, which leads to a $\kappa = \alpha v_g$ [52] of 702 MHz. Thus, $g_{\text{eff}}/\kappa \approx 0.0033$.

Experimental realization of an HD OPAD requires further mitigation of the loss in nanophotonic waveguides and control of the multimode effects that occur with broadband pulsed operation and dispersion engineering or other methods to achieve single-mode operation [18, 52]. The g/κ needed to realize this detector is inversely proportional to the pump squeezing, which in the case of our simulation, with 5 dB of pump squeezing, corresponds to a requirement of $g/\kappa \gtrsim 0.16$ [51], representing a required improvement of about two orders of magnitude from our system. There are advancements continually being made to increase g/κ, with the record for g/κ in TFLN being 0.007 [31]. The performance of the HD-OPAD partially depends on wavelength; as long as g/κ is above that threshold, the performance is similar no matter the individual values of g or κ, but g decreases with wavelength so the loss will have to be appropriately lower in order for the ratio to remain above the threshold. Furthermore, the speed of homodyne detection is constantly being improved, with homodyne detection at 66 GHz having been experimentally demonstrated [20], and photodetectors are amenable to time multiplexing [49], further increasing the potential throughput and allowing for ultrafast operation.

3.6 Conclusion

We have demonstrated and characterized a PD OPAD on a TFLN nanophotonic chip. Our detector operates at room temperature and atmospheric pressure and is readily integrated into nanophotonic circuits. Through tailoring of the material, periodic poling, and dispersion engineering, it is possible to detect photons from visible wavelengths into the mid-IR. As an example of the OPAD's utility for DV QIP, we simulated a measurement using our experimental POVM on one mode of a Bell state, showing how this system is useful for DV state manipulations. We also showed a future path towards generating non-Gaussianity, showing numerically that it is possible to create a Schrödinger kitten state with an HD OPAD. Our results suggest that all-optical single-photon detection using second-order optical nonlinearity is a promising direction for integrated photonic quantum systems.

References

[1] J. M. Arrazola, V. Bergholm, K. Brádler, T. R. Bromley, M. J. Collins, I. Dhand, A. Fumagalli, T. Gerrits, A. Goussev, L. G. Helt, J. Hundal, T. Isacsson, R. B. Israel, J. Izaac, S. Jahangiri, R. Janik, N. Killoran, S. P. Kumar, J. Lavoie, A. E. Lita, D. H. Mahler, M. Menotti, B. Morrison, S. W. Nam, L. Neuhaus, H. Y. Qi, N. Quesada, A. Repingon, K. K. Sabapathy, M. Schuld, D. Su, J. Swinarton, A. Száva, K. Tan, P. Tan, V. D. Vaidya, Z. Vernon, Z. Zabaneh, and Y. Zhang. "Quantum circuits with many photons on a programmable nanophotonic chip". In: *Nature* 591.7848 (Mar. 2021), pp. 54–60. DOI: `10.1038/s41586-021-03202-1`.

[2] Warit Asavanant, Yu Shiozawa, Shota Yokoyama, Baramee Charoensombutamon, Hiroki Emura, Rafael N. Alexander, Shuntaro Takeda, Jun-ichi Yoshikawa, Nicolas C. Menicucci, Hidehiro Yonezawa, and Akira Furusawa. "Generation of time-domain-multiplexed two-dimensional cluster state". In: *Science* 366.6463 (Oct. 18, 2019), pp. 373–376. DOI: `10.1126/science.aay2645`.

[3] Ben Q. Baragiola, Giacomo Pantaleoni, Rafael N. Alexander, Angela Karanjai, and Nicolas C. Menicucci. "All-Gaussian Universality and Fault Tolerance with the Gottesman-Kitaev-Preskill Code". In: *Physical Review Letters* 123.20 (Nov. 13, 2019), p. 200502. DOI: `10.1103/PhysRevLett.123.200502`.

[4] Sara Bartolucci, Patrick Birchall, Hector Bombin, Hugo Cable, Chris Dawson, Mercedes Gimeno-Segovia, Eric Johnston, Konrad Kieling, Naomi Nickerson, Mihir Pant, et al. "Fusion-based quantum computation". In: *Nature Communications* 14.1 (2023), p. 912.

[5] Catxere A Casacio, Lars S Madsen, Alex Terrasson, Muhammad Waleed, Kai Barnscheidt, Boris Hage, Michael A Taylor, and Warwick P Bowen. "Quantum-enhanced nonlinear microscopy". In: *Nature* 594.7862 (2021), pp. 201–206.

[6] Francesco Ceccarelli, Giulia Acconcia, Angelo Gulinatti, Massimo Ghioni, Ivan Rech, and Roberto Osellame. “Recent Advances and Future Perspectives of Single-Photon Avalanche Diodes for Quantum Photonics Applications”. In: *Advanced Quantum Technologies* 4.2 (2021). _eprint: https://onlinelibrary.wiley.com/doi/pdf/10.1002/qute.20 p. 2000102. DOI: 10.1002/qute.202000102.

[7] J. Chang, J. W. N. Los, J. O. Tenorio-Pearl, N. Noordzij, R. Gourgues, A. Guardiani, J. R. Zichi, S. F. Pereira, H. P. Urbach, V. Zwiller, S. N. Dorenbos, and I. Esmaeil Zadeh. “Detecting telecom single photons with 99.52.07+0.5% system detection efficiency and high time resolution”. In: *APL Photonics* 6.3 (Mar. 30, 2021), p. 036114. DOI: 10.1063/5.0039772.

[8] Jeff Chiles, Ilya Charaev, Robert Lasenby, Masha Baryakhtar, Junwu Huang, Alexana Roshko, George Burton, Marco Colangelo, Ken Van Tilburg, Asimina Arvanitaki, Sae Woo Nam, and Karl K. Berggren. “New Constraints on Dark Photon Dark Matter with Superconducting Nanowire Detectors in an Optical Haloscope”. In: *Physical Review Letters* 128.23 (June 10, 2022), p. 231802. DOI: 10.1103/PhysRevLett.128.231802.

[9] Alex O C Davis, Mattia Walschaers, Valentina Parigi, and Nicolas Treps. “Conditional preparation of non-Gaussian quantum optical states by mesoscopic measurement”. In: *New Journal of Physics* 23.6 (June 1, 2021), p. 063039. DOI: 10.1088/1367-2630/ac0204.

[10] Stefano Dello Russo, Arianna Elefante, Daniele Dequal, Deborah Katia Pallotti, Luigi Santamaria Amato, Fabrizio Sgobba, and Mario Siciliani de Cumis. “Advances in Mid-Infrared Single-Photon Detection”. In: *Photonics* 9.7 (July 2022). Number: 7, p. 470. DOI: 10.3390/photonics9070470.

[11] Steven Diamond and Stephen Boyd. “CVXPY: A Python-Embedded Modeling Language for Convex Optimization”. In: *Journal of Machine Learning Research* (2016). To appear.

[12] Miller Eaton, Amr Hossameldin, Richard J. Birrittella, Paul M. Alsing, Christopher C. Gerry, Hai Dong, Chris Cuevas, and Olivier Pfister. “Resolution of 100 photons and quantum generation of unbiased random numbers”. In: *Nature Photonics* 17.1 (Jan. 2023), pp. 106–111. DOI: 10.1038/s41566-022-01105-9.

[13] Iman Esmaeil Zadeh, J. Chang, Johannes W. N. Los, Samuel Gyger, Ali W. Elshaari, Stephan Steinhauer, Sander N. Dorenbos, and Val Zwiller. “Superconducting nanowire single-photon detectors: A perspective on evolution, state-of-the-art, future developments, and applications”. In: *Applied Physics Letters* 118.19 (May 10, 2021), p. 190502. DOI: 10.1063/5.0045990.

[14] A Feito, J S Lundeen, H Coldenstrodt-Ronge, J Eisert, M B Plenio, and I A Walmsley. “Measuring measurement: theory and practice”. In: *New Journal of Physics* 11.9 (Sept. 28, 2009), p. 093038. DOI: 10.1088/1367-2630/11/9/093038.

[15] Daniel Gottesman, Alexei Kitaev, and John Preskill. "Encoding a qubit in an oscillator". In: *Physical Review A* 64.1 (2001), p. 012310.

[16] Warren Grice and Ian A. Walmsley. "Homodyne detection in a photon counting application". In: *Journal of Modern Optics* 43.4 (Apr. 1, 1996), pp. 795–805. DOI: 10.1080/09500349608232783.

[17] De-Yong He, Shuang Wang, Jia-Lin Chen, Wei Chen, Zhen-Qiang Yin, Guan-Jie Fan-Yuan, Zheng Zhou, Guang-Can Guo, and Zheng-Fu Han. "2.5 GHz Gated InGaAs/InP Single-Photon Avalanche Diode with 44 ps Time Jitter". In: *Advanced Devices & Instrumentation* 4 (Sept. 13, 2023), p. 0020. DOI: 10.34133/adi.0020.

[18] Martin Houde and Nicolás Quesada. "Waveguided sources of consistent, single-temporal-mode squeezed light: The good, the bad, and the ugly". In: *AVS Quantum Science* 5.1 (2023).

[19] Mahmoud Kalash and Maria V. Chekhova. "Wigner function tomography via optical parametric amplification". In: *Optica* 10.9 (Sept. 20, 2023), p. 1142. DOI: 10.1364/OPTICA.488697.

[20] Akito Kawasaki, Ryuhoh Ide, Hector Brunel, Takumi Suzuki, Rajveer Nehra, Katsuki Nakashima, Takahiro Kashiwazaki, Asuka Inoue, Takeshi Umeki, Fumihiro China, Masahiro Yabuno, Shigehito Miki, Hirotaka Terai, Taichi Yamashima, Atsushi Sakaguchi, Kan Takase, Mamoru Endo, Warit Asavanant, and Akira Furusawa. "Broadband generation and tomography of non-Gaussian states for ultrafast optical quantum processors". In: *Nature Communications* 15.1 (Nov. 1, 2024), p. 9075. DOI: 10.1038/s41467-024-53408-w.

[21] Emanuel Knill, Raymond Laflamme, and Gerald J Milburn. "A scheme for efficient quantum computation with linear optics". In: *nature* 409.6816 (2001), pp. 46–52.

[22] Shunya Konno, Warit Asavanant, Fumiya Hanamura, Hironari Nagayoshi, Kosuke Fukui, Atsushi Sakaguchi, Ryuhoh Ide, Fumihiro China, Masahiro Yabuno, Shigehito Miki, et al. "Logical states for fault-tolerant quantum computation with propagating light". In: *Science* 383.6680 (2024), pp. 289–293.

[23] Boris Korzh, Qing-Yuan Zhao, Jason P. Allmaras, Simone Frasca, Travis M. Autry, Eric A. Bersin, Andrew D. Beyer, Ryan M. Briggs, Bruce Bumble, Marco Colangelo, Garrison M. Crouch, Andrew E. Dane, Thomas Gerrits, Adriana E. Lita, Francesco Marsili, Galan Moody, Cristián Peña, Edward Ramirez, Jake D. Rezac, Neil Sinclair, Martin J. Stevens, Angel E. Velasco, Varun B. Verma, Emma E. Wollman, Si Xie, Di Zhu, Paul D. Hale, Maria Spiropulu, Kevin L. Silverman, Richard P. Mirin, Sae Woo Nam, Alexander G. Kozorezov, Matthew D. Shaw, and Karl K. Berggren. "Demonstration of sub-3 ps temporal resolution with a superconducting nanowire single-photon detector". In: *Nature Photonics* 14.4 (Apr. 2020), pp. 250–255. DOI: 10.1038/s41566-020-0589-x.

[24] Mikkel V Larsen, Xueshi Guo, Casper R Breum, Jonas S Neergaard-Nielsen, and Ulrik L Andersen. "Deterministic generation of a two-dimensional cluster state". In: *Science* 366.6463 (2019), pp. 369–372.

[25] Jascha A Lau, Varun B Verma, Dirk Schwarzer, and Alec M Wodtke. "Superconducting single-photon detectors in the mid-infrared for physical chemistry and spectroscopy". In: *Chemical Society Reviews* 52.3 (2023), pp. 921–941.

[26] Luis Ledezma, Ryoto Sekine, Qiushi Guo, Rajveer Nehra, Saman Jahani, and Alireza Marandi. "Intense optical parametric amplification in dispersion-engineered nanophotonic lithium niobate waveguides". In: *Optica* 9.3 (Mar. 20, 2022), p. 303. DOI: 10.1364/OPTICA.442332.

[27] Jintian Lin, Fang Bo, Ya Cheng, and Jingjun Xu. "Advances in on-chip photonic devices based on lithium niobate on insulator". In: *Photonics Research* 8.12 (Dec. 1, 2020), pp. 1910–1936. DOI: 10.1364/PRJ.395305.

[28] S Lischke, A Peczek, JS Morgan, K Sun, D Steckler, Y Yamamoto, F Korndörfer, C Mai, S Marschmeyer, M Fraschke, et al. "Ultra-fast germanium photodiode with 3-dB bandwidth of 265 GHz". In: *Nature Photonics* 15.12 (2021), pp. 925–931.

[29] Adriana E Lita, Aaron J Miller, and Sae Woo Nam. "Counting near-infrared single-photons with 95% efficiency". In: *Optics express* 16.5 (2008), pp. 3032–3040.

[30] Seth Lloyd and Samuel L Braunstein. "Quantum computation over continuous variables". In: *Physical Review Letters* 82.8 (1999), p. 1784.

[31] Juanjuan Lu, Ming Li, Chang-Ling Zou, Ayed Al Sayem, and Hong X. Tang. "Toward 1% single-photon anharmonicity with periodically poled lithium niobate microring resonators". In: *Optica* 7.12 (Dec. 20, 2020), p. 1654. DOI: 10.1364/OPTICA.403931.

[32] J. S. Lundeen, A. Feito, H. Coldenstrodt-Ronge, K. L. Pregnell, Ch. Silberhorn, T. C. Ralph, J. Eisert, M. B. Plenio, and I. A. Walmsley. "Tomography of quantum detectors". In: *Nature Physics* 5.1 (Jan. 2009), pp. 27–30. DOI: 10.1038/nphys1133.

[33] Nicolas C. Menicucci. "Temporal-mode continuous-variable cluster states using linear optics". In: *Physical Review A* 83.6 (June 13, 2011), p. 062314. DOI: 10.1103/PhysRevA.83.062314.

[34] Galan Moody, Volker J Sorger, Daniel J Blumenthal, Paul W Juodawlkis, William Loh, Cheryl Sorace-Agaskar, Alex E Jones, Krishna C Balram, Jonathan CF Matthews, Anthony Laing, et al. "2022 Roadmap on integrated quantum photonics". In: *Journal of Physics: Photonics* 4.1 (2022), p. 012501.

[35] Rajveer Nehra, Kevin Valson Jacob, Miller Eaton, and Olivier Pfister. "Characterizing Quantum Detectors by Wigner Functions". In: *OSA Quantum 2.0 Conference (2020), paper QTu8A.6*. Quantum 2.0. Optica Publishing Group, Sept. 14, 2020, QTu8A.6. DOI: 10.1364/QUANTUM.2020.QTu8A.6.

[36] Rajveer Nehra, Ryoto Sekine, Luis Ledezma, Qiushi Guo, Robert M. Gray, Arkadev Roy, and Alireza Marandi. “Few-cycle vacuum squeezing in nanophotonics”. In: *Science* 377.6612 (Sept. 16, 2022), pp. 1333–1337. DOI: 10.1126/science.abo6213.

[37] Jeremy L O’brien. “Optical quantum computing”. In: *Science* 318.5856 (2007), pp. 1567–1570.

[38] Alexei Ourjoumtsev, Rosa Tualle-Brouri, Julien Laurat, and Philippe Grangier. “Generating optical Schrodinger kittens for quantum information processing”. In: *Science* 312.5770 (2006), pp. 83–86.

[39] Taewon Park, Hubert Stokowski, Vahid Ansari, Samuel Gyger, Kevin KS Multani, Oguz Tolga Celik, Alexander Y Hwang, Devin J Dean, Felix Mayor, Timothy P McKenna, et al. “Single-mode squeezed-light generation and tomography with an integrated optical parametric oscillator”. In: *Science Advances* 10.11 (2024).

[40] Dileep V. Reddy, Robert R. Nerem, Sae Woo Nam, Richard P. Mirin, and Varun B. Verma. “Superconducting nanowire single-photon detectors with 98% system detection efficiency at 1550 nm”. In: *Optica* 7.12 (Dec. 20, 2020), p. 1649. DOI: 10.1364/OPTICA.400751.

[41] Giovanni V. Resta, Lorenzo Stasi, Matthieu Perrenoud, Sylvain El-Khoury, Tiff Brydges, Rob Thew, Hugo Zbinden, and Félix Bussières. “GHz detection rates and dynamic photon-number resolution with superconducting nanowire arrays”. In: *Nano Letters* 23.13 (July 12, 2023), pp. 6018–6026. DOI: 10.1021/acs.nanolett.3c01228. arXiv: 2303.17401[physics,physics:quant-ph].

[42] Ayed Al Sayem, Risheng Cheng, Sihao Wang, and Hong X. Tang. “Lithium-niobate-on-insulator waveguide-integrated superconducting nanowire single-photon detectors”. In: *Applied Physics Letters* 116.15 (Apr. 13, 2020), p. 151102. DOI: 10.1063/1.5142852.

[43] S. Y. Siew, B. Li, F. Gao, H. Y. Zheng, W. Zhang, P. Guo, S. W. Xie, A. Song, B. Dong, L. W. Luo, C. Li, X. Luo, and G.-Q. Lo. “Review of Silicon Photonics Technology and Platform Development”. In: *Journal of Lightwave Technology* 39.13 (July 2021). Conference Name: Journal of Lightwave Technology, pp. 4374–4389. DOI: 10.1109/JLT.2021.3066203.

[44] Gregor G. Taylor, Alexander B. Walter, Boris Korzh, Bruce Bumble, Sahil R. Patel, Jason P. Allmaras, Andrew D. Beyer, Roger O’Brient, Matthew D. Shaw, and Emma E. Wollman. “Low-noise single-photon counting superconducting nanowire detectors at infrared wavelengths up to 29 µm”. In: *Optica* 10.12 (Dec. 20, 2023), pp. 1672–1678. DOI: 10.1364/OPTICA.509337.

[45] Sjoerd Telkamp, Odiel Hooybergs, Myriam Rihani, Giovanni Finco, Tummas Napoleon Arge, Robin N Dür, Victor Mougel, Daniel Scheffler, Filip Krizek, Rachel Grange, et al. “High-temperature growth of ultra thin NbTiN films on lithium niobate for integrated single photon detection”. In: *arXiv preprint arXiv:2509.07870* (2025).

[46] Jianwei Wang, Fabio Sciarrino, Anthony Laing, and Mark G Thompson. “Integrated photonic quantum technologies”. In: *Nature Photonics* 14.5 (2020), pp. 273–284.

[47] Xina Wang, Xufeng Jiao, Bin Wang, Yang Liu, Xiu-Ping Xie, Ming-Yang Zheng, Qiang Zhang, and Jian-Wei Pan. “Quantum frequency conversion and single-photon detection with lithium niobate nanophotonic chips”. In: *npj Quantum Information* 9.1 (2023), p. 38.

[48] James Williams, Rajveer Nehra, Elina Sendonaris, Luis Ledezma, Robert M Gray, Ryoto Sekine, and Alireza Marandi. “Ultrashort pulse biphoton source in lithium niobate nanophotonics at 2 μm”. In: *Nanophotonics* 13.18 (2024), pp. 3535–3544.

[49] James Williams*, Elina Sendonaris*, Rajveer Nehra, Robert M. Gray, Ryoto Sekine, Luis Ledezma, and Alireza Marandi. “Ultrafast all-optical measurement of squeezed vacuum in a lithium niobate nanophotonic circuit”. In: *Physical Review Research* 7.4 (Oct. 1, 2025), p. 043006. DOI: 10.1103/rvmb-ljd3.

[50] Xiaojun Xie, Chao Wei, Xingchen He, Yake Chen, Chenghao Wang, Jihui Sun, Lin Jiang, Jia Ye, Xihua Zou, Wei Pan, et al. “A 3.584 Tbps coherent receiver chip on InP-LiNbO3 wafer-level integration platform”. In: *Light: Science & Applications* 14.1 (2025), p. 172.

[51] Ryotatsu Yanagimoto, Rajveer Nehra, Ryan Hamerly, Edwin Ng, Alireza Marandi, and Hideo Mabuchi. “Quantum Nondemolition Measurements with Optical Parametric Amplifiers for Ultrafast Universal Quantum Information Processing”. In: *PRX Quantum* 4.1 (Mar. 29, 2023), p. 010333. DOI: 10.1103/PRXQuantum.4.010333.

[52] Ryotatsu Yanagimoto, Edwin Ng, Marc Jankowski, Hideo Mabuchi, and Ryan Hamerly. “Temporal trapping: a route to strong coupling and deterministic optical quantum computation”. In: *Optica* 9.11 (2022), pp. 1289–1296.

[53] Ryotatsu Yanagimoto, Edwin Ng, Marc Jankowski, Rajveer Nehra, Timothy P. McKenna, Tatsuhiro Onodera, Logan G. Wright, Ryan Hamerly, Alireza Marandi, M. M. Fejer, and Hideo Mabuchi. *Mesoscopic ultrafast nonlinear optics – The emergence of multimode quantum non-Gaussian physics.* Nov. 22, 2023. arXiv: 2311.13775[physics,physics:quant-ph].

[54] Weijun Zhang, Jia Huang, Chengjun Zhang, Lixing You, Chaolin Lv, Lu Zhang, Hao Li, Zhen Wang, and Xiaoming Xie. “A 16-Pixel Interleaved Superconducting Nanowire Single-Photon Detector Array With A Maximum Count Rate Exceeding 1.5 GHz”. In: *IEEE Transactions on Applied Superconductivity* 29.5 (Aug. 2019). Conference Name: IEEE Transactions on Applied Superconductivity, pp. 1–4. DOI: 10.1109/TASC.2019.2895621.

[55] Di Zhu, Linbo Shao, Mengjie Yu, Rebecca Cheng, Boris Desiatov, C. J. Xin, Yaowen Hu, Jeffrey Holzgrafe, Soumya Ghosh, Amirhassan Shams-Ansari, Eric Puma, Neil Sinclair, Christian Reimer, Mian Zhang, and Marko Lončar. "Integrated photonics on thin-film lithium niobate". In: *Advances in Optics and Photonics* 13.2 (June 30, 2021), pp. 242–352. DOI: 10.1364/AOP.411024.

Chapter 4

ULTRAFAST ALL-OPTICAL MEASUREMENT OF SQUEEZED VACUUM IN A LITHIUM NIOBATE NANOPHOTONIC CIRCUIT

[1] James Williams*, Elina Sendonaris*, Rajveer Nehra, Robert M. Gray, Ryoto Sekine, Luis Ledezma, and Alireza Marandi. “Ultrafast all-optical measurement of squeezed vacuum in a lithium niobate nanophotonic circuit”. In: *Physical Review Research* 7.4 (Oct. 1, 2025), p. 043006. DOI: 10.1103/rvmb-ljd3.

ABSTRACT

Squeezed vacuum, a fundamental resource for continuous-variable quantum information processing, has been used to demonstrate quantum advantages in sensing, communication, and computation. While most experiments use homodyne detection to characterize squeezing and are therefore limited to electronic bandwidths, recent experiments have shown optical parametric amplification (OPA) to be a viable measurement strategy. Here, we realize OPA-based quantum state tomography in integrated photonics and demonstrate the generation and all-optical Wigner tomography of squeezed vacuum in a nanophotonic circuit. We employ dispersion engineering to enable the near-distortion-free propagation of femtosecond pulses and achieve ultra-broad operation bandwidths, effectively lifting the speed restrictions imposed by traditional electronics on quantum measurements with a theoretical maximum clock speed of 6.5 THz. We implement our circuit on thin-film lithium niobate, a platform compatible with a wide variety of active and passive photonic components. Our results chart a course for realizing all-optical ultrafast quantum information processing in an integrated room-temperature platform.

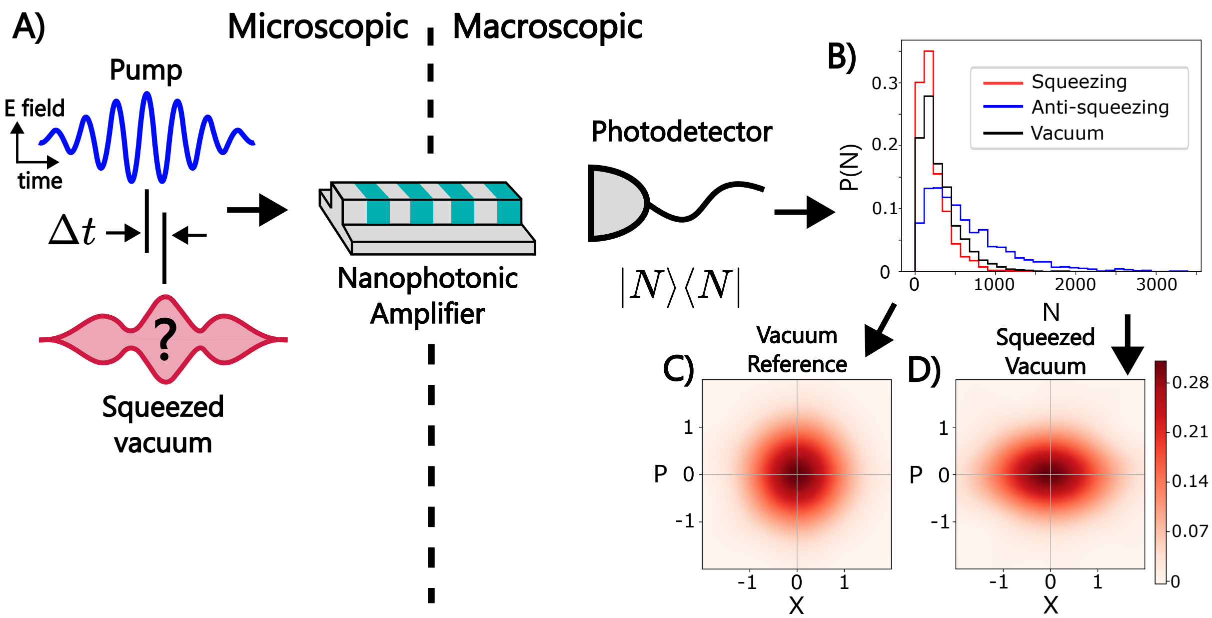

Figure 4.1: A) Layout of the measurement procedure. Δt represents the relative time-delay between the pump and squeezed vacuum where a 0.775 fs delay corresponds to a measurement phase of $\theta = \frac{\pi}{2}$. B) Measured photon number distributions for squeezing ($\theta = \frac{\pi}{2}$), anti-squeezing ($\theta = 0$) and vacuum. C) Wigner function recovered for vacuum. D) Wigner function recovered for squeezed vacuum.

4.1 Introduction

Many quantum systems have been used to gain an advantage over otherwise purely classical means in a variety of fields [10, 16, 42]. Implementations of provably-secure quantum key distribution and random-number generation are now commercially available [23, 25, 39]. Many enhanced sensing techniques using squeezed and non-classical states of light with applications in chemistry and imaging have been shown [1, 9, 20, 48]. Considerable effort is currently being invested into building quantum computers both in research and industry [2, 18, 49].

Photonics has emerged as a front-runner for quantum information processing for several key reasons. Most photonic technologies are capable of operating at room temperature outside a carefully controlled cryogenic environment. Advances in integrated photonics have allowed many devices and circuits to be combined into a single monolithic platform similar to CMOS technology and the advent of integrated circuits [59]. Photonics also offers an inherently broad bandwidth which, when combined with dispersion engineering, can allow for the manipulation and propagation of ultra-short pulses of light [34]. Time-multiplexing, an effective technique used in photonic systems to increase information throughput [28, 29, 35, 55], can leverage femtosecond pulses to achieve clock speeds far exceeding what is currently possible with conventional electronics.

Optical parametric amplifiers (OPAs) are a cornerstone of quantum optics and continuous-variable quantum information, and have been studied extensively in a variety of different contexts. In the low-gain limit, OPAs generate pairs of entangled photons for quantum-enhanced sensing and quantum key distribution [12, 30, 37, 47, 62]. Boson sampling with a quantum advantage has recently been demonstrated with 100 independent OPAs [66]. At higher gains, OPAs generate squeezed vacuum (SV), a quantum state in which one quadrature is compressed below the shot-noise limit. SV is often used for sensing enhancement [33] and most notably in the LIGO experiment [43]. Independently-generated SV states can be combined to create a highly entangled cluster state for universal quantum computation [4, 32]. SV generation from a type-0 source is typically spectrotemporally multimode. Recently, several experiments have demonstrated how these modes can be utilized as a basis for quantum information. Bulk experiments have shown that shaping the spectral profile of the pump can control the occupancy of each mode [52]. Pump shaping combined with engineering of the phase matching condition for sum-frequency generation can be used to isolate and measure each individual mode [3, 11].

A crucial part of any quantum information processing system is a measurement device capable of characterizing a component of interest. For SV, homodyne detection is often employed as its phase-sensitive nature can be used to reconstruct the Wigner function, a quasi-probability distribution over two non-commuting quadratures which completely characterizes a quantum state. Homodyne detectors can isolate a single mode by shaping the spectral profile of the pump appropriately [50]. This phase-sensitive and mode-selective behavior makes them well-suited for characterizing a variety of quantum states, including non-classical states. Single-photon and photon number-resolving (PNR) detectors are also common tools for state characterization, especially in the context of states exhibiting Wigner negativity [31, 46]. Given the non-Gaussian nature of their measurement operator, PNR detectors have been used to generate non-classical states which are characterized through homodyne detection [15, 56, 58, 65]. While homodyne and PNR detection are powerful techniques for probing quantum states of interest, their speed is ultimately constrained by the bandwidth of the electronics used to physically realize these detectors, which are limited to the GHz range.

OPAs have seen use as a method of measuring quantum information [53, 57]. Degenerate $\chi^{(2)}$ OPAs use a nonlinear medium to amplify a signal at ω using a pump at 2ω. Importantly, OPAs amplify the portion of the signal that is in-phase with the pump and de-amplify the out-of-phase portion. Similar to homodyne detection, this phase sensitivity allows for quantum information to be recovered from the input state by resolving the number of photons in the output state [27, 45].

Here, we demonstrate OPA-based Wigner tomography in lithium niobate nanophotonics. In our previous demonstration of nanophotonic OPA measurements [45], we measured the average photon number at the output of the OPA to calculate squeezing levels. In this work, we use a fast photodetector to measure each pulse and resolve the statistical information necessary to calculate the Wigner function of the input SV. Our OPA has low dispersion at both the pump and signal wavelengths, allowing for the near-distortion-free propagation and amplification of femtosecond pulses. Such an OPA-based circuit for generating and measuring SV supports a maximum clock speed of 6.5 THz for time-multiplexed quantum information processing. Our results highlight nanophotonic OPAs as an important building block for ultrafast quantum state measurement and information processing on a chip and at room temperature.

4.2 Parametric Amplifiers as Quantum Measurement Devices

Early proposals of OPAs as quantum measurement devices demonstrated loss tolerance and detector inefficiency mitigation [7]. OPAs are particularly well-suited for this task as their phase-sensitive amplification is in principle noiseless unlike phase-insensitive amplifiers such as erbium-doped fibers and semiconductor gain media [41]. OPA-assisted balanced homodyne detection has been used to characterized fiber-based sources of SV over 43 GHz of electronic bandwidth [26]. A similar technique has also been demonstrated using the $\chi^{(3)}$ nonlinearity [53]. Other experiments have shown quantum-enhanced sensing using an SU(1,1) interferometer constructed from two OPAs for state readout [14, 24]. OPAs have also been used to amplify weak spatially-varying signals and detect quantum correlations for imaging applications [40, 54]. All-optical feed-forward, a technique used to surpass the constraints of electronics in feed-forward schemes for quantum information processing, has been demonstrated using 3 OPAs [64]. Wigner-tomography of squeezed states using bulk OPAs has been experimentally realized [27]. OPA-based techniques have also been extended to squeezing across multiple spatial modes where direct detection is used to disentangle and analyze each mode independently [5].

Quadrature Measurement

Figure 4.1 depicts the scheme used to measure the Wigner function of a squeezed vacuum state. When a quantum signal enters the OPA, its in-phase quadrature $\hat{x}(\theta)$ is amplified by the pump while its out-of-phase quadrature $\hat{p}(\theta)$ is de-amplified. These quadratures map to the un-rotated quadratures of the state as:

$$\hat{x}(\theta) = \hat{x}\cos(\theta) - \hat{p}\sin(\theta) \tag{4.1}$$

$$\hat{p}(\theta) = \hat{p}\cos(\theta) + \hat{x}\sin(\theta) \tag{4.2}$$

Where θ represents a relative phase between the pump and amplified signal induced by adjusting the time-delay ($\Delta t \propto \theta$) of the pump. After amplification, the output quadratures can be expressed as:

$$\hat{X}(\theta) = e^{r}\hat{x}(\theta) \tag{4.3}$$

$$\hat{P}(\theta) = e^{-r}\hat{p}(\theta) \tag{4.4}$$

where e^r, the amplification applied by the OPA, can be controlled by changing the pump power. The operator for the number of photons in the signal field at the output is then:

$$\hat{N}_\theta = \hat{X}(\theta)^2 + \hat{P}(\theta)^2 - \frac{1}{2} \tag{4.5}$$

For a large gain $e^r \gg 1 \gg e^{-r}$, the 2nd and 3rd terms of Eq.4.5 can be ignored such that:

$$\hat{N}_\theta \approx \hat{X}(\theta)^2 \tag{4.6}$$

By resolving the number of photons at the output of the OPA in the signal field in each pulse, we can recover the marginal distribution $P(N, \theta)$, or the probability of detecting N photons at a pump phase θ.

Because our OPA exhibits low dispersion over a broad bandwidth while operating in the type-0 phase matching configuration, it amplifies many orthogonal spectrotemporal modes simultaneously [60], all of which contribute to the measured $P(N, \theta)$. These modes

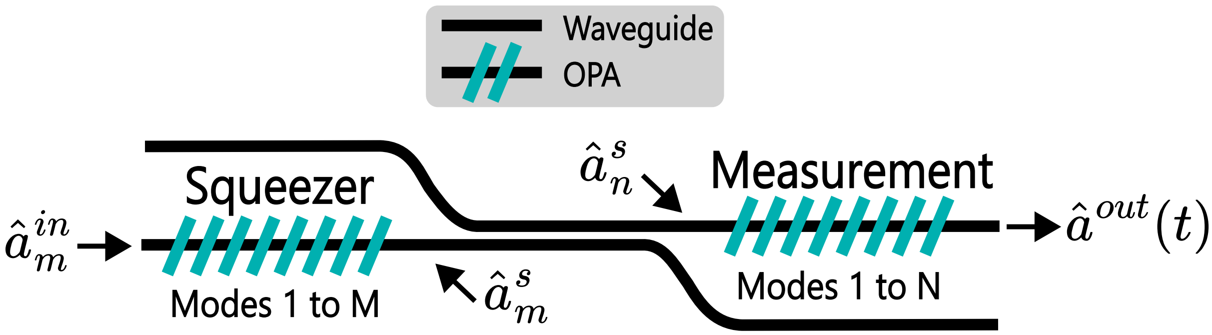

Figure 4.2: A diagram of the squeezer and measurement OPA circuit. The annihilation operators correspond to the modes at each point in the circuit, with m denoting the squeezer OPA basis and n denoting the measurement OPA basis.

can be calculated analytically by computing the joint spectral intensity (JSI) function of the signal and idler, which is the absolute value squared of the JSA ($JSI(\omega_s, \omega_i) = |J(\omega_s, \omega_i)|^2$). Our JSI and the corresponding modes are computed and plotted using the dispersion parameters calculated from the waveguide geometry and the Heisenberg propagators derived in [22]. As our JSI is inseparable ($|J(\omega_s, \omega_i)|^2 \neq \phi(\omega_s)\phi(\omega_i)$), it is composed of a sum over multiple terms $J_n(\omega_s, \omega_i)$, each corresponding to an independent mode through $J_n(\omega_s, \omega_i) = \phi_n(\omega_s)\phi_n(\omega_i)$, as shown in Fig. 4.3.

At the photodetector, we use a combination of a 1700-nm long-pass filter and 1950-nm short-pass filter to suppress contributions from higher order modes. Using the measured $P(N)$ for vacuum amplification (i.e when no signal field is sent into the OPA), we calculate a Schmidt number of 1.35 modes using definition of $g^{(2)}$ from [13].

Multimode Cascaded Squeezing in the Heisenberg picture

We use the formalism of [61] to derive the output of a two cascaded multimode OPAs: a squeezer OPA and a measurement OPA. Figure 4.2 shows the circuit diagram. We begin with the state after the squeezer OPA (denoted with superscript s) and decompose the annihilation operator into the squeezer OPA's eigenmodes (denoted by subscript m):

$$\begin{aligned}\hat{a}^s(t) &= \sum_m \psi_m^{s*}(t)\hat{a}_m^s \\ &= \sum_m \psi_m^{s*}(t)(\cosh r_m^s \hat{a}_m^{in} + \sinh r_m^s \hat{a}_m^{in\dagger})\end{aligned} \tag{4.7}$$

where r_m^s is the squeezing parameter of mode m. Each eigenmode of the squeezer OPA is independently squeezed. To simplify later expressions, we assume that $r_m^s = r_m^s(\theta)$

where θ is the phase of the squeezed vacuum relative to the measurement pump. In our experiment, we inject vacuum into the squeezer OPA, and so $\hat{a}^{in} \equiv \hat{a}^{vac}$.

After the squeezer OPA, the state is placed into the measurement OPA (superscript ms and mode subscript n) and the resulting output operator is labeled $\hat{a}^{out}(t)$. The measurement OPA amplifies its own modes as independent single-mode OPAs:

$$\begin{aligned}\hat{a}^{out}(t) &= \sum_n \psi_n^{ms*}(t)\hat{a}_n^{out} \\ &= \sum_n \psi_n^{ms*}(t)(\cosh r_n^{ms}\hat{a}_n^s + \sinh r_n^{ms}\hat{a}_n^{s\dagger})\end{aligned} \tag{4.8}$$

We can write the squeezed operators in the measurement OPA basis as a function of the mode overlaps between the measurement OPA's and squeezer OPA's eigenmodes $\sigma_{mn} = \int \mathrm{d}t\ \psi_n^{ms}(t)\psi_m^{s*}(t)$

$$\begin{aligned}\hat{a}_n^s &= \int_{-\infty}^{\infty} \mathrm{d}t\ \psi_n^{ms}(t)\hat{a}^s(t) \\ &= \int_{-\infty}^{\infty} \mathrm{d}t\ \psi_n^{ms}(t)\sum_m \psi_m^{s*}(t)\hat{a}_m^s \\ &= \sum_m \sigma_{mn}\hat{a}_m^s.\end{aligned} \tag{4.9}$$

The output annihilation operator is then

$$\begin{aligned}\hat{a}^{out}(t) &= \sum_{mn} \psi_n^{ms*}(t)(\cosh r_n^{ms}\sigma_{mn}\hat{a}_m^s + \sinh r_n^{ms}\sigma_{mn}^*\hat{a}_m^{s\dagger}) \\ &= \sum_{mn} \psi_n^{ms*}(t)(\cosh r_n^{ms}\sigma_{mn}(\cosh r_m^s\hat{a}_m^{in} + \sinh r_m^s\hat{a}_m^{in\dagger}) \\ &\qquad + \sinh r_n^{ms}\sigma_{mn}^*(\cosh r_m^s\hat{a}_m^{in\dagger} + \sinh r_m^s\hat{a}_m^{in}))\end{aligned} \tag{4.10}$$

For large measurement OPA gains, we use the approximation $\cosh r_n^{ms} \approx \sinh r_n^{ms} \approx \frac{1}{2}\exp(r_n^{ms})$, when $e^{r^{ms}} \gg 1 \gg e^{-r^{ms}}$. Then, the output operator becomes:

$$\hat{a}^{out}(t) = \sum_{mn} \frac{e^{r_n^{ms}}}{2}\psi_n^{ms*}(t)(\sigma_{mn}(\cosh r_m^s\hat{a}_m^{in} + \sinh r_m^s\hat{a}_m^{in\dagger}) + \sigma_{mn}^*(\cosh r_m^s\hat{a}_m^{in\dagger} + \sinh r_m^s\hat{a}_m^{in})) \tag{4.11}$$

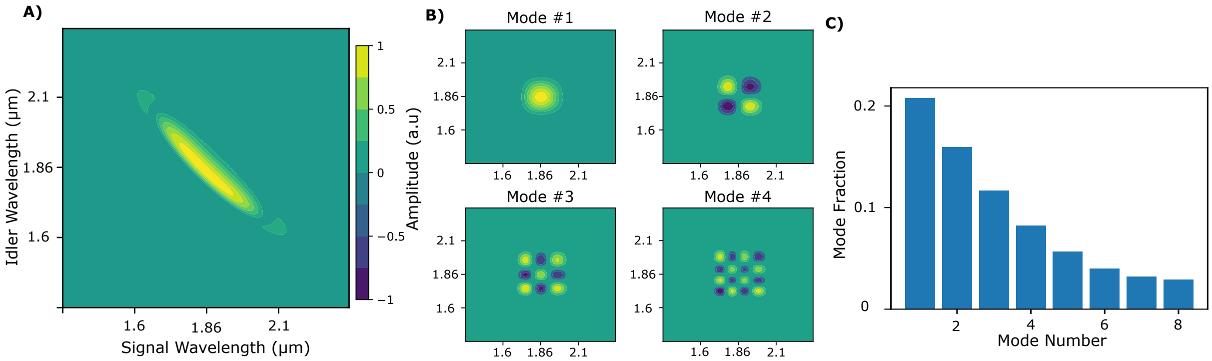

Figure 4.3: A) A plot of the joint-spectral intensity function of the squeezed vacuum produced by our OPA. B) The JSAs corresponding to the first four modes of the JSI calculated via the singular value decomposition $J_n(\omega_s, \omega_i) = \phi_n(\omega_s)\phi_n(\omega_i)$. C) Plot of the mode number vs proportion of mode present in the JSI.

We can write the photon number operator for an individual pulse as

$$\begin{aligned}
\hat{N} &= \int_{-\Delta t}^{\Delta t} \mathrm{d}t\ \hat{a}^{out\dagger}(t)\hat{a}^{out}(t) \\
&= \int \mathrm{d}t \sum_{m,m',n,n'} \frac{e^{r_n^{ms}+r_{n'}^{ms}}}{4}\Big(\psi_n^{ms}(t)(\sigma_{mn}^*(\cosh r_m^s \hat{a}_m^{in\dagger} + \sinh r_m^s \hat{a}_m^{in}) \\
&\qquad + \sigma_{mn}(\cosh r_m^s \hat{a}_m^{in} + \sinh r_m^s \hat{a}_m^{in\dagger}))\Big) \\
&\quad \Big(\psi_{n'}^{ms*}(t)(\sigma_{m'n'}(\cosh r_{m'}^s \hat{a}_{m'}^{in} + \sinh r_{m'}^s \hat{a}_{m'}^{in\dagger}) \\
&\qquad + \sigma_{m'n'}^*(\cosh r_{m'}^s \hat{a}_{m'}^{in\dagger} + \sinh r_{m'}^s \hat{a}_{m'}^{in}))\Big) \\
&= \sum_{m,n} e^{2r_n^{ms}}(\mathrm{Re}[\sigma_{mn}]e^{r_m^s}\hat{x}_m^{in} - \mathrm{Im}[\sigma_{mn}]e^{-r_m^s}\hat{y}_m^{in})^2
\end{aligned} \tag{4.12}$$

where the integral over Δt captures the total time-duration of the pulse, and we have used the orthonormality of the principal modes ($\int \mathrm{d}t\ \psi_n(t)\psi_{n'}^*(t) = \delta_{nn'}$) to insert $\delta_{nn'}$ and $\delta_{mm'}$ and resolve m' and n' in the summation.

Bandpass filtering around degeneracy suppresses the imaginary component of σ_{mn} as imaginary contributions arise from phase walk-off away from degeneracy. Taking $\mathrm{Im}[\sigma_{mn}]e^{-r_m^s} << \mathrm{Re}[\sigma_{mn}]e^{r_m^s}$, which is true when there is low dispersion (as we have engineered our chip for), we have:

$$\hat{N} = \sum_{m,n} \frac{e^{2r_n^{ms}+2r_m^s}}{4}\sigma_{mn}(\hat{a}_m^{in} + \hat{a}_m^{in\dagger})^2, \tag{4.13}$$

If we take a compare to the case of no squeezing from the squeezer OPA ($\sigma_{mn} = \delta_{mn}, r^s_m = 0 \; \forall \; m$),

$$\hat{N} = \sum_n \frac{e^{2r^{ms}_n}}{4}(\hat{a}^{in}_n + \hat{a}^{in\dagger}_n)^2 \tag{4.14}$$

and assume M squeezer modes and N measurement modes, we show that there are now MN modes with effective squeezing parameters $r^{eff}_{m,n} = r^{ms}_n + r^s_m$, whose contributions are weighted by σ_{mn}. From here, we can re-write Eq.4.13 as a function of the quadratures as

$$\hat{N} = \sum_{m,n} \frac{e^{2r^{ms}_n + 2r^s_m}}{8}\sigma_{mn}(\hat{X}^{in}_m)^2 \tag{4.15}$$

In our experiment, we make the assumption that only the first two modes provide significant contributions to the measured statistics as our Schmidt number after filtering is 1.35, and so we truncate m and n to the range $\{1,2\}$. Furthermore, we know that σ_{mn} where m and n are of different parity are zero. This simplifies Eq.4.15 to:

$$\hat{N} = \frac{e^{2r^{ms}_1 + 2r^s_1}}{8}\sigma_{11}(\hat{X}^{in}_1)^2 + \frac{e^{2r^{ms}_2 + 2r^s_2}}{8}\sigma_{22}(\hat{X}^{in}_2)^2 \tag{4.16}$$

This allows us to model the measured photon number distribution as the sum of two independent photon number distributions. During the experiment, we treat the fast photodetector as a macroscopic photon number detector such that $N \propto I_d$ where I_d is the current measured on the detector integrated over a single pulse.

For a single mode, the photon number distribution for bright squeezed vacuum is [27]:

$$P^1_{\langle\hat{N}\rangle}(N, r) = \frac{1}{\sqrt{2\pi N\langle\hat{N}\rangle(r)}}e^{-\frac{N}{2\langle\hat{N}\rangle(r)}} \tag{4.17}$$

with average photon number $\langle\hat{N}\rangle(r) = e^{2r}/4$. Since the photon number contributions from each mode are summed at the detector, we can model the total distribution as the convolution of two single-mode distributions [27, 38], i.e:

$$P^2(N, \theta)_{\langle\hat{N}_1\rangle,\langle\hat{N}_2\rangle} = \int_0^\infty P^1_{\langle\hat{N}_1\rangle}(N - n, \theta)P^1_{\langle\hat{N}_2\rangle}(n, \theta)dn \tag{4.18}$$

where $\langle N(\theta)\rangle$ is the average photon number as a function of relative pump phase between the squeezed vacuum and amplifying measurement OPA pump. By fitting Eq.4.18 to the measured photon number distributions (see Sec. 4.4), we isolate the squeezing parameter of the 1st mode from higher-order modes.

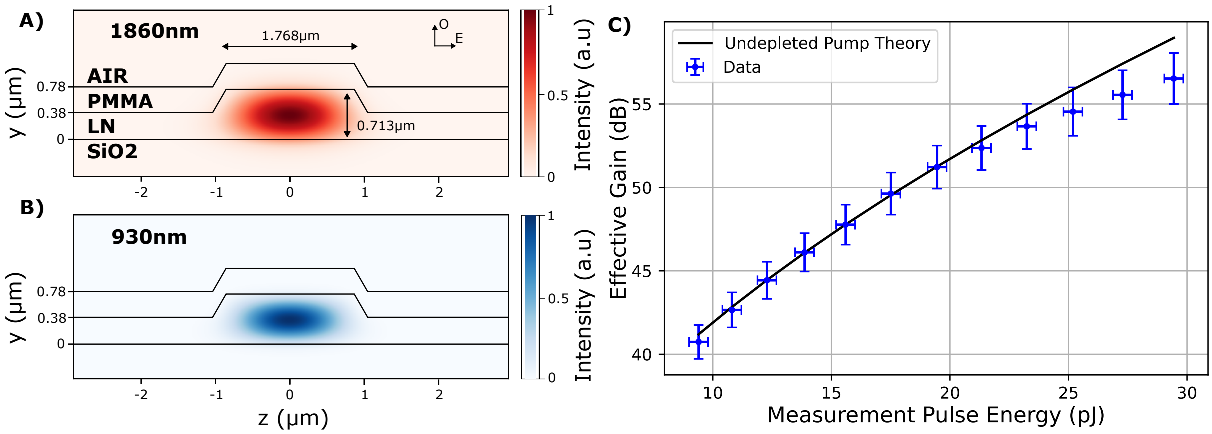

Figure 4.4: A) Signal spatial mode within our waveguide. Text on the right denotes the material stack-up with air, poly methyl methacrylate (PMMA), lithium niobate (LN) and silicon dioxide (SiO2). Dimensions are indicated by the vertical and horizontal measurements. The ordinary and extraordinary crystal axes are denoted at the top right. B) Pump spatial mode. C) OPA gain vs measurement pump energy. Error bars are calculated from pump and signal coupling stability measurements taken before gain measurements.

Intuitively, this convolution can be understood as a sum of all probabilities for which the photon contributions of the first and second modes sum to N as the photodetector cannot distinguish between photons arriving from different modes. These fitted distributions are then sampled and used as inputs to a maximum-likelihood reconstruction algorithm to recover the density matrix and Wigner function [6].

Dispersion Engineering

A key advantage of using nanophotonics is the ability to control the dispersive properties of the waveguides used to create photonic circuits. Figure 4.4 depicts our ridge waveguide geometry and material stack used for our OPAs. We fabricate our OPAs on a thin-film lithium niobate (TFLN) on silica on silicon wafers available from NanoLN. By adjusting the width, height and etch depth of the waveguide, we can manipulate its dispersive properties to achieve low group velocity dispersion (GVD) at the pump and signal wavelengths while simultaneously minimizing the walk-off from group velocity mismatch (GVM) between the pump and signal [34]. This regime of operation allows for our OPA to exhibit high gain over a broad bandwidth, making it an ideal tool for studying quantum states encoded in ultrafast pulses. Our waveguide geometry achieves a GVD of -17.3 fs^2/mm at our signal wavelength of 1860 nm, 244 fs^2/mm at our pump wavelength

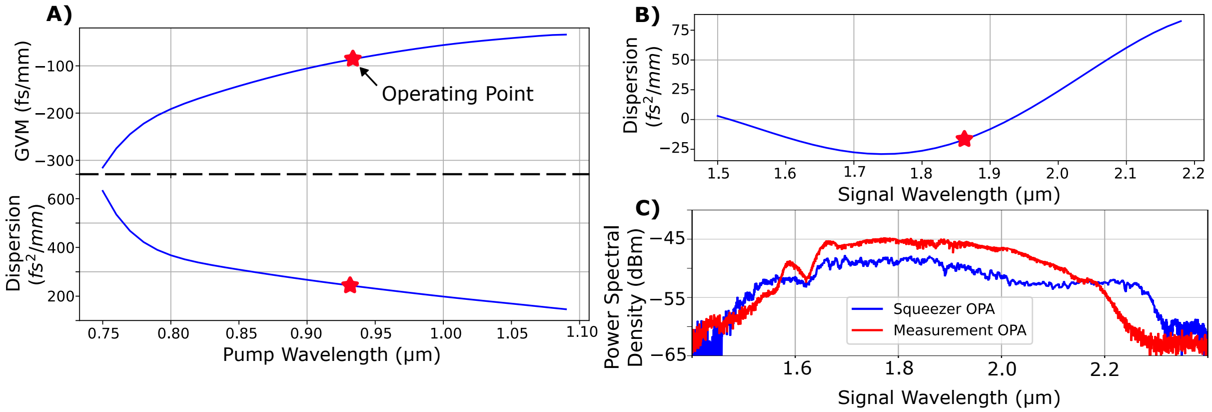

Figure 4.5: A) Pump dispersion and group-velocity mismatch (calculated at degeneracy and plotted at the pump wavelength) for our OPA. B) Signal dispersion vs wavelength. C) Parametric generation (vacuum amplification) spectra of our measurement and squeezer OPAs.

of 930 nm, and a GVM of −87 fs/mm. By comparison, bulk lithium niobate has a GVD of 13.3 fs^2/mm at 1860 nm, a GVD of 341 fs^2/mm at 930 nm, and a GVM of 203 fs/mm. A thin layer of poly-methyl methacrylate (PMMA) is deposited via spin-coating on top of the waveguide to tune the phase matching condition. We note that our design is not perfectly optimal, and that geometries with lower dispersion have been demonstrated [34].

Operating with low dispersion allows us to utilize ultrafast femtosecond pulses at both the pump and signal frequencies. Shorter pulses are advantageous in nonlinear optics as the high peak power from temporal confinement can achieve a stronger nonlinear interaction for the same pulse energy. This interaction is also enhanced by the tight spatial mode confinement offered by ridge waveguides. Furthermore, by shortening the length of the pump and signal pulses in the time domain, subsequent pulses can be packed closer together in time, enabling a significant boost in clock speeds for time-multiplexing. Based on the dispersive properties of our 5-mm measurement OPA and our 70-fs pump source, we estimate an upper bound on the temporal length of our SV of 154.3 fs, which gives a theoretical maximum of 6.5 THz for our clock rate [61]. This clock rate can be increased further by using a shorter OPA and a higher pump power, or more advanced dispersion engineering.

Dispersion engineering in TFLN has been used to demonstrate broadband amplifiers with record-breaking gain bandwidths [34]. Dispersion-engineered OPAs have been shown to be suitable devices for both generating and measuring the time-averaged squeezing of

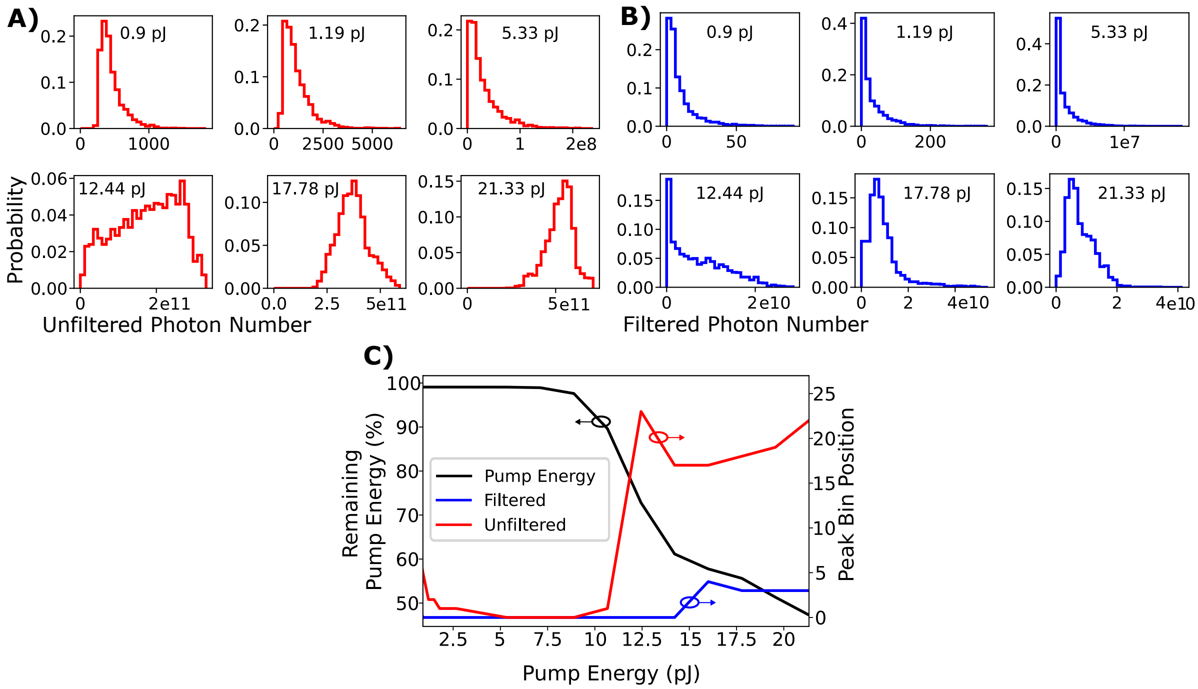

Figure 4.6: A) Simulated photon number distributions for unfiltered detection across different pump energies. B) Simulated photon number distributions for 20-nm bandpass filtered detection across different pump energies. C) A plot of the remaining pump energy after pulse propagation (lower remaining energy is a more depleted pump), and the peak histogram bin for the unfiltered and filtered simulations.

SV [45] as well as producing short-pulse biphotons [63]. Ultrafast switching [17], and ultrafast computation of nonlinear functions for machine learning have been achieved [36]. Combining these OPAs with resonators has allowed new regimes of nonlinearity to be studied which were previously impossible to achieve in bulk platforms [51].

Calculation of the Joint Spectral Intensity and its Modes

Figure 4.3A shows the joint-spectral intensity function (JSI) of the squeezed vacuum we measure. We calculate our JSI using the dispersive parameters obtained from mode simulations, the input pump pulse energy, and the resources from [21]. The modes of the JSI are found by performing the Bloch-Messiah decomposition which calculates the modes such that the correlations between pairs of modes are minimized. The first four modes are plotted in Fig. 4.3B and the fraction of the first eight modes comprising the JSI is shown in Fig. 4.3C. The JSI decomposition reveals a Schmidt mode number of 7.1. This same calculation can be repeated for the measurement OPA resulting in a Schmidt number of 3.9. Filtering before detection reduces this number to 1.35.

Pump Depletion

An important consideration for OPAs as quantum measurement devices is the depletion experienced by the pump during amplification. As the pump energy increases, the nonlinear interaction becomes more efficient, causing the pump pulse to deplete while propagating in the OPA and the gain to saturate. Figure 4.4C shows measured on-chip OPA gain vs the input pump energy. The black line represents the theoretical undepleted pump gain $G_{dB} = 10\log_{10}(e^{b\sqrt{E}})$ where E is the pump energy in Joules and b is found by fitting the pump energy vs gain curve in the undepleted regime. Around 20 pJ, the measured gain begins to saturate relative to the theoretical gain due to pump depletion effects.

Pump depletion impacts our measurement in two ways. First, the larger photon number components of the state being measured experience less gain than smaller photon number components. This phenomenon, often known as gain saturation for classical amplifiers, suppresses the larger photon number contributions to the measured photon number distribution. Second, pump depletion can be thought of as a semi-deterministic transfer of energy from the pump pulse to the signal pulse. This causes the peak of the photon number distribution to shift away from $N = 0$. We observe this effect in classical simulations which use a split-step Fourier method to simulate single-mode and multimode vacuum measurements. These simulations are detailed in the supplementary. This effect has also been observed in single-mode quantum simulations [8] and experimentally [13]. We address this issue when fitting our data with 2-mode distributions by fitting a constant offset along the N axis, leading to good agreement between the measured data and fitted distributions.

We model the effects of pump depletion as a shift in the peak of the photon number distribution. Figure 4.6 shows semi-classical simulation results of vacuum amplification in our OPA generated via a split-step Fourier method. As pump energy increases, the pump pulse depletes more efficiently given the peak-power-enhanced nonlinear interaction, and causes the peak of $P(N)$ to shift away from 0. Fig. 4.6B shows simulated $P(N)$ with 20-nm bandpass filtering at degeneracy before measurement. In this case, the dominant contribution to the peak shift is pump depletion as multimode effects are suppressed. The difference can be seen in Fig. 4.6A where in the unfiltered case, peak shifting is more prominent thanks to strong multimode contributions. Peak shifting as a result of pump depletion has recently been studied in single-mode quantum simulations [8] and experimentally observed [13].

4.3 Experimental Setup

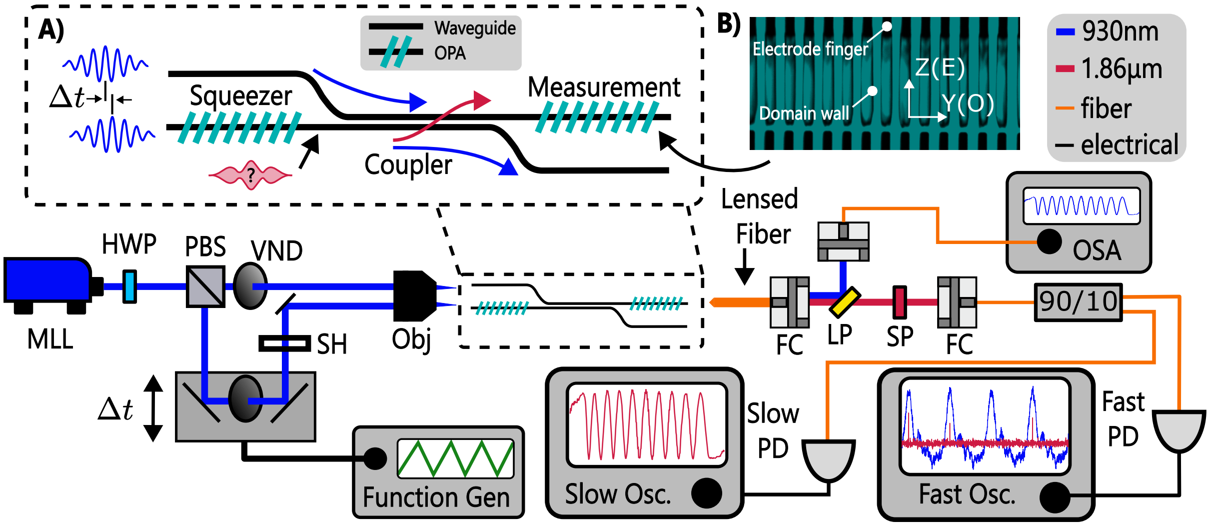

Figure 4.7: Experimental setup. MLL: Titanium:sapphire tunable mode-locked laser. PBS: polarizing beamsplitter. VND: variable neutral density filter. SH: mechanical shutter. Obj: reflective objective. FC: reflective fiber collimator. LP and SP: long-pass and short-pass wavelength filters. 90/10: fiber splitter with 90% going to the fast detector and 10% going to the slow oscilloscope. PD: photodetector. Fast Osc: 80 GSPS 40 GHz oscilloscope. Slow Osc: 100 MSPS 10 MHz oscilloscope.

Figure 4.7 shows the experimental setup. An 80 MHz mode-locked titanium-sapphire laser (MLL) sends 70-fs pulses to a half-wave plate (HWP) and polarizing beamsplitter (PBS) combination to control the power splitting between the measurement and squeezer beam paths. Pump light for the squeezer OPA is sent to a delay stage used to scan θ in equation 4.1. A shutter is also placed in this path to block the squeezer beam for shot-noise calibration. Two continuously variable neutral density filters (VND) are used in both paths to fine tune the input power. The paths are combined on a reflective objective (Obj) and focused onto the waveguide inputs for the OPAs. Figure 4.7A shows the layout of the nanophotonic circuit. In the squeezer OPA, the vacuum field around 1860 nm is squeezed by the pump. The SV and the remaining pump light enter an adiabatic coupler which passes at least 55% of the SV and 5% of the pump into the measurement OPA. Inside the measurement OPA, the SV is amplified by a strong pump pulse (40 pJ) to macroscopic photon levels detectable by a fast photodetector. A lensed fiber collects light from the output of the measurement OPA and directs it to a series of free-space filters used to remove remaining pump light, including the previously mentioned 1700-nm long pass and a 1950-nm short pass for limiting the measured mode number. From here, the filtered SV is collected into single-mode fiber and enters a 90/10 splitter where 90% is sent to a fast (10 GHz) photodetector and fast (80 GSPS 40 GHz) oscilloscope used to resolve individual pulses while the remaining 10% is sent to a slow (1MHz) detector and slow (100 MSPS 10 MHz) oscilloscope used to detect the amplification fringe and determine the measurement phase θ.

4.4 Data Analysis

Shot-noise Calibration

Initial characterization of the shot noise and squeezing levels is performed using a slow photodetector and an optical spectrum analyzer (OSA) which replaces the fast detector in Fig. 4.7. This data is used to calibrate the shot noise of the measurement OPA and measure the squeezing generated by the squeezer OPA (See [44] supplementary). During calibration, the mechanical shutter is initially left open. As the relative delay of the squeezer path is scanned, the measurement amplifier oscillates between measuring squeezed and anti-squeezed quadratures, resulting in the black curve in Fig. 4.8A. The remaining pump light collected from the output is monitored on a second OSA. Because the optical coupler between the measurement and squeezer OPAs couples some of the pump used to drive the squeezer, the measurement and squeezer pumps interfere inside the measurement OPA, causing the gain, and therefore shot-noise level, of the measurement OPA to depend on θ. The shutter is then closed and the baseline shot noise is measured by the OSA resulting in the gray curve in Fig. 4.8A.

To determine the shot-noise levels corresponding to the minimum and maximum of the squeezing curve, the measurement OPA power is lowered using the VND until the measured pump power matches the minima of the pump interference. The shot-noise minimum is then measured on the slow photodetector and OSA resulting in the red curve in Fig. 4.8A. This same procedure is repeated for the shot-noise maximum as well to calibrate the anti-squeezing and obtain the blue curve. The pump OSA is set to measure around 970 nm to minimize any pump depletion effects. After shot-noise calibration, the squeezing is calculated as:

$$S_{\pm}^{\theta}[dB] = 10 \log_{10} \left[\frac{\langle N(\theta) \rangle}{\langle N_{vac} \rangle} \right] \tag{4.19}$$

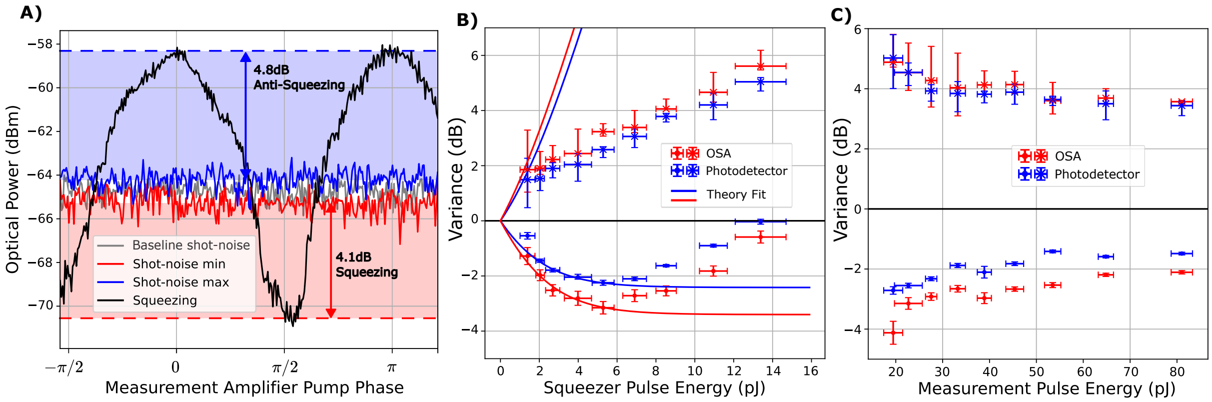

Figure 4.8: A) Squeezing measurement taken on the OSA. The black curve is the amplification fringe produced from squeezed vacuum amplified by the measurement OPA. The grey curve is the baseline shot noise at the pump power used to measure the black curve. The red and blue curves are the corrected shot-noise levels to account for pump interference in the measurement OPA. B) Variance relative to vacuum vs squeezer pulse energy with a measurement pulse energy of 30 pJ. C) Variance relative to vacuum vs measurement pulse energy. Error bars are calculated from shot-noise variations during each measurement.

where $\langle N(\theta)\rangle$ is proportional to the current measured at the detector, and $\langle N_{vac}\rangle$ is the calibrated shot noise from amplifying vacuum. We note that the variance of the measured quadrature is proportional to the average photon number for a state with zero mean field such as SV [45].

Slow Photodetector Measurements

Figure 4.8B shows the measured squeezing on the slow photodetector and OSA as a function of the input pulse energy for the squeezer waveguide with a measurement pulse energy of 30 pJ. For these measurements, the 1950-nm short-pass filter is removed to accentuate the impact of multiple modes (a Schmidt number of 2.8). Because the OSA uses a 2-nm bandpass filter, it can better suppress higher-order modes to isolate the squeezing in the fundamental mode [21, 44]. For the photodetector, the presence of higher-order modes with less squeezing reduces overall measured squeezing as the photodetector is not mode-sensitive and measures the squeezing as averaged over all modes. At low squeezer pulse energies, the measured squeezing is limited by the gain available in the squeezer OPA and grows as the pulse energy is increased. After 5 pJ, the observed squeezing begins to decrease with increasing pulse energy. Two phenomena contribute to this behavior. First, the finite phase noise of the pump laser causes a portion of the anti-squeezed quadrature to leak into the measurement of the squeezed quadrature. Raising the squeezer gain increases the contribution of the anti-squeezing to the measurement and reduces the measured squeezing. This increased gain produces more squeezing, but the noise reduction in the squeezed quadrature is asymptotically limited by the finite efficiency of the coupler while the noise of the anti-squeezed quadrature is not (see solid theory curves in Fig. 4.8B). Second, nonlinear behavior in the measurement amplifier increases with input power and further degrades measured squeezing.

The solid lines plotted in Fig. 4.8B are calculated from the theoretical measured squeezing as a function of the coupling loss from the squeezer to measurement OPA. As SV passes through the coupler, some of the light is lost to propagation losses and fabrication imperfections in the coupler. This light is replaced with vacuum noise, causing lower squeezing and anti-squeezing values to be measured [19]. For a given measurement efficiency η, the measured squeezing can be modeled as

$$S_{\pm}^{\eta}[dB] = 10\log_{10}[(1-\eta) + \eta e^{\pm 2r}] \tag{4.20}$$

Where r is the on-chip squeezer gain in natural log units (i.e. the squeezing parameter). Using this fit, we estimate an effective measurement efficiency (η) of 55% at 1860 nm. This fit includes squeezing lost to inefficiencies in our coupler as well as losses to nonlinear behavior in the measurement OPA. This fitting also allows us to calculate the expected anti-squeezing, however we can see that the measured data has a stark divergence from the expected trend. This is a result of the gain compression in the measurement OPA. Because the measurement OPA operates in the pump depleted regime, the anti-squeezed vacuum cannot be sufficiently amplified to reflect the true anti-squeezing entering the OPA. The same is true for the squeezing measurements in which the shot-noise level becomes compressed, leading to lower measured squeezing.

The effects of gain depletion can also be seen in Fig. 4.8C which plots the measured squeezing values vs the measurement pulse energy for a fixed squeezer energy of 5 pJ. As the measurement pulse energy is decreased, the measurement OPA experiences less gain depletion, leading to higher measured squeezing and anti-squeezing. In the undepleted pump regime, measured squeezing and anti-squeezing will follow Eq.4.20 and remain unchanged with small changes in pump energy. Hence, we know all measurements in Fig. 4.8B are taken in the pump depletion regime. This is also confirmed from Fig. 4.4C

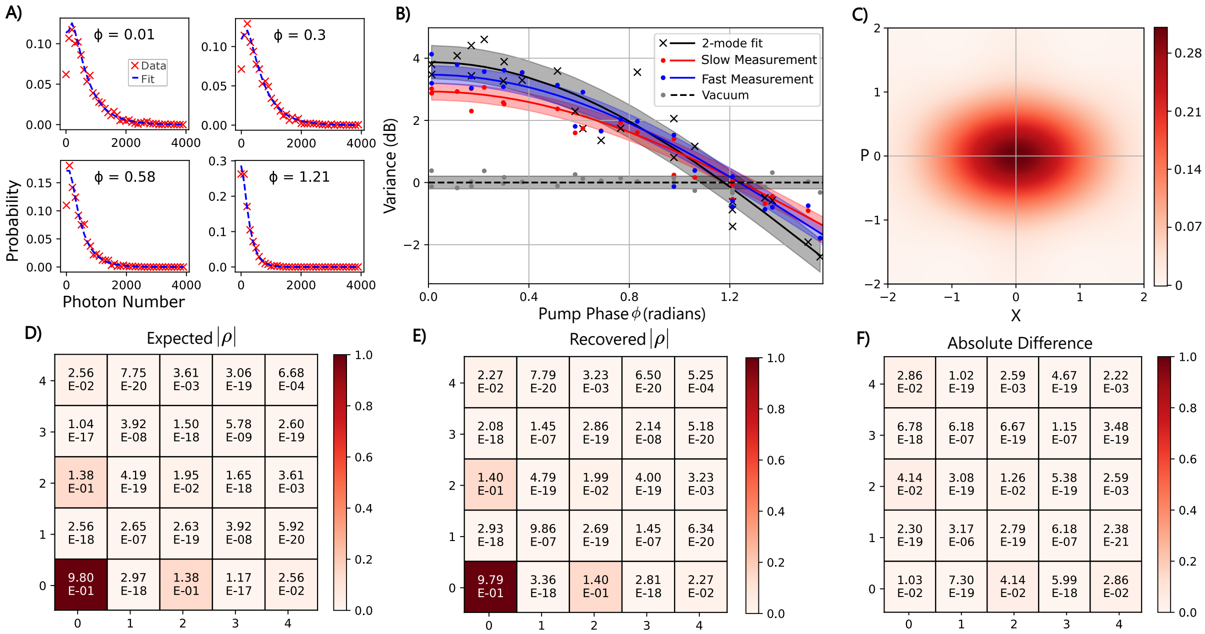

Figure 4.9: A) Sample photon number distributions from fast measurements at different θ. Red points are data, blue curve is a 2-mode fit. B) Photon number variance vs θ for slow and fast (pulse-to-pulse) measurements, and the 1st mode of a 2-mode fit. C) Recovered squeezed vacuum Wigner function. D) Expected density matrix (ρ) based on measured squeezing and anti-squeezing. E) Recovered ρ. F) Absolute difference between expected and recovered ρ.

where pump depletion effects take hold around 20 pJ. Below 20 pJ, the shot noise no longer clears the electronic noise floor of the OSA, preventing squeezing measurements at lower measurement pump energies. This problem can be mitigated by improving output coupling efficiency and operating the measurement OPA at a lower pump power.

Pulse-to-pulse Measurements

Fast photodetector measurements resolve the pulse-to-pulse photon number and provide the statistical information necessary to measure $P(N, \theta)$ and recover the Wigner function of a symmetric state. Before a fast measurement, a slow measurement is conducted with the OSAs to calibrate the shot noise. During each fast measurement, the shutter is initially left open, and the fast oscilloscope is triggered using the voltage applied to the piezo driving the squeezer's delay stage to coincide with the middle of the θ scan. Data from the slow oscilloscope is used to determine θ and estimate the coupling stability based on measurement-to-measurement variations in the shot noise. After recording data, the squeezer's shutter is closed and the measurement is repeated to find the calibrated shot-noise level.

Figure 4.9 shows results gathered from fast photodetector measurements for a squeezer pulse energy of 5 pJ and a measurement pulse energy of 45 pJ. Sample measured histograms at 4 different phases are plotted in Fig. 4.9A, and each histogram corresponds to a single data point in Fig. 4.9B. For each measurement, we fit the 2-mode photon number distribution model in Eqn. 4.18 to extract the variance of the fundamental mode as a function of the amplified quadrature phase of the squeezed vacuum θ. Figure 4.9B shows these measurements for three cases: slow photodetector measurements, fast photodetector measurements, and the 2-mode fit. Slow measurement values are calculated from the slow oscilloscope trace using the method outlined in section 4.4. Because of the photon number offset resulting from pump depletion, the numerator and denominator of Eq.4.19 have a small but constant offset, resulting in the measured squeezing and anti-squeezing being underestimated. Fast measurement values are calculated using the variance of the photon numbers measured at the fast detector. This overcomes the offset problem and measures more squeezing and anti-squeezing, but these measurements are still contaminated with remaining contributions from higher-order modes. The 2-mode fit addresses this problem by isolating the variance as a function of θ for the fundamental mode, leading to higher measured squeezing and anti-squeezing. After performing this fit for all measurements, the distributions are re-sampled and fed into a maximum likelihood algorithm which calculates the Wigner functions for squeezing data (Fig. 4.9C). We extract a squeezing in the fundamental mode of 2.41 ± 0.34 dB and an anti-squeezing of 3.87 ± 0.61 dB, which corresponds to a state purity of 0.929 ± 0.044. Figure 4.9E shows the recovered density matrix corresponding to the Wigner function plotted in Fig. 4.9C. We show the expected density matrix given the measured squeezing and anti-squeezing in Fig. 4.9D, and the absolute difference between the expected and recovered in Fig. 4.9F where we calculate a fidelity of 0.9998 ± 0.0001. While our fitting strategy limits us to states with known distributions, we can overcome this limitation with tighter bandpass filtering to better reject higher-order modes. Our losses between the chip and fiber (10 dB) and from our filter setup (6 dB) currently prevent us from tighter filtering as the remaining light is no longer strong enough to provide a sufficiently large signal-to-noise ratio at the fast photodetector.

4.5 Conclusion

We have demonstrated OPA-based state tomography for squeezed vacuum in the ultrafast regime using dispersion-engineered TFLN. The low dispersion of our OPA design allows operation with ultra-short pulses to exceed the bandwidth of homodyne measurement and access a new regime of THz repetition-rate measurement and computation. With narrower bandpass filtering at the output of our OPA, modest improvements in detection efficiency, and a generalization of our state tomography algorithm, we can perform Wigner tomography on arbitrary symmetric quantum states encoded in femtosecond optical pulses. We show that ultrafast nanophotonic OPAs can serve as quantum measurement devices, paving the way for ultrafast quantum information processing to be realized in a room-temperature chip-scale platform.

References

[1] Ayman F Abouraddy, Magued B Nasr, Bahaa EA Saleh, Alexander V Sergienko, and Malvin C Teich. "Quantum-optical coherence tomography with dispersion cancellation". In: *Physical Review A* 65.5 (2002), p. 053817.

[2] Frank Acasiete, Flavia P Agostini, J Khatibi Moqadam, and Renato Portugal. "Implementation of quantum walks on IBM quantum computers". In: *Quantum Information Processing* 19 (2020), pp. 1–20.

[3] Vahid Ansari, Georg Harder, Markus Allgaier, Benjamin Brecht, and Christine Silberhorn. "Temporal-mode measurement tomography of a quantum pulse gate". In: *Physical Review A* 96.6 (2017), p. 063817.

[4] Warit Asavanant, Yu Shiozawa, Shota Yokoyama, Baramee Charoensombutamon, Hiroki Emura, Rafael N. Alexander, Shuntaro Takeda, Jun-ichi Yoshikawa, Nicolas C. Menicucci, Hidehiro Yonezawa, and Akira Furusawa. "Generation of time-domain-multiplexed two-dimensional cluster state". In: *Science* 366.6463 (Oct. 18, 2019), pp. 373–376. DOI: `10.1126/science.aay2645`.

[5] Ismail Barakat, Mahmoud Kalash, Dennis Scharwald, Polina Sharapova, Norbert Lindlein, and Maria Chekhova. *Simultaneous measurement of multimode squeezing*. Feb. 24, 2024. arXiv: `2402.15786[quant-ph]`.

[6] William Bidle. "Optical Quantum State Tomography". In: *Department of Physics & Astronomy* (2023).

[7] Carlton M. Caves. "Quantum-mechanical noise in an interferometer". In: *Physical Review D* 23.8 (Apr. 15, 1981), pp. 1693–1708. DOI: `10.1103/PhysRevD.23.1693`.

[8] Karthik Chinni and Nicolás Quesada. "Beyond the parametric approximation: Pump depletion, entanglement, and squeezing in macroscopic down-conversion". In: *Physical Review A* 110.1 (2024), p. 013712.

[9] Hugo Defienne, Warwick P Bowen, Maria Chekhova, Gabriela Barreto Lemos, Dan Oron, Sven Ramelow, Nicolas Treps, and Daniele Faccio. "Advances in quantum imaging". In: *Nature Photonics* (2024), pp. 1–13.

[10] Christian L Degen, Friedemann Reinhard, and Paola Cappellaro. “Quantum sensing”. In: *Reviews of modern physics* 89.3 (2017), p. 035002.

[11] Andreas Eckstein, Benjamin Brecht, and Christine Silberhorn. “A quantum pulse gate based on spectrally engineered sum frequency generation”. In: *Optics express* 19.15 (2011), pp. 13770–13778.

[12] Xiao-Tian Fang, Pei Zeng, Hui Liu, Mi Zou, Weijie Wu, Yan-Lin Tang, Ying-Jie Sheng, Yao Xiang, Weijun Zhang, Hao Li, et al. “Implementation of quantum key distribution surpassing the linear rate-transmittance bound”. In: *Nature Photonics* 14.7 (2020), pp. 422–425.

[13] Jefferson Flórez, Jeff S Lundeen, and Maria V Chekhova. “Pump depletion in parametric down-conversion with low pump energies”. In: *Optics Letters* 45.15 (2020), pp. 4264–4267.

[14] G. Frascella, E. E. Mikhailov, N. Takanashi, R. V. Zakharov, O. V. Tikhonova, and M. V. Chekhova. “Wide-field SU(1,1) interferometer”. In: *Optica* 6.9 (Sept. 2019), pp. 1233–1236. DOI: 10.1364/OPTICA.6.001233.

[15] Thomas Gerrits, Scott Glancy, Tracy S Clement, Brice Calkins, Adriana E Lita, Aaron J Miller, Alan L Migdall, Sae Woo Nam, Richard P Mirin, and Emanuel Knill. “Generation of optical coherent-state superpositions by number-resolved photon subtraction from the squeezed vacuum”. In: *Physical Review A* 82.3 (2010), p. 031802.

[16] Nicolas Gisin and Rob Thew. “Quantum communication”. In: *Nature photonics* 1.3 (2007), pp. 165–171.

[17] Qiushi Guo, Ryoto Sekine, Luis Ledezma, Rajveer Nehra, Devin J Dean, Arkadev Roy, Robert M Gray, Saman Jahani, and Alireza Marandi. “Femtojoule femtosecond all-optical switching in lithium niobate nanophotonics”. In: *Nature Photonics* 16.9 (2022), pp. 625–631.

[18] Vikas Hassija, Vinay Chamola, Vikas Saxena, Vaibhav Chanana, Prakhar Parashari, Shahid Mumtaz, and Mohsen Guizani. “Present landscape of quantum computing”. In: *IET Quantum Communication* 1.2 (2020), pp. 42–48.

[19] Charles H Henry and Rudolf F Kazarinov. “Quantum noise in photonics”. In: *Reviews of Modern Physics* 68.3 (1996), p. 801.

[20] Bryce P. Hickam, Manni He, Nathan Harper, Szilard Szoke, and Scott K. Cushing. “Single-Photon Scattering Can Account for the Discrepancies among Entangled Two-Photon Measurement Techniques”. In: *The Journal of Physical Chemistry Letters* 13.22 (2022). PMID: 35635002, pp. 4934–4940. DOI: 10.1021/acs.jpclett.2c00865. eprint: https://doi.org/10.1021/acs.jpclett.2c00865.

[21] Martin Houde and Nicolás Quesada. “Waveguided sources of consistent, single-temporal-mode squeezed light: The good, the bad, and the ugly”. In: *AVS Quantum Science* 5.1 (2023).

[22] Martin Houde and Nicolás Quesada. "Waveguided sources of consistent, single-temporal-mode squeezed light: the good, the bad, and the ugly". In: *CLEO 2023 (2023), paper FF1L.6*. CLEO: Fundamental Science. Optica Publishing Group, May 7, 2023, FF1L.6. DOI: 10.1364/CLEO_FS.2023.FF1L.6.

[23] Anqi Huang, Shihan Sajeed, Poompong Chaiwongkhot, Mathilde Soucarros, Matthieu Legré, and Vadim Makarov. "Gap between industrial and academic solutions to implementation loopholes: testing random-gate-removal countermeasure in commercial QKD system". In: *Unpublished full-text manuscript from Vadim Makarov* (2018).

[24] Florian Hudelist, Jia Kong, Cunjin Liu, Jietai Jing, ZY Ou, and Weiping Zhang. "Quantum metrology with parametric amplifier-based photon correlation interferometers". In: *Nature communications* 5.1 (2014), p. 3049.

[25] Darren Hurley-Smith and Julio Hernandez-Castro. "Quam bene non quantum: Identifying bias in a commercial quantum random number generator". In: *Unpublished full-text manuscript from ResearchGate. Presented at Real World Crypto* (2018).

[26] A. Inoue, T. Kashiwazaki, T. Yamashima, N. Takanashi, T. Kazama, K. Enbutsu, K. Watanabe, T. Umeki, M. Endo, and A. Furusawa. "Toward a multi-core ultrafast optical quantum processor: 43-GHz bandwidth real-time amplitude measurement of 5-dB squeezed light using modularized optical parametric amplifier with 5G technology". In: *Applied Physics Letters* 122.10 (Mar. 2023), p. 104001. DOI: 10.1063/5.0137641.

[27] Mahmoud Kalash and Maria V. Chekhova. "Wigner function tomography via optical parametric amplification". In: *Optica* 10.9 (Sept. 20, 2023), p. 1142. DOI: 10.1364/OPTICA.488697.

[28] Shunya Konno, Warit Asavanant, Fumiya Hanamura, Hironari Nagayoshi, Kosuke Fukui, Atsushi Sakaguchi, Ryuhoh Ide, Fumihiro China, Masahiro Yabuno, Shigehito Miki, et al. "Logical states for fault-tolerant quantum computation with propagating light". In: *Science* 383.6680 (2024), pp. 289–293.

[29] Shunya Konno, Warit Asavanant, Fumiya Hanamura, Hironari Nagayoshi, Kosuke Fukui, Atsushi Sakaguchi, Ryuhoh Ide, Fumihiro China, Masahiro Yabuno, Shigehito Miki, et al. "Propagating Gottesman-Kitaev-Preskill states encoded in an optical oscillator". In: *arXiv preprint arXiv:2309.02306* (2023).

[30] Leong-Chuan Kwek, Lin Cao, Wei Luo, Yunxiang Wang, Shihai Sun, Xiangbin Wang, and Ai Qun Liu. "Chip-based quantum key distribution". In: *AAPPS Bulletin* 31 (2021), pp. 1–8.

[31] Kaisa Laiho, Katiúscia N Cassemiro, David Gross, and Christine Silberhorn. "Probing the negative Wigner function of a pulsed single photon point by point". In: *Physical review letters* 105.25 (2010), p. 253603.

[32] Mikkel V. Larsen, Xueshi Guo, Casper R. Breum, Jonas S. Neergaard-Nielsen, and Ulrik L. Andersen. "Deterministic generation of a two-dimensional cluster state". In: *Science* 366.6463 (Oct. 18, 2019), pp. 369–372. DOI: 10.1126/science.aay4354.

[33] B. J. Lawrie, P. D. Lett, A. M. Marino, and R. C. Pooser. "Quantum Sensing with Squeezed Light". In: *ACS Photonics* 6.6 (June 19, 2019), pp. 1307–1318. DOI: 10.1021/acsphotonics.9b00250.

[34] Luis Ledezma, Ryoto Sekine, Qiushi Guo, Rajveer Nehra, Saman Jahani, and Alireza Marandi. "Intense optical parametric amplification in dispersion-engineered nanophotonic lithium niobate waveguides". In: *Optica* 9.3 (Mar. 20, 2022), p. 303. DOI: 10.1364/OPTICA.442332.

[35] Christian Leefmans, Avik Dutt, James Williams, Luqi Yuan, Midya Parto, Franco Nori, Shanhui Fan, and Alireza Marandi. "Topological dissipation in a time-multiplexed photonic resonator network". In: *Nature Physics* 18.4 (2022), pp. 442–449.

[36] Gordon H.Y. Li, Ryoto Sekine, Rajveer Nehra, Robert M. Gray, Luis Ledezma, Qiushi Guo, and Alireza Marandi. "All-optical ultrafast ReLU function for energy-efficient nanophotonic deep learning". In: *Nanophotonics* 12.5 (Mar. 10, 2023), pp. 847–855. DOI: 10.1515/nanoph-2022-0137.

[37] Sheng-Kai Liao, Wen-Qi Cai, Wei-Yue Liu, Liang Zhang, Yang Li, Ji-Gang Ren, Juan Yin, Qi Shen, Yuan Cao, Zheng-Ping Li, et al. "Satellite-to-ground quantum key distribution". In: *Nature* 549.7670 (2017), pp. 43–47.

[38] Noah Lordi, Eugene J. Tsao, Alexander J. Lind, Scott A. Diddams, and Joshua Combes. "Quantum theory of temporally mismatched homodyne measurements with applications to optical-frequency-comb metrology". In: *Physical Review A* 109.3 (Mar. 25, 2024), p. 033722. DOI: 10.1103/PhysRevA.109.033722.

[39] Mhlambululi Mafu and Makhamisa Senekane. "Implementation and Security Analysis of the B92 Protocol using Id3100 Clavis2 System". In: *Applied Mathematics & Information Sciences* 15.5 (2021), pp. 661–666.

[40] Michael L Marable, Sang-Kyung Choi, and Prem Kumar. "Measurement of quantum-noise correlations in parametric image amplification". In: *Optics Express* 2.3 (1998), pp. 84–92.

[41] A. M. Marino, N. V. Corzo Trejo, and P. D. Lett. "Effect of losses on the performance of an SU(1,1) interferometer". In: *Physical Review A* 86.2 (Aug. 24, 2012), p. 023844. DOI: 10.1103/PhysRevA.86.023844.

[42] Horowitz Mark, Grumbling Emily, National Academies of Sciences Engineering, Medicine, et al. *Quantum computing: progress and prospects.* The National Academies Press, 2019.

[43] L McCuller, C Whittle, D Ganapathy, K Komori, M Tse, A Fernandez-Galiana, L Barsotti, Peter Fritschel, M MacInnis, F Matichard, et al. “Frequency-dependent squeezing for advanced LIGO”. In: *Physical review letters* 124.17 (2020), p. 171102.

[44] Rajveer Nehra, Ryoto Sekine, Luis Ledezma, Qiushi Guo, Robert M Gray, Arkadev Roy, and Alireza Marandi. “Few-cycle vacuum squeezing in nanophotonics”. In: *Science* 377.6612 (2022), pp. 1333–1337.

[45] Rajveer Nehra, Ryoto Sekine, Luis Ledezma, Qiushi Guo, Robert M. Gray, Arkadev Roy, and Alireza Marandi. “Few-cycle vacuum squeezing in nanophotonics”. In: *Science* 377.6612 (Sept. 16, 2022), pp. 1333–1337. DOI: 10.1126/science.abo6213.

[46] Rajveer Nehra, Aye Win, Miller Eaton, Reihaneh Shahrokhshahi, Niranjan Sridhar, Thomas Gerrits, Adriana Lita, Sae Woo Nam, and Olivier Pfister. “State-independent quantum state tomography by photon-number-resolving measurements”. In: *Optica* 6.10 (2019), pp. 1356–1360.

[47] Masayuki Okano, Hwan Hong Lim, Ryo Okamoto, Norihiko Nishizawa, Sunao Kurimura, and Shigeki Takeuchi. “0.54 μm resolution two-photon interference with dispersion cancellation for quantum optical coherence tomography”. In: *Scientific reports* 5.1 (2015), p. 18042.

[48] E Pavel, SI Jinga, BS Vasile, A Dinescu, V Marinescu, R Trusca, and N Tosa. “Quantum optical lithography from 1 nm resolution to pattern transfer on silicon wafer”. In: *Optics & Laser Technology* 60 (2014), pp. 80–84.

[49] Google AI Quantum, Collaborators*†, Frank Arute, Kunal Arya, Ryan Babbush, Dave Bacon, Joseph C Bardin, Rami Barends, Sergio Boixo, Michael Broughton, Bob B Buckley, et al. “Hartree-Fock on a superconducting qubit quantum computer”. In: *Science* 369.6507 (2020), pp. 1084–1089.

[50] Jonathan Roslund, Renné Medeiros de Araújo, Shifeng Jiang, Claude Fabre, and Nicolas Treps. “Wavelength-multiplexed quantum networks with ultrafast frequency combs”. In: *Nature Photonics* 8.2 (Feb. 2014), pp. 109–112. DOI: 10.1038/nphoton.2013.340.

[51] Ryoto Sekine, Robert M Gray, Luis Ledezma, Selina Zhou, Qiushi Guo, and Alireza Marandi. “Multi-octave frequency comb from an ultra-low-threshold nanophotonic parametric oscillator”. In: *arXiv preprint arXiv:2309.04545* (2023).

[52] Laura Serino, Werner Ridder, Abhinandan Bhattacharjee, Jano Gil-Lopez, Benjamin Brecht, and Christine Silberhorn. “Orchestrating time and color: a programmable source of high-dimensional entanglement”. In: *Optica Quantum* 2.5 (Oct. 25, 2024), pp. 339–345. DOI: 10.1364/OPTICAQ.532334.

[53] Yaakov Shaked, Yoad Michael, Rafi Z. Vered, Leon Bello, Michael Rosenbluh, and Avi Pe’er. “Lifting the bandwidth limit of optical homodyne measurement with broadband parametric amplification”. In: *Nature Communications* 9.1 (Feb. 9, 2018), p. 609. DOI: 10.1038/s41467-018-03083-5.

[54] Yi Sun, Haohua Tu, Sixian You, Chi Zhang, Yuan-Zhi Liu, and Stephen A Boppart. “Detection of weak near-infrared optical imaging signals under ambient light by optical parametric amplification”. In: *Optics letters* 44.17 (2019), pp. 4391–4394.

[55] Takumi Suzuki, Takaya Hoshi, Akito Kawasaki, Shotaro Oki, Konhi Ichii, Hironari Nagayoshi, Kazuma Takahashi, Takahiro Kashiwazaki, Taichi Yamashima, Asuka Inoue, Takeshi Umeki, Tatsuki Sonoyama, Kan Takase, Warit Asavanant, Mamoru Endo, and Akira Furusawa. *Ultrafast all-optical quantum teleportation*. Apr. 16, 2026. DOI: `10.48550/arXiv.2604.14959`. arXiv: `2604.14959[quant-ph]`.

[56] Demid V Sychev, Alexander E Ulanov, Anastasia A Pushkina, Matthew W Richards, Ilya A Fedorov, and Alexander I Lvovsky. “Enlargement of optical Schrödinger’s cat states”. In: *Nature Photonics* 11.6 (2017), pp. 379–382.

[57] Naoto Takanashi, Asuka Inoue, Takahiro Kashiwazaki, Takushi Kazama, Koji Enbutsu, Ryoichi Kasahara, Takeshi Umeki, and Akira Furusawa. “All-optical phase-sensitive detection for ultra-fast quantum computation”. In: *Optics Express* 28.23 (2020), pp. 34916–34926.

[58] Kan Takase, Jun-ichi Yoshikawa, Warit Asavanant, Mamoru Endo, and Akira Furusawa. “Generation of optical Schrödinger cat states by generalized photon subtraction”. In: *Physical Review A* 103.1 (2021), p. 013710.

[59] Lars Thylén and Lech Wosinski. “Integrated photonics in the 21st century”. In: *Photonics Research* 2.2 (2014), pp. 75–81.

[60] Alfred B U’Ren, Christine Silberhorn, Reinhard Erdmann, Konrad Banaszek, Warren P Grice, Ian A Walmsley, and Michael G Raymer. “Generation of pure-state single-photon wavepackets by conditional preparation based on spontaneous parametric downconversion”. In: *arXiv preprint quant-ph/0611019* (2006).

[61] Wojciech Wasilewski, A. I. Lvovsky, Konrad Banaszek, and Czesław Radzewicz. “Pulsed squeezed light: Simultaneous squeezing of multiple modes”. In: *Physical Review A* 73.6 (June 20, 2006), p. 063819. DOI: `10.1103/PhysRevA.73.063819`.

[62] Rebecca Whittaker, Chris Erven, Alex Neville, Monica Berry, JL O’Brien, Hugo Cable, and JCF Matthews. “Absorption spectroscopy at the ultimate quantum limit from single-photon states”. In: *New Journal of Physics* 19.2 (2017), p. 023013.

[63] James Williams, Rajveer Nehra, **Sendonaris, Elina**, Luis Ledezma, Robert M. Gray, Ryoto Sekine, and Alireza Marandi. “Ultrashort pulse biphoton source in lithium niobate nanophotonics at 2 μm”. In: *Nanophotonics* 13.18 (Aug. 1, 2024), pp. 3535–3544. DOI: `10.1515/nanoph-2024-0054`.

[64] Taichi Yamashima, Takahiro Kashiwazaki, Takumi Suzuki, Rajveer Nehra, Tomohiro Nakamura, Asuka Inoue, Takeshi Umeki, Kan Takase, Warit Asavanant, Mamoru Endo, et al. “All-optical measurement-device-free feedforward enabling ultra-fast quantum information processing”. In: *arXiv preprint arXiv:2410.20693* (2024).

[65] Jun-ichi Yoshikawa, Warit Asavanant, and Akira Furusawa. "Purification of photon subtraction from continuous squeezed light by filtering". In: *Physical Review A* 96.5 (2017), p. 052304.

[66] Han-Sen Zhong, Hui Wang, Yu-Hao Deng, Ming-Cheng Chen, Li-Chao Peng, Yi-Han Luo, Jian Qin, Dian Wu, Xing Ding, Yi Hu, Peng Hu, Xiao-Yan Yang, Wei-Jun Zhang, Hao Li, Yuxuan Li, Xiao Jiang, Lin Gan, Guangwen Yang, Lixing You, Zhen Wang, Li Li, Nai-Le Liu, Chao-Yang Lu, and Jian-Wei Pan. "Quantum computational advantage using photons". In: *Science* 370.6523 (Dec. 18, 2020), pp. 1460–1463. DOI: 10.1126/science.abe8770.

Chapter 5

FREQUENCY RESOLVED OPTICAL GATING USING PARAMETRIC AMPLIFICATION FOR CHARACTERIZING ULTRAFAST TEMPORALLY MULTIMODE SQUEEZED STATES

[1] Elina Sendonaris, Thomas Zacharias, Robert Gray, James Williams, and Alireza Marandi. *Frequency resolved optical gating using parametric amplification for characterizing ultrafast temporally multimode squeezed states*. Apr. 9, 2026. DOI: 10.48550/arXiv.2604.08717. arXiv: 2604.08717[quant-ph].

ABSTRACT

Temporally multimode squeezed states have been a topic of recent interest due to their applications in quantum communication, information processing, and sensing. Characterizing the mode shapes is crucial for effectively manipulating these states, but current mode shape and state characterization techniques necessitate constraining assumptions and complicated experimental setups. Here, we propose a characterization technique that simultaneously recovers the complex temporal mode shapes and quadrature variances of ultrafast multimode squeezed states based on frequency-resolved optical gating (FROG) using an optical parametric amplifier (OPA). FROG is a promising tool for quantum state characterization due to its flexibility of implementation and high temporal resolution. Using an OPA as the nonlinear process in FROG has the benefit of amplifying weak quantum states to a detectable level while preserving quantum information. Numerical simulations demonstrate the recovery of the mode shapes and levels of squeezing and anti-squeezing of ultrafast multimode squeezed states. This scheme offers a practical experimental approach to measuring arbitrary temporal mode shapes and characterizing large-scale multimode ultrafast Gaussian quantum states.

5.1 Introduction

Optical quantum information processing and communication have been the subjects of intense study, due to light's long coherence time and information density capacity [1, 15, 16, 24, 25, 48]. Encoding quantum information in the temporal modes of ultrashort pulses, which are overlapping orthonormal modes in time and frequency, allows for multiple modes to exist within the same pulse and spatial mode [4]. This basis allows a single pulse to carry a large amount of information, making it an attractive and natural option for ultrafast time-multiplexed communication and computation [32]. High-bandwidth single-mode pulses also carry a large amount of information, and recent progress has seen quantum optics extended even to the attosecond regime [6, 38, 39].

One difficulty of working with ultrafast quantum states is that the efficiency of operations degrades rapidly with the mismatch between modes, so characterizing the mode shapes of the quantum state is paramount to manipulating these states and realizing useful computation and communication. Using squeezed states to perform continuous-variable quantum computation [20, 21] and secure quantum communication [18, 27] is one path to quantum advantage which has the benefit of deterministic state generation. Characterizing ultrafast quantum states has therefore been an active field of study.

In particular, the tomography of temporally multimode squeezed states using optical parametric amplifiers (OPAs) has been the subject of intense recent study [2, 13, 42]. OPAs are well-suited to generating and measuring these states due to their inherently multimode [41] and broadband nature [34], and their phase-sensitive amplification which allows for quadrature-selective measurement while preserving some quantum information [12, 22]. Because of their broad bandwidth [17], many temporal modes can exist in an ultrashort multimode squeezed pulse generated by an OPA. Mode-selective squeezing measurements allow us to access the squeezing in the principal modes, which is higher than the mode-averaged (e.g. time-averaged) squeezing which is typically measured [2, 23, 42].

One challenge in temporal-mode continuous-variable (CV) quantum optics is that the relevant basis is typically unknown, as the principal squeezing modes depend on pump shape and phase matching and are sensitive to physical imperfections. Most detection strategies require mode-matched local oscillators [5] or reconfigurable mode projections [14, 26]. Some techniques have a tradeoff between the amount of information gained about the state and the modes [36], and others rely on prior knowledge about the state [9, 35]. Quantum pulse gates can decompose the state into multiple modes by shaping a pump pulse [30, 33] and have been used to decompose a state into its component modes adaptively [9, 31]. Electro-optic sampling has also been used to characterize the temporal nature of squeezed light [10, 11, 28, 43], but it necessitates sub-cycle pulses, which limits it to quantum pulses with longer wavelengths. Lastly, decomposition of data measured using homodyne detection [5, 29] can also be used to identify the principal modes of a state. Many of these techniques require pulse shaping and feedback loops, and their resolution and bandwidth is typically limited by pulse shaping performance. However, a technique capable of directly reconstructing both the temporal mode structure and quantum statistics of ultrafast multimode squeezed states without requiring mode-matched local oscillators or adaptive pulse shaping remains a significant challenge.

Here we introduce multimode Gaussian OPA frequency-resolved optical gating (MMG-OPA-FROG), a phase-sensitive parametric variant of FROG in which a broadband OPA serves as the nonlinear gate, and show how it can be used to characterize Gaussian states through their quadrature variances and simultaneously determine their principal temporal mode basis. We propose and numerically simulate using an OPA as the nonlinear element in a frequency-resolved optical gating (FROG) setup [37] and develop a retrieval algorithm to account for the multimode and quantum nature of the input state. The concept is illustrated in Fig. 5.1.

FROG is popular due to its simplicity of setup and robustness to experimental imperfections while having high resolution and bandwidth. Employing an OPA as the nonlinear process in FROG has been used to measure pulses with extremely low energy [44, 46, 47], which is possible because OPAs can amplify pulses by a factor of as large as 10^8 while having low dispersion. Furthermore, the complex temporal envelope of quantum correlations between twin beams has been measured using FROG [7]. Thus, an OPA-based FROG is an ideal candidate for characterizing low-photon-number ultrashort quantum states. The phase-sensitive nature of the OPA provides access to the second-order moments, from which it is possible to fully characterize Gaussian states and even partially characterize non-Gaussian states. This technique gives the full temporal mode information, including the complex mode phase, which is crucial for manipulating the modes. MMG-OPA-FROG can be applied even for single-mode ultrafast quantum states, in order to take advantage of the high resolution and flexibility in wavelength. We have recently explored multimode squeezed state reconstruction using sum-frequency generation FROG [45]. The present work instead considers the distinct measurement regime of OPA-only FROG and develops the corresponding formalism for recovering the temporal modes and

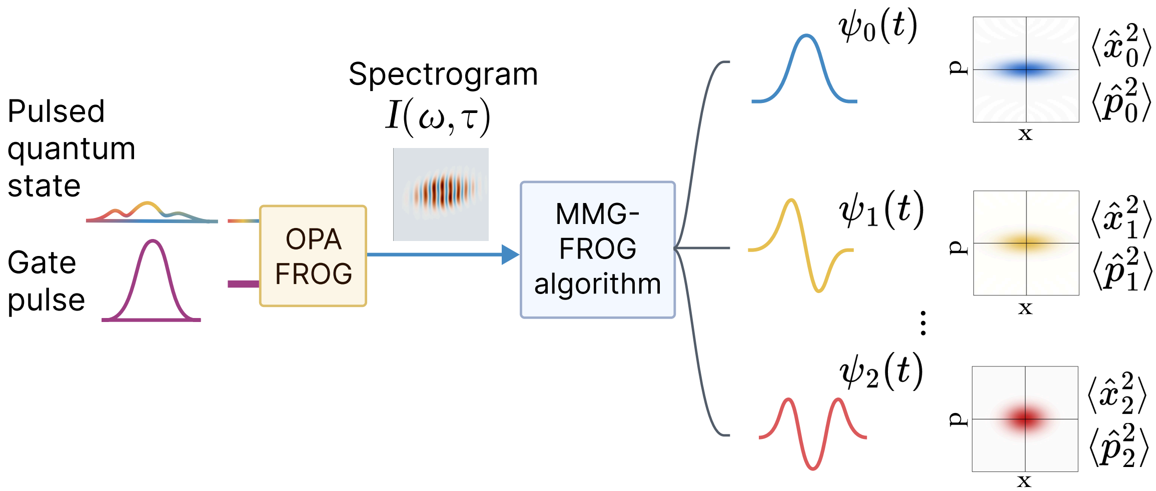

Figure 5.1: Temporally multimode Gaussian (MMG) state reconstruction process using OPA FROG. The pulsed quantum input state and a gate pulse are put through an OPA FROG setup, and the resulting spectrogram is put into the MMG-OPA-FROG algorithm, which splits the input state up into its component modes $\psi_n(t)$ and second-order moments $\langle \hat{x}_n^2 \rangle$ and $\langle \hat{p}_n^2 \rangle$.

second-order quadrature moments.

We show how the FROG spectrogram is related to the mode shapes and second-order moments and then show numerically how ultrafast multimode Gaussian states can be characterized using a FROG retrieval algorithm. In addition, we quantify the resiliency to noise in the spectrogram, showing a successful retrieval even in the presence of noise, and how to extract the relative squeezing angles from the mode shapes. We show how to extract information necessary for temporal mode quantum information processing and communication using a minimal experimental setup and few assumptions.

5.2 Theory

Quantum OPA FROG with arbitrary OPA and signal modes

We start by considering a frequency-resolved optical gating (FROG) setup with an OPA as its nonlinearity. The MMG-OPA-FROG spectrogram is generated by sending the quantum state and gating pulse as the pump into an OPA and measuring the output spectra at various relative delays between the input state and gate. The information in the spectrogram allows for the reconstruction of the complex mode shape of a classical pulse, and it also allows for reconstruction of multiple modes in the same pulse. This spectrogram $I(\omega, \tau)$ is the expectation value of the photon number of the output state at delay τ and frequency ω:

$$I(\omega, \tau) = \langle \hat{N}(\omega, \tau) \rangle = \langle \hat{a}^{out,\dagger}(\omega, \tau) \hat{a}^{out}(\omega, \tau) \rangle. \tag{5.1}$$

where I is spectrogram and $\hat{a}^{out}(\omega, \tau)$ is annihilation operator in the Heisenberg picture after the OPA in the frequency mode ω at gate delay τ. Expanding the output operator in terms of the temporal modes of the OPA and then in terms of the operators of the signal input into the OPA $\hat{a}^{in}$, using the Bogoliubov transform, we have

$$\hat{a}^{out}(\omega) = \sum_m \psi_m^{\mathrm{OPA}*}(\omega, \tau) \hat{a}_m^{out} \tag{5.2}$$

$$= \sum_m \psi_m^{\mathrm{OPA}*}(\omega, \tau) (\cosh r_m(\tau) \hat{a}_m^{in} - \sinh r_m(\tau) e^{i\theta_m(\tau)} \hat{a}_m^{in\dagger}) \tag{5.3}$$

where $\xi_n \equiv r_n e^{i\theta_m}$ are the complex gain parameters of the OPA for each mode m and $\psi_m^{\mathrm{OPA}}(\omega)$ are the OPA modes in the frequency basis. The modes are delay-dependent since their position in time is dependent on the relative position of the pump pulse to the signal pulse, and the gain parameters are delay-dependent because the pump phase determines which signal quadrature is amplified. The mode annihilation operators in a basis $\{\psi_m(\omega)\}$ are defined as

$$\hat{a}_m = \int \mathrm{d}\omega \ \psi_m(\omega) \hat{a}(\omega), \tag{5.4}$$

which, for an orthonormal basis leads to the complementary transformation

$$\hat{a}(\omega) = \sum_m \psi_m^*(\omega) \hat{a}_m. \tag{5.5}$$

We can expand the spectrogram in terms of sums over the OPA modes, suppressing the delay dependence of the modes and gain parameters for now:

$$I(\omega, \tau) = \sum_{m,m'} \Big\langle \psi_m^{\mathrm{OPA}}(\omega) (\cosh r_m \hat{a}_m^{in\dagger} - \sinh r_m e^{-i\theta_m} \hat{a}_m^{in}) \\ \psi_{m'}^{\mathrm{OPA}*}(\omega) (\cosh r_{m'} \hat{a}_{m'}^{in} - \sinh r_{m'} e^{i\theta_{m'}} \hat{a}_{m'}^{in\dagger}) \Big\rangle. \tag{5.6}$$

We now define how we would like to decompose the multimode Gaussian input state. Any Gaussian state can be decomposed into a principal mode basis in which the states are uncorrelated with each other [8]. The input state's annihilation operator can be decomposed into its uncorrelated principal mode basis $\{\psi_n^{sig}(\omega)\}$ and the output signal can be written as a function of that basis as (subscript n denotes an operator the signal basis while m indicates one in the OPA basis):

$$\hat{a}_m^{in} = \int \mathrm{d}\omega\ \psi_m^{\mathrm{OPA}}(\omega)\hat{a}^{in}(\omega) \tag{5.7}$$

$$= \int \mathrm{d}\omega\ \psi_m^{\mathrm{OPA}}(\omega)\sum_n \psi_n^{sig*}(\omega)\hat{a}_n^{in} \tag{5.8}$$

$$= \sum_n \sigma_{mn}\hat{a}_n^{in} \tag{5.9}$$

where $\sigma_{mn} \equiv \int \mathrm{d}\omega\ \psi_m^{\mathrm{OPA}}(\omega)\psi_n^{sig*}(\omega)$ is the overlap of a signal and OPA mode.

Now, we make the high-gain approximation, which is that the detected modes have high gain parameters r_m such that $\cosh r_m \approx \sinh r_m \approx \exp(r_m)/2$. This approximation is relevant when using a photodetector which is not sensitive to single photons, or rather, one which is used to detect mainly classical macroscopic states. With this approximation and plugging in the definition for σ_{mn} we have:

$$I(\omega,\tau) = \sum_{m,m',n,n'} \Big\langle \psi_m^{\mathrm{OPA}}(\omega)\psi_{m'}^{\mathrm{OPA}*}(\omega)\frac{e^{r_m+r'_m}}{4}(\sigma_{mn}^*\hat{a}_n^{in\dagger} - e^{-i\theta_m}\sigma_{mn}\hat{a}_n^{in})$$
$$(\sigma_{m'n'}\hat{a}_{n'}^{in} - e^{i\theta_{m'}}\sigma_{m'n'}^*\hat{a}_{n'}^{in\dagger})\Big\rangle. \tag{5.10}$$

The sums over n, n' are over all modes of the input state (that is, from the first mode to a potential infinite number of modes), and the terms are not necessarily zero when the input state is vacuum, but rather only zero when the overlap between the OPA and input modes is zero. This is due to an $\langle \hat{a}^{in\dagger}\hat{a}^{in}\rangle$ term which is non-zero for vacuum.

Using that the signal modes are uncorrelated, that is, that $\langle \hat{q}_n\hat{q}'_{n'}\rangle \propto \delta_{nn'}$ for $\hat{q}, \hat{q}' \in \{\hat{a}^{in}, \hat{a}^{in\dagger}\}$, we arrive at

$$I(\omega,\tau) = \sum_{m,m',n} \psi_m^{\mathrm{OPA}}(\omega,\tau)\psi_{m'}^{\mathrm{OPA}*}(\omega,\tau)\frac{e^{r_m+r_{m'}}}{4}\Big(\sigma_{mn}^*\sigma_{m'n}\langle\hat{a}_n^{in\dagger}\hat{a}_n^{in}\rangle - e^{-i\theta_m}\sigma_{mn}\sigma_{m'n}\langle(\hat{a}_n^{in})^2\rangle$$
$$- e^{i\theta_{m'}}\sigma_{mn}^*\sigma_{m'n}^*\langle(\hat{a}_n^{in\dagger})^2\rangle + e^{i(\theta_{m'}-\theta_m)}\sigma_{mn}\sigma_{m'n}^*\langle\hat{a}_n^{in}\hat{a}_n^{in\dagger}\rangle\Big). \tag{5.11}$$

This shows that we need to know the overlap between the modes of the OPA and the input state in order to interpret the results. This indicates that the spectrogram contains all second-order moments of the state, which fully characterize a zero-mean-field Gaussian state.

Quantum OPA FROG with a large-bandwidth OPA

A large-bandwidth OPA has modes which approach delta functions in time and plane waves in frequency:

$$\psi_m^{\mathrm{OPA}}(\omega) \to \mathfrak{F}\{\delta(t_m)\} = e^{-i\omega t_m}. \tag{5.12}$$

This is because the temporal width of OPA modes is inversely proportional to the product of the bandwidths of the pump laser and of the phase matching of the OPA [19].

The mode overlap then becomes

$$\sigma_{mn} = \int \mathrm{d}\omega\ e^{-i\omega t_m}\psi_n^{sig*}(\omega) = \psi_n^{sig*}(t_m) \tag{5.13}$$

where $\psi^{sig}(t)_n$ are the inverse Fourier transforms of the signal modes. We now drop the m subscript and simply refer to the OPA modes by their time t. Plugging all this into Eq. 5.11 results in

$$\begin{aligned} I(\omega,\tau) = \iint \mathrm{d}t\mathrm{d}t' e^{i\omega(t'-t)}\frac{e^{r(t-\tau)+r(t'-\tau)}}{4}\sum_n \Big(\psi_n^{sig}(t)\psi_n^{sig*}(t')\langle\hat{a}_n^{in\dagger}\hat{a}_n^{in}\rangle - e^{-i\theta(t-\tau)}\psi_n^{sig*}(t)\psi_n^{sig*}(t')\langle(\hat{a}_n^{in})^2\rangle \\ - e^{i\theta(t'-\tau)}\psi_n^{sig}(t)\psi_n^{sig}(t')\langle(\hat{a}_n^{in\dagger})^2\rangle + e^{i(\theta(t'-\tau)-\theta(t'-\tau))}\psi_n^{sig*}(t)\psi_n^{sig}(t')\langle\hat{a}_n^{in}\hat{a}_n^{in\dagger}\rangle\Big). \end{aligned} \tag{5.14}$$

We now assume that the signal is centered around a frequency ω_s and that the pump is centered around a frequency $\omega_p = 2\omega_s$. The squeezing parameter $\xi(t)$ can be separated into

$$\xi(t) = r(t)e^{i\theta(t)} = r(t)e^{i(\delta\theta(t)+\omega_p t)} \tag{5.15}$$

with $\theta(t) = \delta\theta(t) + \omega_p t$.

We also define the broadband quadrature operators

$$\hat{x}_n = \frac{1}{2}(\hat{a}_n + \hat{a}_n^\dagger) \tag{5.16}$$

$$\hat{p}_n = \frac{1}{2i}(\hat{a}_n - \hat{a}_n^\dagger) \tag{5.17}$$

The spectrogram can be written in terms of the interaction picture squeezing phase and quadrature operators, dropping the superscripts *sig* and *in*, as

$$\begin{aligned} I(\omega,\tau) = \iint \mathrm{d}t\mathrm{d}t' \frac{e^{i\omega(t-t')+r(t-\tau)+r(t'-\tau)}}{4}\sum_n \Big[(\langle\hat{x}_n^2\rangle + \langle\hat{p}_n^2\rangle - \tfrac{1}{2})\psi_n(t)\psi_n^*(t') \\ + (\langle\hat{x}_n^2\rangle + \langle\hat{p}_n^2\rangle + \tfrac{1}{2})e^{-i(\delta\theta(t-\tau)-\delta\theta(t'-\tau))}\psi_n^*(t)\psi(t') \\ - (\langle\hat{x}_n^2\rangle - \langle\hat{p}_n^2\rangle + i\langle\hat{x}_n\hat{p}_n + \hat{p}_n\hat{x}_n\rangle)e^{-i(\delta\theta(t-\tau)+\omega_p\tau)}\psi_n^*(t)\psi_n^*(t') \\ - (\langle\hat{x}_n^2\rangle - \langle\hat{p}_n^2\rangle - i\langle\hat{x}_n\hat{p}_n + \hat{p}_n\hat{x}_n\rangle)e^{i(\delta\theta(t'-\tau)+\omega_p\tau)}\psi_n(t)\psi_n(t')\Big]. \end{aligned} \tag{5.18}$$

Moving a factor of $e^{i(-\delta\theta(t-\tau)+\delta\theta(t'-\tau))/2}$ in front, we have

$$
\begin{aligned}
I(\omega,\tau) = \iint \mathrm{d}t\mathrm{d}t' \; &\tfrac{1}{4}e^{i(\omega(t'-t)-\delta\theta(t-\tau)/2+\delta\theta(t'-\tau)/2)+r(t-\tau)+r(t'-\tau)} \\
&\sum_n \Big[(\langle \hat{x}_n^2\rangle + \langle \hat{p}_n^2\rangle - \tfrac{1}{2})e^{i(\delta\theta(t-\tau)-\delta\theta(t'-\tau))/2}\psi_n(t)\psi_n^*(t') \\
&+ (\langle \hat{x}_n^2\rangle + \langle \hat{p}_n^2\rangle + \tfrac{1}{2})e^{-i(\delta\theta(t-\tau)-\delta\theta(t'-\tau))/2}\psi_n^*(t)\psi(t') \\
&- (\langle \hat{x}_n^2\rangle - \langle \hat{p}_n^2\rangle + i\langle \hat{x}_n\hat{p}_n + \hat{p}_n\hat{x}_n\rangle)e^{i((-\delta\theta(t-\tau)-\delta\theta(t'-\tau))/2-\omega_p\tau)}\psi_n^*(t)\psi_n^*(t') \\
&- (\langle \hat{x}_n^2\rangle - \langle \hat{p}_n^2\rangle - i\langle \hat{x}_n\hat{p}_n + \hat{p}_n\hat{x}_n\rangle)e^{i((\delta\theta(t-\tau)+\delta\theta(t'-\tau))/2+\omega_p\tau)}\psi_n(t)\psi_n(t')\Big].
\end{aligned} \tag{5.19}
$$

Collecting the second-order moments and defining $\delta\phi(t) = \theta(t)/2 - \omega_s t$, we get

$$
\begin{aligned}
I(\omega,\tau) = \sum_n \iint \mathrm{d}t\mathrm{d}t' &\tfrac{1}{4}e^{i(\omega(t'-t)-\delta\phi(t-\tau)+\delta\phi(t'-\tau))+r(t-\tau)+r(t'-\tau)} \\
\Big[\langle \hat{x}_n^2\rangle &(\psi_n(t)e^{i(\delta\phi(t-\tau)+\omega_p\tau/2)} - \psi_n^*(t)e^{-i(\delta\phi(t-\tau)+\omega_p\tau/2)})(\psi_n^*(t')e^{-i(\delta\phi(t'-\tau)+\omega_p\tau/2)} - \psi_n(t')e^{i(\delta\phi(t'-\tau)+\omega_p\tau/2)}) \\
+\langle \hat{p}_n^2\rangle &(\psi_n(t)e^{i(\delta\phi(t-\tau)+\omega_p\tau/2)} + \psi_n^*(t)e^{-i(\delta\phi(t-\tau)+\omega_p\tau/2)})(\psi_n^*(t')e^{-i(\delta\phi(t'-\tau)+\omega_p\tau/2)} + \psi_n(t')e^{i(\delta\phi(t'-\tau)+\omega_p\tau/2)}) \\
&+ \tfrac{1}{2}(\psi_n^*(t)\psi_n(t')e^{-i(\delta\phi(t-\tau)-\delta\phi(t'-\tau))} - \psi_n(t)\psi_n^*(t')e^{i(\delta\phi(t-\tau)-\delta\phi(t'-\tau))}) \\
+i\langle \hat{x}_n\hat{p}_n + \hat{p}_n\hat{x}_n\rangle &(\psi_n^*(t)\psi_n^*(t')e^{-i(\delta\phi(t-\tau)+\delta\phi(t'-\tau)+\omega_p\tau)} - \psi_n(t)\psi_n(t')e^{i(\delta\phi(t-\tau)+\delta\phi(t'-\tau)+\omega_p\tau)})\Big].
\end{aligned} \tag{5.20}
$$

Finally, simplifying each term and using the definition $G(t) \equiv e^{-i\delta\phi(t)+r(t)}$, we have

$$
\begin{aligned}
I(\omega,\tau) = \sum_{n=1}^{\infty} \Big[&\langle(\hat{x}_n^{\mathrm{in}})^2\rangle \Big|\mathfrak{F}\{G(t-\tau)\,\mathrm{Im}[\psi_n(t)e^{i(\delta\phi(t-\tau)+\omega_s\tau)}]\}\Big|^2 \\
&+ \langle(\hat{p}_n^{\mathrm{in}})^2\rangle \Big|\mathfrak{F}\{G(t-\tau)\,\mathrm{Re}[\psi_n(t)e^{i(\delta\phi(t-\tau)+\omega_s\tau)}]\}\Big|^2 \\
+\frac{1}{2}\langle \hat{x}_n^{\mathrm{in}}\hat{p}_n^{\mathrm{in}} + \hat{p}_n^{\mathrm{in}}\hat{x}_n^{\mathrm{in}}\rangle\,&\mathrm{Im}\Big[\mathfrak{F}\{G(t-\tau)\psi_n(t)e^{i(\delta\phi(t-\tau)-\omega_s\tau)}\}(\mathfrak{F}\{G^*(t-\tau)\psi_n^*(t)e^{-i(\delta\phi(t-\tau)+\omega_s\tau)}\})^*\Big] \\
&+ \frac{1}{8}\Big(\Big|\mathfrak{F}\{G(t-\tau)e^{-i\delta\phi(t-\tau)}\psi_n^*(t)\}\Big|^2 + \Big|\mathfrak{F}\{G(t-\tau)e^{i\delta\phi(t-\tau)}\psi_n(t)\}\Big|^2\Big)\Big].
\end{aligned} \tag{5.21}
$$

This form of the spectrogram is specific to bases in which the states in the modes are uncorrelated, so finding the modes which contribute in this way to the spectrogram will give us the principal modes, effectively diagonalizing the covariance matrix. The spectrogram is the incoherent sum of the principal-mode spectrograms, with four terms per mode. Two of the terms are weighted by the two non-zero second-order moments, and the last two are independent of the state's statistics. The angle in quadrature phase space along which the state is squeezed is encoded in the relative phase between the modes, allowing us to recover the covariance of the squeezed state. Thus, this spectrogram contains all the information needed to recover the mode shapes and the second-order moments of a multimode state, which is enough for characterizing a multimode Gaussian state.

It is important to note that the sum is over an infinite number of modes, since the vacuum modes result in a non-zero contribution to the spectrogram due to OPG. Thus, even for a vacuum input, the output spectrogram will be non-zero, and it is beneficial to subtract the vacuum contributions for ease of recovery.

Covariance term

The term following the covariance $\langle \hat{x}_n^{\text{in}} \hat{p}_n^{\text{in}} + \hat{p}_n^{\text{in}} \hat{x}_n^{\text{in}} \rangle$ is not in an ideal form for using a FROG-type algorithm. However, for a Gaussian state with zero mean-field (e.g. a squeezed state), the state can be rotated such that the covariance goes to zero by adding a phase to the mode shapes. This occurs because the covariance vanishes when the state is squeezed along the $\hat{x}$ or $\hat{p}$ axis. Therefore, we may set this covariance to zero without discarding physical information. The squeezing angle is not lost, but instead is absorbed into the complex phases of the recovered mode functions.

This equivalence follows from the broadband input state annihilation operator

$$\hat{a}(t) = \sum_n \psi_n^*(t) \hat{a}_n \tag{5.22}$$

and noting that multiplying either $\psi_n(t)$ or $\hat{a}_n$ by a complex phase $e^{-i\theta_n}$ can be compensated by multiplying the other one by the same complex phase. Making the transformation $\hat{a} \to e^{-i\theta} \hat{a}$ leads to the usual rotation in phase space $\hat{x} \to \hat{x}\cos\theta + \hat{p}\sin\theta$ and $\hat{p} \to \hat{p}\cos\theta - \hat{x}\sin\theta$. Hence rotating in quadrature phase space is operationally the same as adjusting the complex phase of the mode function. We can use this freedom to choose a basis with $\langle \hat{x}_n^{\text{in}} \hat{p}_n^{\text{in}} + \hat{p}_n^{\text{in}} \hat{x}_n^{\text{in}} \rangle = 0$, while keeping the squeezing orientation encoded in the retrieved mode phases.

As an example, we show three spectrograms in Fig. 5.2, each with just one mode. We show how rotating the quadrature operators and the modes leads to the spectrogram changing. Rotating the quadrature by $\pi/4$ shifts the peaks and valleys by half a period, as can be seen in Fig. 5.2(b), while adding the same phase to the modes shifts it back to the original spectrogram, as can be seen in Fig. 5.2(c). Thus, adding a phase to the operators and the modes leads to the same effect and one can be used to absorb the effect of the other, allowing us to ignore the covariance term for squeezed states. Moving forward we will omit this term in the equations of spectrograms.

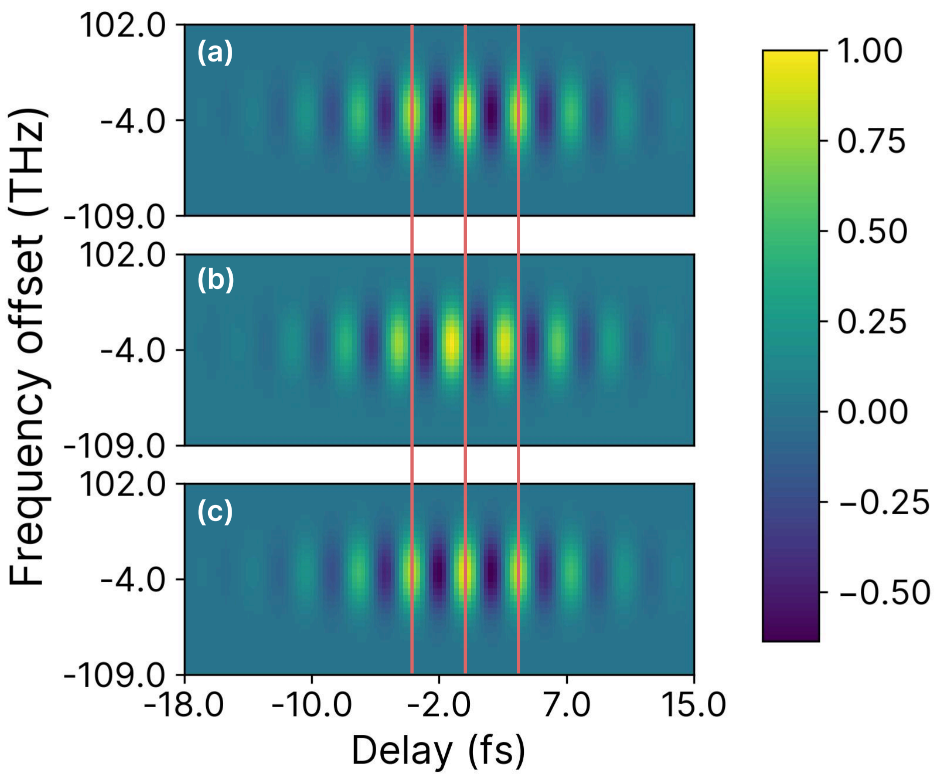

Figure 5.2: Spectrograms changing with rotating quadratures and adding a phase to the mode. All spectrograms are vacuum-subtracted and generated with one 30-fs Gaussian mode a 100-fs pump pulse, both with no chirp, and normalized such that their peak value is 1. The red lines are aligned to the peaks of (a) as a visual guide. (a) Spectrogram with no rotations. (b) Spectrogram with the quadratures rotated ($\hat{a} \rightarrow \hat{a}e^{-i\pi/4}$). (c) Spectrogram with the quadratures rotated and a phase on the mode ($\psi(t) \rightarrow \psi(t)e^{-i\pi/4}$). Note that this action undoes the quadrature rotation and that this spectrogram is identical to (a).

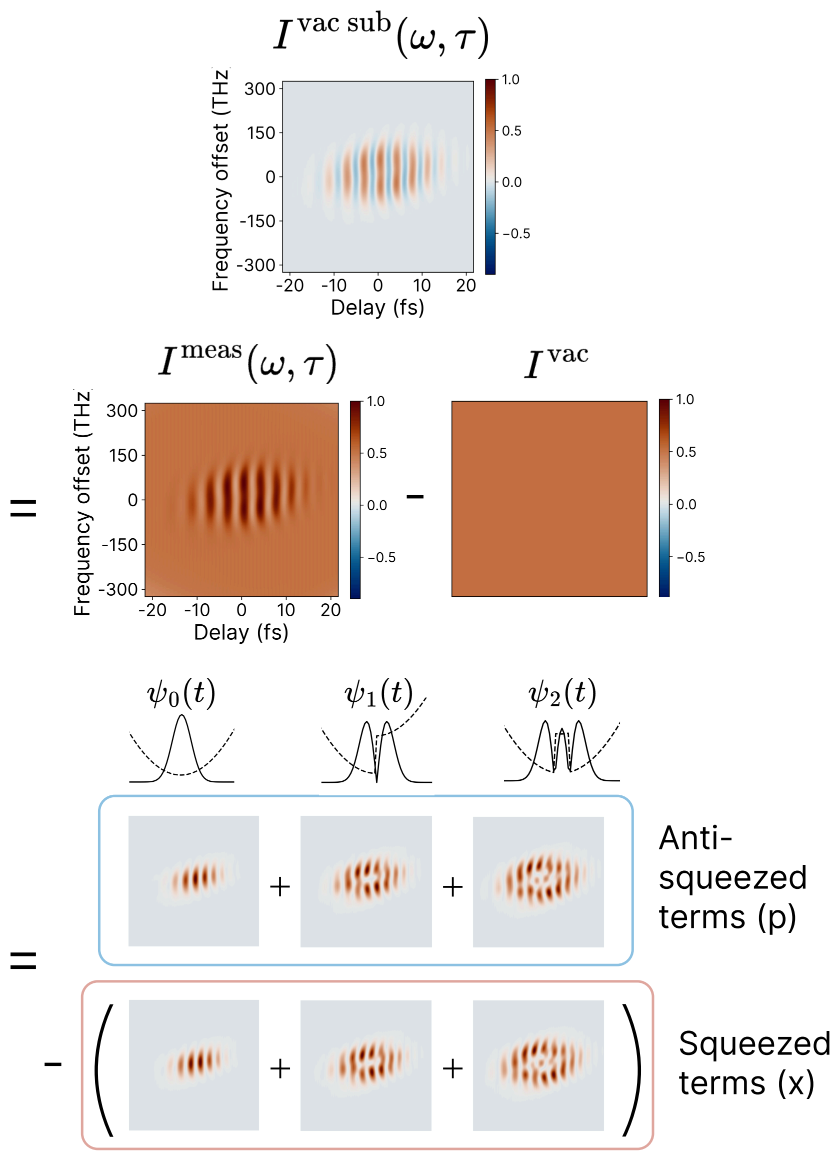

Figure 5.3: Overview of the vacuum-subtracted spectrogram $I^{\text{vac sub}}(\omega,\tau)$, which is the measured spectrogram $I^{\text{meas}}(\omega,\tau)$ minus the vacuum spectrogram I^{vac}, which is the output when the input state is vacuum. All color bars are shared and are normalized to the maximum of the measured spectrogram. For multimode squeezed states, the vacuum-subtracted spectrogram is composed of positive elements for the anti-squeezed quadratures and negative elements corresponding to the squeezed quadratures, with two terms per mode (one positive and one negative). Negative values indicate the presence of squeezing.

Vacuum-subtracted spectogram

For the case of a vacuum input, the spectrogram simplifies to the constant $I^{\text{vac}}(\omega, \tau) = |\int \mathrm{d}t\, G(t)|^2/4$, which is just the optical parametric generation from the OPA. Because the spectrogram is non-zero for vacuum input, it is possible to extract the absolute squeezing parameters by normalizing the extracted mode shapes using the vacuum spectrogram as a reference. Furthermore, if the vacuum spectrogram is subtracted from a measured spectrogram, the last two terms and all contributions from un-squeezed modes in the input state are canceled out, truncating the sum to only those modes which are occupied by a non-vacuum state:

$$\begin{aligned} I^{\text{vac sub}}(\omega, \tau) &\equiv I(\omega, \tau) - I^{\text{vac}}(\omega, \tau) \\ &= \sum_{n=1}^{M} \Bigg[\left(\left\langle (\hat{x}_n^{\text{in}})^2 \right\rangle - \frac{1}{4} \right) \left| \mathfrak{F}\{G(t') \operatorname{Im}[\psi_n(t) e^{i(\delta\phi(t') + \omega_s \tau)}]\} \right|^2 \\ &\qquad + \left(\left\langle (\hat{p}_n^{\text{in}})^2 \right\rangle - \frac{1}{4} \right) \left| \mathfrak{F}\{G(t') \operatorname{Re}[\psi_n(t) e^{i(\delta\phi(t') + \omega_s \tau)}]\} \right|^2 \Bigg], \end{aligned} \tag{5.23}$$

where M is the number of non-vacuum modes

This spectrogram, which we call the vacuum-subtracted spectrogram, has negative components if either quadrature has noise below the shot noise level. The negativity of the vacuum-subtracted spectrogram thus gives an indication of whether there is squeezing. An example vacuum-subtracted spectrogram for a multimode squeezed state is shown in Fig. 5.3 using 25-fs Hermite-Gaussian modes with a moderate chirp and a 100-fs chirped gating pulse. The modes have 3 dB, 4 dB, and 2 dB of squeezing, in order of increasing Hermite polynomial order.

5.3 Algorithm

We use a similar algorithm to that developed in [3], which was for a varying probabilistic pulse train, whose spectrogram is also an incoherent sum over the potential pulses that can be emitted. Whereas their spectrogram was positive, our vacuum-subtracted spectrogram can contain negative values, so their data constraint cannot be applied directly. We use Lagrange multiplier projection to get around this issue. Furthermore, the form of the spectrogram terms is not amenable to the principal-components generalized projections algorithm, so we must use gradient descent for the nonlinear constraint step. A block diagram is shown in Fig. 5.4.

Throughout the algorithm, as is common in FROG algorithms, we keep track of both the mode shapes (and the corresponding weights, which are based on the second-order

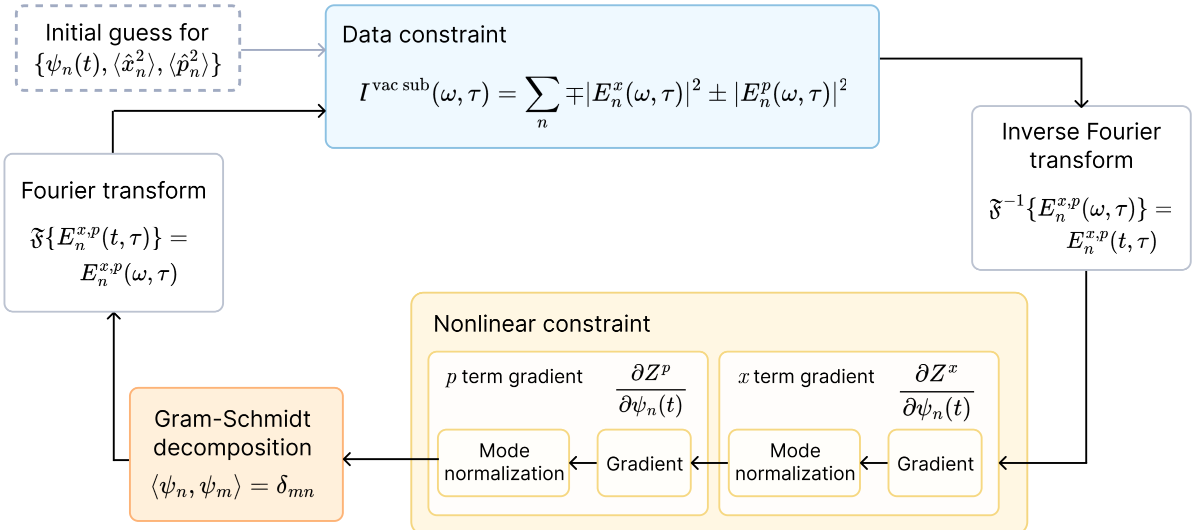

Figure 5.4: Block diagram of the MMG OPA FROG algorithm. The data constraint uses the measured data to update the guess in frequency space. The nonlinear constraint enforces the form of the spectrogram based on the nonlinear action of the OPA, which is encoded in Eq. 5.21. The mode orthonormalization step ensures the validity of the modes. An initial (usually random) guess for the shapes and quadrature variances of the modes begins the algorithm.

moments) and the frequency-domain complex signal fields [37]. The aim of each iteration of the algorithm is to update the signal fields so that they match the measured data and then to update the modes and weights so that they match the signal fields. In the case of MMG-FROG, we must keep track of $2M$ signal fields for M modes, where for each mode there is an x and a p field corresponding to their respective term in the vacuum-subtracted spectrogram. We label these signal fields $E_n^{x,p}(\omega,\tau)$.

Data constraint

The spectrogram is in the form of

$$I^{\text{vac sub}}(\omega,\tau) = \sum_{n=1}^{N} \pm |E_n^x(\omega,\tau)|^2 \pm |E_n^p(\omega,\tau)|^2 = \sum_{m=1}^{2N} s_m |E_m(\omega,\tau)|^2 \tag{5.24}$$

with the signs in front of the fields $s_m \in \pm 1$ depending on whether each quadrature is squeezed or anti-squeezed, m denotes a sum over both x and p terms (e.g. the first N terms for x and $m = N+1$ through $2N$ correspond to the p terms), and E_m without a superscript denotes that the field can be of either quadrature. The goal of the data constraint step is to change the signal fields as little as possible while satisfying the equation above. This can be done by the method of Lagrangian multipliers.

We define a Lagrangian to be minimized

$$\mathcal{L} = \sum_m |E_m(\omega,\tau) - E'_m(\omega,\tau)|^2 + \lambda(\omega,\tau)\left(\sum_{m'} s_m |E'_m(\omega,\tau)|^2 - I^{\text{vac sub}}(\omega,\tau)\right), \quad (5.25)$$

with $E'_n(\omega,\tau)$ being the updated signal fields. Taking the derivative with respect to E'^*_n, we have that

$$E'_m(\omega,\tau) = \frac{E_m(\omega,\tau)}{1 + s_m\lambda(\omega,\tau)}. \quad (5.26)$$

This equation represents N^2 equations, one for each point in the spectrogram. To determine the value of $\lambda(\omega,\tau)$, we plug this equation into the data constraint Eq. 5.24:

$$\sum_m s_m \frac{|E_m(\omega,\tau)|^2}{(1 + s_m\lambda(\omega,\tau))^2} = I^{\text{vac sub}}(\omega,\tau). \quad (5.27)$$

After solving for $\lambda(\omega,\tau)$, we simply plug it into Eq. 5.26 and obtain the new signal.

Nonlinear constraint

The nonlinear constraint serves to enforce the form of the signal fields. That is, that

$$E^x_n(t,\tau) = X_n G(t')(\mathrm{Re}[\psi_n(t)]\sin(\delta\phi(t') + \omega_s\tau) + \mathrm{Im}[\psi_n(t)]\cos(\delta\phi(t') + \omega_s\tau)) \quad (5.28)$$

$$E^p_n(t,\tau) = P_n G(t')(\mathrm{Re}[\psi_n(t)]\cos(\delta\phi(t') + \omega_s\tau) - \mathrm{Im}[\psi_n(t)]\sin(\delta\phi(t') + \omega_s\tau)) \quad (5.29)$$

where $X_n \equiv \sqrt{\left|\langle(\hat{x}^{\text{in}}_n)^2\rangle - \frac{1}{4}\right|}$, $P_n \equiv \sqrt{\left|\langle(\hat{p}^{\text{in}}_n)^2\rangle - \frac{1}{4}\right|}$, and $t' \equiv t - \tau$. These are the inverse Fourier transforms of $E^{x,p}_n(\omega,\tau)$ in the first parameter.

The way to enforce this constraint is to find the mode shape and variance that minimizes the functional loss

$$Z^{x,p}_n \equiv \sum_{t,\tau} |E^{x,p}_n(t,\tau) - E^{x,p\prime}_n(t,\tau)|^2, \quad (5.30)$$

where $E^{x,p\prime}_n(t,\tau)$ is a function of the mode shape and state as shown above in Eqns. 5.28 and 5.29. We can analytically find the gradient of the functional loss with respect to the real and imaginary parts of the modes:

$$\frac{\partial Z^x_n}{\partial\,\mathrm{Re}[\psi_n(t)]} = -2\sum_\tau \mathrm{Re}[X_n G(t-\tau)\sin\delta\phi'(t,\tau) R^{x*}_n(t,\tau)] \quad (5.31)$$

$$\frac{\partial Z^x_n}{\partial\,\mathrm{Im}[\psi_n(t)]} = -2\sum_\tau \mathrm{Re}[X_n G(t-\tau)\cos\delta\phi'(t,\tau) R^{x*}_n(t,\tau)] \quad (5.32)$$

$$\frac{\partial Z^p_n}{\partial\,\mathrm{Re}[\psi_n(t)]} = -2\sum_\tau \mathrm{Re}[P_n G(t-\tau)\cos\delta\phi'(t,\tau) R^{p*}_n(t,\tau)] \quad (5.33)$$

$$\frac{\partial Z^p_n}{\partial\,\mathrm{Im}[\psi_n(t)]} = 2\sum_\tau \mathrm{Re}[P_n G(t-\tau)\sin\delta\phi'(t,\tau) R^{p*}_n(t,\tau)], \quad (5.34)$$

where $G(t) \equiv e^{r(t)+i\delta\phi(t)}$, $\delta\phi'(t,\tau) \equiv \delta\phi(t-\tau) + \omega_s \tau$ and

$$R_n^x(t,\tau) \equiv E_n^x(t,\tau) - X_n G(t-\tau)(\mathrm{Re}[\psi_n(t)] \sin\delta\phi'(t,\tau) + \mathrm{Im}[\psi_n(t)] \cos\delta\phi'(t,\tau)) \quad (5.35)$$

$$R_n^p(t,\tau) \equiv E_n^p(t,\tau) - P_n G(t-\tau)(\mathrm{Re}[\psi_n(t)] \cos\delta\phi'(t,\tau) - \mathrm{Im}[\psi_n(t)] \sin\delta\phi'(t,\tau)) \quad (5.36)$$

are the residuals between the stored signal fields and the signal fields calculated from the modes and quadrature variances. After calculating these gradients, we use an optimizer to determine the optimal step size before updating the mode shapes along the gradient direction.

In order to update the mode variance weights, we normalize the new mode shapes such that $\sum_t |\psi_n(t)|^2 = 1$ for all n and multiply the variance weight by the amount we divided $\psi_n(t)$ by. That is,

$$\psi_n^{\mathrm{norm}}(t) = \frac{\psi_n(t)}{\sqrt{\int |\psi_n(t)|^2 \mathrm{d}t}} \quad (5.37)$$

$$C_n' = C_n \sqrt{\int |\psi_n(t)|^2 \mathrm{d}t} \quad (5.38)$$

for C_n being one of the mode weights X_n or P_n. Thus, the product $C_n \psi_n(t) = C_n' \psi_n^{\mathrm{norm}}(t)$ remains constant but the mode is normalized, and enough information is gained from this gradient step (i.e. an increase or decrease in mode amplitude) to adjust the mode weight.

5.4 Results

We numerically simulated the generation of the OPA FROG spectrogram and retrieved the mode shapes and quadrature variances using our MMG-OPA-FROG algorithm, described above. We used the retrieval algorithm to extract the shape of modes, the variances in $\hat{x}$ and $\hat{p}$, and the relative angles of squeezing.

We numerically generated the spectrogram from a multimode squeezed state composed of 30-fs-long chirped Hermite Gaussian temporal modes, which are a good approximation for the modes that arise from a broadband OPA [41], using Eq. 5.23. The gating pulse is a mildly chirped 100-fs Gaussian pulse which amplifies the state by 50 dB. The results, after 10,000 iterations of the algorithm, are shown in Fig. 5.5. The loss, which is the root mean square distance between the simulated and recovered spectrograms normalized by the root mean square of the measured spectrogram, is 0.0026.

The mode fidelity of each mode, written as an inset in Figs. 5.5(d)-(g), which we define as the squared overlap between the actual and recovered modes as $|\int \mathrm{d}t\ \psi_n^*(t)\psi_n^{\mathrm{rec}}(t)|^2$,

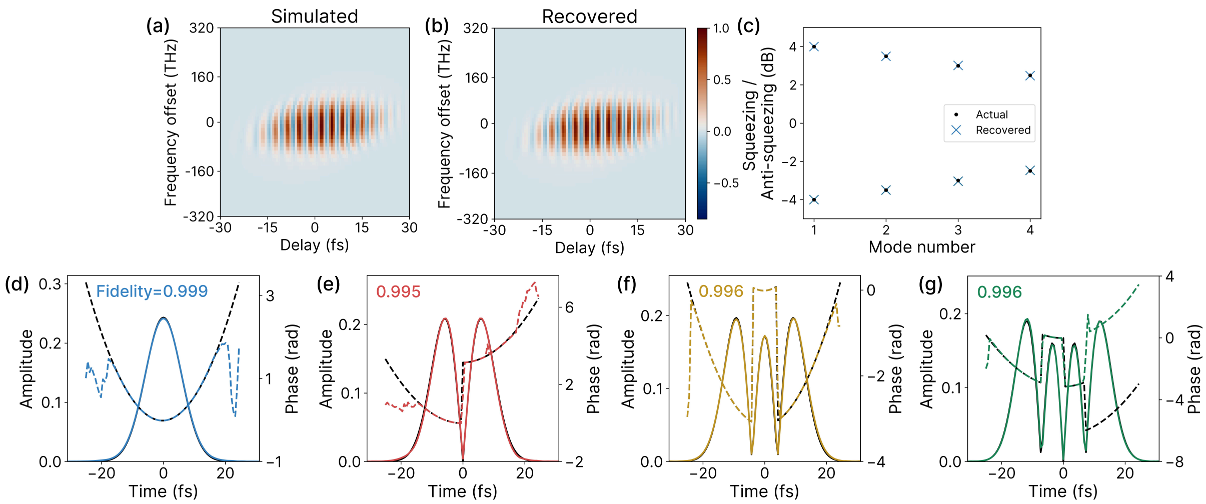

Figure 5.5: Simulated retrieval of an ultrafast multimode squeezed state using MMG-OPA-FROG algorithm using a 100-fs chirped Gaussian gating pulse. (a) Simulated spectrogram, normalized such that the peak value is 1. (b) Retrieved spectrogram, also normalized. The root mean square distance loss is 0.0026. (c) Plot of actual (black circles) and recovered (blue crosses) squeezing and anti-squeezing for each mode. (d)-(g) Recovered (colored) and actual (black) mode shapes, with the solid lines portraying amplitude and the dashed lines phase. The fidelity between the actual and recovered modes is written in each plot.

is above 0.995 for all modes. The amount of actual and recovered squeezing and anti-squeezing is shown in Fig. 5.5(c), with all recovered values falling within 2% of the actual values. All of these quantities indicate a successful reconstruction of the state. This demonstrates that the MMG-OPA-FROG algorithm can accurately recover both the temporal structure and quantum statistics of ultrafast multimode squeezed states directly from the measured spectrogram.

The algorithm can identify the relative phases, which is equivalent to the squeezing angles for a multimode squeezed state, which can be used to reconstruct the full covariance matrix. In the case of Fig. 5.5 the relative phases are zero.

We use the algorithm to extract the relative phase between the modes, which for squeezed vacuum allows us to determine the full covariance matrix with one of the squeezing modes as the reference for squeezing angle $\theta_s = 0$. We show the correspondence in Fig. 5.6(a) and the relative mode phase recovery for 2 modes in 5.6(b). The covariance as a function of the relative mode phase and the quadrature variances can be calculated as

$$\langle 2\hat{x}^2 \sin\theta_s \cos\theta_s - 2\hat{p}^2 \sin\theta_s \cos\theta_s \rangle. \tag{5.39}$$

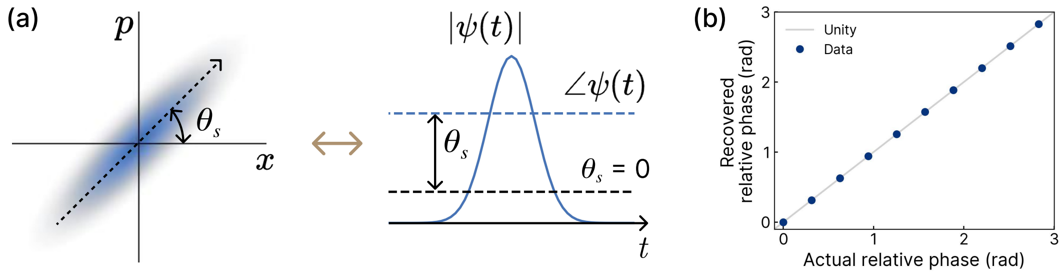

Figure 5.6: (a) Correspondence between the squeezing angle in phase space and the relative phase between a mode and a reference point (usually another mode). (b) The recovered relative phase between two modes vs. the actual relative phase. Unity (perfect reconstruction) is shown in gray.

We characterize the noise-tolerance of the algorithm by adding Gaussian noise to the simulated spectrogram to achieve various signal-to-noise ratios (SNRs) and characterizing the loss and mode fidelity, as shown in Fig. 5.7(a) and (b). We employ a zeroing mask over the data outside the significantly non-zero portion of the spectrogram so that the noise in the wings does not prevent convergence. In order to simulate a realistic recovery procedure, we use the common bootstrapping technique to generate the error bars from a single noisy spectrogram at each noise level [40]. We can see that the recovery decreases in effectiveness with higher noise, and that some retrievals fail (note the heavy tails of the fidelity distributions towards low fidelity for low SNR in Fig. 5.7(b)). These tails indicate that some retrievals fail, so we set a threshold of 10% loss for considering a state recovery successful, and the following plots are based on successful recoveries.

We show an example mode retrieval at an SNR of 15 dB in Figs. 5.7(c-h). The mode retrieval is slightly less successful than in the noiseless case, with the squeezing values in particular having a large variance. However, the average mode fidelities, shown in the insets of Figs. 5.7(f-h), are above 0.85, and the mode variances are within 10% of their actual values, showing that the mode shape reconstruction was successful even in the presence of noise.

5.5 Discussion

The experimental prospects for generating and characterizing a multimode squeezed state using MMG-OPA-FROG are promising. A potential setup to implement it is shown in Fig. 5.9. Multimode squeezed states have been generated and characterized using OPAs [2, 13, 42], and OPAs have been used as the nonlinear process in FROG setups for classical

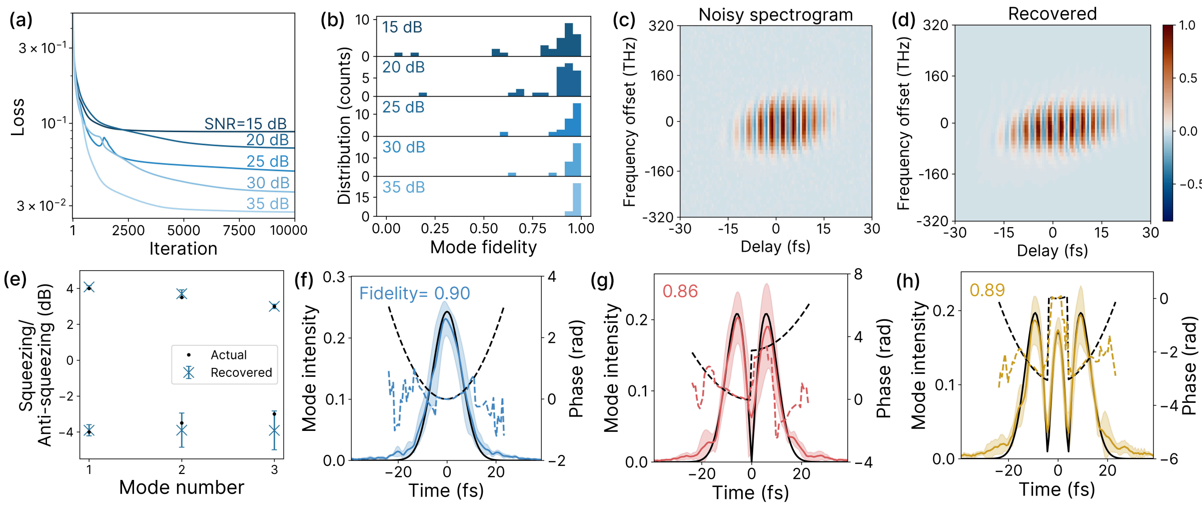

Figure 5.7: Performance of the algorithm in the presence of noise. (a) Loss vs. iteration number for different amounts of noise in the spectrogram. (b) Distributions of mode fidelity for different SNRs. (c) Example noisy spectrogram with 15 dB SNR. (d) Recovered spectrogram, with the noisy one as input. (e) Actual (dots) and recovered (crosses) squeezing and anti-squeezing values from the noisy spectrogram. (f-h) Recovered mode intensity (solid lines) and phase (dashed lines) from the noisy spectrogram, averaged over successful retrievals. The shaded region indicates one standard deviation, based on bootstrapping. The fidelity of the recovered mode with the actual mode is inset.

pulses [44, 46, 47]. OPAs with a broad bandwidth, which is necessary for the spectrogram to be in this form, are available in integrated photonics [17]. Furthermore, the length of the pump pulse does not limit the resolution of the reconstruction, within reason, and so the pump pulse can be any pulse that allows for broadband and high-gain operation of the OPA, lifting the pulse-shaping requirement present in homodyne detection.

One difficulty of implementing this state retrieval scheme is minimizing the loss between the state-generation and measurement OPA, so that the squeezing is maintained. One solution is putting both OPAs on one integrated photonic chip, which reduces loss and allows for significant squeezing to be measured [22]. Another potential difficulty lies in stabilizing the relative delay between the state and gating pulse, since the amplified state coming out of an OPA is very sensitive to the relative phase of the pulses and as such it must be very well stabilized. There are, however, techniques for calibrating the phase given instabilities [44].

Currently, except for the mode orthonormalization step, the computation time of the algorithm scales linearly with the number of modes and with the number of data points,

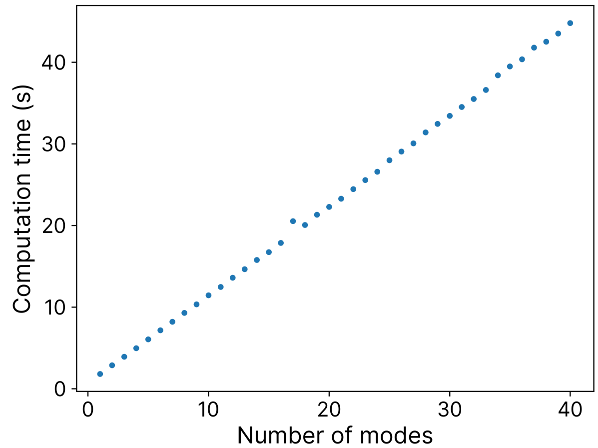

Figure 5.8: Retrieval time vs. number of modes in the retrieval.

since each data constraint and gradient descent step must be implemented mode-by-mode and data-point by data-point, leading to a scaling of $\mathcal{O}(MN_\omega N_\tau)$ for M the number of modes recovered, N_ω the number of frequency data points, and N_τ the number of delays measured. The mode orthonormalization, which is a Gram-Schmidt decomposition, scales as $\mathcal{O}(N_\omega M^2)$, but in practice up to $M = 40$ modes the linear factor dominates. We plot the computation time vs. the number of modes in the retrieval in Fig. 5.8 for 200 iterations each, with 64 points along both frequency and delay. The small fluctuations are likely due to other processes on the computer. For retrieving five modes using 10,000 iterations, twelve minutes are required on an Apple M1 processor with no GPU speedup. Due to the linear scaling, by optimizing the algorithm further and using dedicated hardware it may be possible to scale up the retrieval to a larger number of modes with a reasonable computation time.

Further work includes advancing the measurement scheme, including retrieving the covariance for arbitrary input states, which would grant us access to some information on non-Gaussian states [43]. To characterize non-Gaussian states fully, we require access to all of the statistics of the state, not just the second-order moments. If a single-shot spectrometer is available, it may be possible to perform full multimode state tomography [9].

5.6 Conclusion

In summary, we have proposed and numerically simulated the characterization of a multimode squeezed state using OPA FROG. We derived the OPA FROG spectrogram of a

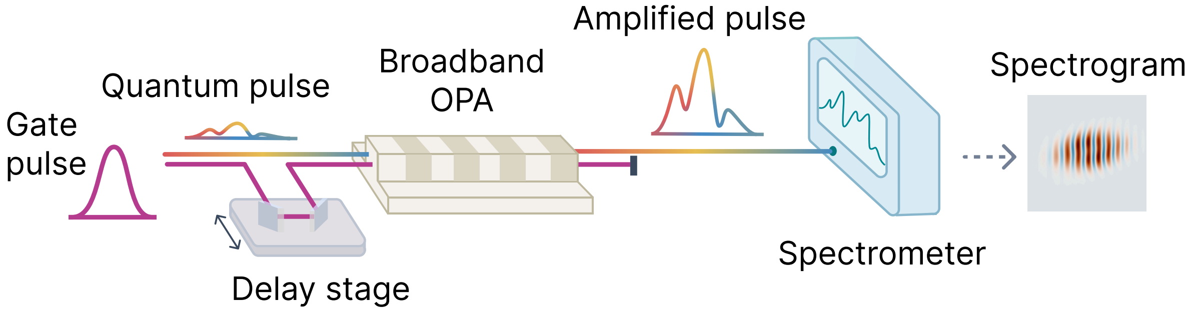

Figure 5.9: An experimental setup to measure the OPA FROG multimode spectrogram. The quantum pulse is amplified by a delayed gating pulse in a broadband high-gain OPA. The resulting amplified pulse is measured in a spectrometer and these spectra are combined to form the spectrogram $I(\omega, \tau)$.

multimode quantum state as a function of the second-order moments and mode shapes. We developed a multimode FROG algorithm to extract the mode shapes and $\hat{x}$ and $\hat{p}$ variances. This technique can be implemented using available experimental techniques and equipment, particularly the scalable platform of integrated photonics, and has the potential to characterize a wide range of mode shapes and states. Unlike existing techniques, MMG-OPA-FROG does not have demanding gating pump pulse requirements, and there are few limits on the range of wavelengths that can be characterized. There are no assumptions on the shapes of the modes or on the gating pulse, and the assumption that the OPA used in FROG is broadband and high-gain is consistent with current experiments. Thus, ultra-broadband multimode input states such as the ones generated using broadband OPAs themselves can be characterized and utilized more effectively.

The ability to characterize ultrafast temporally multimode Gaussian states is central to implementing an optical temporal-mode-based communication and computation system, since knowing the mode shapes is crucial for mode matching and manipulation. This technique is one possible tool in the toolbox of ultrafast optical temporal mode computing and communication.

References

[1] Warit Asavanant, Yu Shiozawa, Shota Yokoyama, Baramee Charoensombutamon, Hiroki Emura, Rafael N. Alexander, Shuntaro Takeda, Jun-ichi Yoshikawa, Nicolas C. Menicucci, Hidehiro Yonezawa, and Akira Furusawa. "Generation of time-domain-multiplexed two-dimensional cluster state". In: *Science* 366.6463 (Oct. 18, 2019), pp. 373–376. DOI: 10.1126/science.aay2645.

[2] Ismail Barakat, Mahmoud Kalash, Dennis Scharwald, Polina Sharapova, Norbert Lindlein, and Maria Chekhova. "Simultaneous measurement of multimode squeezing through multimode phase-sensitive amplification". In: *Optica Quantum* 3.1 (Feb. 25, 2025), pp. 36–44. DOI: 10.1364/OPTICAQ.524682.

[3] C. Bourassin-Bouchet and M.-E. Couprie. "Partially coherent ultrafast spectrography". In: *Nature Communications* 6.1 (Mar. 6, 2015), p. 6465. DOI: 10.1038/ncomms7465.

[4] B. Brecht, Dileep V. Reddy, C. Silberhorn, and M. G. Raymer. "Photon Temporal Modes: A Complete Framework for Quantum Information Science". In: *Physical Review X* 5.4 (Oct. 30, 2015), p. 041017. DOI: 10.1103/PhysRevX.5.041017.

[5] Y. Cai, J. Roslund, G. Ferrini, F. Arzani, X. Xu, C. Fabre, and N. Treps. "Multimode entanglement in reconfigurable graph states using optical frequency combs". In: *Nature Communications* 8.1 (June 6, 2017), p. 15645. DOI: 10.1038/ncomms15645.

[6] Lidice Cruz-Rodriguez, Diptesh Dey, Antonia Freibert, and Philipp Stammer. "Quantum phenomena in attosecond science". In: *Nature Reviews Physics* 6.11 (Nov. 2024), pp. 691–704. DOI: 10.1038/s42254-024-00769-2.

[7] Yujiro Eto, Mutsuo Nuriya, and Hideaki Kano. "Quantum frequency-resolved optical gating measurement for ultranarrow temporal correlation of twin beams". In: *Optica Quantum* 2.6 (Dec. 25, 2024), pp. 468–474. DOI: 10.1364/OPTICAQ.533469.

[8] C. Fabre and N. Treps. "Modes and states in quantum optics". In: *Reviews of Modern Physics* 92.3 (Sept. 10, 2020), p. 035005. DOI: 10.1103/RevModPhys.92.035005.

[9] Jano Gil-Lopez, Yong Siah Teo, Syamsundar De, Benjamin Brecht, Hyunseok Jeong, Christine Silberhorn, and Luis L. Sánchez-Soto. "Universal compressive tomography in the time-frequency domain". In: *Optica* 8.10 (Oct. 20, 2021), pp. 1296–1305. DOI: 10.1364/OPTICA.427645.

[10] Emanuel Hubenschmid and Guido Burkard. *Time-domain field correlation measurements enable tomography of highly multimode quantum states of light.* June 12, 2025. DOI: 10.48550/arXiv.2506.10483. arXiv: 2506.10483[quant-ph].

[11] Emanuel Hubenschmid, Thiago L. M. Guedes, and Guido Burkard. "Optical Time-Domain Quantum State Tomography on a Subcycle Scale". In: *Physical Review X* 14.4 (Nov. 5, 2024), p. 041032. DOI: 10.1103/PhysRevX.14.041032.

[12] Mahmoud Kalash and Maria V. Chekhova. "Wigner function tomography via optical parametric amplification". In: *Optica* 10.9 (Sept. 20, 2023), p. 1142. DOI: 10.1364/OPTICA.488697.

[13] Mahmoud Kalash, Ui-Nyung Han, Young-Sik Ra, and Maria V. Chekhova. *Efficient detection of spectrally multimode squeezed light through optical parametric amplification.* Aug. 6, 2025. DOI: 10.48550/arXiv.2508.04502. arXiv: 2508.04502[quant-ph].

[14] Aviv Karnieli, Paul-Alexis Mor, Charles Roques-Carmes, Eran Lustig, Jamison Sloan, Jelena Vučković, David A. B. Miller, and Shanhui Fan. *Variational processing of multimode squeezed light*. Sept. 20, 2025. DOI: 10.48550/arXiv.2509.16753. arXiv: 2509.16753[quant-ph].

[15] M. V. Larsen, J. E. Bourassa, S. Kocsis, J. F. Tasker, R. S. Chadwick, C. González-Arciniegas, J. Hastrup, C. E. Lopetegui-González, F. M. Miatto, A. Motamedi, R. Noro, G. Roeland, R. Baby, H. Chen, P. Contu, I. Di Luch, C. Drago, M. Giesbrecht, T. Grainge, I. Krasnokutska, M. Menotti, B. Morrison, C. Puviraj, K. Rezaei Shad, B. Hussain, J. McMahon, J. E. Ortmann, M. J. Collins, C. Ma, D. S. Phillips, M. Seymour, Q. Y. Tang, B. Yang, Z. Vernon, R. N. Alexander, and D. H. Mahler. “Integrated photonic source of Gottesman–Kitaev–Preskill qubits”. In: *Nature* 642.8068 (June 2025), pp. 587–591. DOI: 10.1038/s41586-025-09044-5.

[16] Mikkel V. Larsen, Xueshi Guo, Casper R. Breum, Jonas S. Neergaard-Nielsen, and Ulrik L. Andersen. “Deterministic generation of a two-dimensional cluster state”. In: *Science* 366.6463 (Oct. 18, 2019), pp. 369–372. DOI: 10.1126/science.aay4354.

[17] Luis Ledezma, Ryoto Sekine, Qiushi Guo, Rajveer Nehra, Saman Jahani, and Alireza Marandi. “Intense optical parametric amplification in dispersion-engineered nanophotonic lithium niobate waveguides”. In: *Optica* 9.3 (Mar. 20, 2022), p. 303. DOI: 10.1364/OPTICA.442332.

[18] Anthony Leverrier and Philippe Grangier. “Unconditional Security Proof of Long-Distance Continuous-Variable Quantum Key Distribution with Discrete Modulation”. In: *Physical Review Letters* 102.18 (May 6, 2009), p. 180504. DOI: 10.1103/PhysRevLett.102.180504.

[19] A. I. Lvovsky. “Continuous-variable optical quantum-state tomography”. In: *Reviews of Modern Physics* 81.1 (2009), pp. 299–332. DOI: 10.1103/RevModPhys.81.299.

[20] Nicolas C. Menicucci. “Fault-Tolerant Measurement-Based Quantum Computing with Continuous-Variable Cluster States”. In: *Physical Review Letters* 112.12 (Mar. 26, 2014), p. 120504. DOI: 10.1103/PhysRevLett.112.120504.

[21] Nicolas C. Menicucci, Peter Van Loock, Mile Gu, Christian Weedbrook, Timothy C. Ralph, and Michael A. Nielsen. “Universal Quantum Computation with Continuous-Variable Cluster States”. In: *Physical Review Letters* 97.11 (Sept. 13, 2006), p. 110501. DOI: 10.1103/PhysRevLett.97.110501.

[22] Rajveer Nehra, Ryoto Sekine, Luis Ledezma, Qiushi Guo, Robert M. Gray, Arkadev Roy, and Alireza Marandi. “Few-cycle vacuum squeezing in nanophotonics”. In: *Science* 377.6612 (Sept. 16, 2022), pp. 1333–1337. DOI: 10.1126/science.abo6213.

[23] Edwin Ng, Ryotatsu Yanagimoto, Marc Jankowski, M. M. Fejer, and Hideo Mabuchi. *Quantum noise dynamics in nonlinear pulse propagation.* July 11, 2023. arXiv: 2307.05464[physics,physics:quant-ph].

[24] Jeremy L. O'Brien. "Optical Quantum Computing". In: *Science* 318.5856 (Dec. 7, 2007), pp. 1567–1570. DOI: 10.1126/science.1142892.

[25] S. Pirandola, U. L. Andersen, L. Banchi, M. Berta, D. Bunandar, R. Colbeck, D. Englund, T. Gehring, C. Lupo, C. Ottaviani, J. L. Pereira, M. Razavi, J. Shamsul Shaari, M. Tomamichel, V. C. Usenko, G. Vallone, P. Villoresi, and P. Wallden. "Advances in quantum cryptography". In: *Advances in Optics and Photonics* 12.4 (Dec. 31, 2020), pp. 1012–1236. DOI: 10.1364/AOP.361502.

[26] C. Polycarpou. "Adaptive Detection of Arbitrarily Shaped Ultrashort Quantum Light States". In: *Physical Review Letters* 109.5 (2012). DOI: 10.1103/PhysRevLett.109.053602.

[27] T. C. Ralph. "Continuous variable quantum cryptography". In: *Physical Review A* 61.1 (Dec. 8, 1999), p. 010303. DOI: 10.1103/PhysRevA.61.010303.

[28] C. Riek, P. Sulzer, M. Seeger, A. S. Moskalenko, G. Burkard, D. V. Seletskiy, and A. Leitenstorfer. "Subcycle quantum electrodynamics". In: *Nature* 541.7637 (Jan. 2017), pp. 376–379. DOI: 10.1038/nature21024.

[29] Jonathan Roslund, Renné Medeiros de Araújo, Shifeng Jiang, Claude Fabre, and Nicolas Treps. "Wavelength-multiplexed quantum networks with ultrafast frequency combs". In: *Nature Photonics* 8.2 (Feb. 2014), pp. 109–112. DOI: 10.1038/nphoton.2013.340.

[30] Laura Serino, Jano Gil-Lopez, Michael Stefszky, Raimund Ricken, Christof Eigner, Benjamin Brecht, and Christine Silberhorn. "Realization of a Multi-Output Quantum Pulse Gate for Decoding High-Dimensional Temporal Modes of Single-Photon States". In: *PRX Quantum* 4.2 (Apr. 12, 2023), p. 020306. DOI: 10.1103/PRXQuantum.4.020306.

[31] Laura Serino, Markus Rambach, Benjamin Brecht, Jacquiline Romero, and Christine Silberhorn. "Self-guided tomography of time-frequency qudits". In: *Quantum Science and Technology* 10.2 (Apr. 1, 2025), p. 025024. DOI: 10.1088/2058-9565/adb0ea.

[32] Laura Serino, Werner Ridder, Abhinandan Bhattacharjee, Jano Gil-Lopez, Benjamin Brecht, and Christine Silberhorn. "Orchestrating time and color: a programmable source of high-dimensional entanglement". In: *Optica Quantum* 2.5 (Oct. 25, 2024), pp. 339–345. DOI: 10.1364/OPTICAQ.532334.

[33] Laura Serino, Werner Ridder, Abhinandan Bhattacharjee, Jano Gil-Lopez, Benjamin Brecht, and Christine Silberhorn. "Orchestrating time and color: a programmable source of high-dimensional entanglement". In: *Optica Quantum* 2.5 (Oct. 25, 2024), pp. 339–345. DOI: 10.1364/OPTICAQ.532334.

[34] Yaakov Shaked, Yoad Michael, Rafi Z. Vered, Leon Bello, Michael Rosenbluh, and Avi Pe'er. "Lifting the bandwidth limit of optical homodyne measurement with broadband parametric amplification". In: *Nature Communications* 9.1 (Feb. 9, 2018), p. 609. DOI: 10.1038/s41467-018-03083-5.

[35] Kan Takase, Masanori Okada, Takahiro Serikawa, Shuntaro Takeda, Jun-ichi Yoshikawa, and Akira Furusawa. "Complete temporal mode characterization of non-Gaussian states by a dual homodyne measurement". In: *Physical Review A* 99.3 (Mar. 18, 2019), p. 033832. DOI: 10.1103/PhysRevA.99.033832.

[36] J Tiedau, V S Shchesnovich, D Mogilevtsev, V Ansari, G Harder, T J Bartley, N Korolkova, and Ch Silberhorn. "Quantum state and mode profile tomography by the overlap". In: *New Journal of Physics* 20.3 (Mar. 2018), p. 033003. DOI: 10.1088/1367-2630/aaad8a.

[37] Rick Trebino. *Frequency-Resolved Optical Gating: The Measurement of Ultrashort Laser Pulses*. Boston, MA: Springer US, 2000. DOI: 10.1007/978-1-4615-1181-6.

[38] Matan Even Tzur, Chen Mor, Noa Yaffe, Michael Birk, Andrei Rasputnyi, Omer Kneller, Ido Nisim, Ido Kaminer, Maria Chekhova, Michael Krueger, Misha Ivanov, Nirit Dudovich, and Oren Cohen. *Attosecond-resolved quantum fluctuations of light and matter*. Nov. 23, 2025. DOI: 10.48550/arXiv.2511.18362. arXiv: 2511.18362[physics].

[39] Matan Even Tzur, Chen Mor, Noa Yaffe, Michael Birk, Andrei Rasputnyi, Omer Kneller, Ido Nisim, Ido Kaminer, Michael Krüger, Nirit Dudovich, and Oren Cohen. *Measuring and controlling the birth of quantum attosecond pulses*. Feb. 13, 2025. DOI: 10.48550/arXiv.2502.09427. arXiv: 2502.09427[physics].

[40] Ziyang Wang, Erik Zeek, Rick Trebino, and Paul Kvam. "Beyond error bars: Understanding uncertainty in ultrashort-pulse frequency-resolved-optical-gating measurements in the presence of ambiguity". In: *Optics Express* 11.26 (Dec. 29, 2003), p. 3518. DOI: 10.1364/OE.11.003518.

[41] Wojciech Wasilewski, A. I. Lvovsky, Konrad Banaszek, and Czesław Radzewicz. "Pulsed squeezed light: Simultaneous squeezing of multiple modes". In: *Physical Review A* 73.6 (June 20, 2006), p. 063819. DOI: 10.1103/PhysRevA.73.063819.

[42] James Williams, Elina Sendonaris, Rajveer Nehra, Robert M. Gray, Ryoto Sekine, Luis Ledezma, and Alireza Marandi. "Ultrafast all-optical measurement of squeezed vacuum in a lithium niobate nanophotonic circuit". In: *Physical Review Research* 7.4 (Oct. 1, 2025), p. 043006. DOI: 10.1103/rvmb-ljd3.

[43] Geehyun Yang, Matthias Kizmann, Alfred Leitenstorfer, and Andrey S. Moskalenko. *Subcycle tomography of quantum light*. July 24, 2023. DOI: 10.48550/arXiv.2307.12812. arXiv: 2307.12812[quant-ph].

[44] Thomas Zacharias, Robert Gray, Ryoto Sekine, James Williams, Selina Zhou, and Alireza Marandi. "Energy-Efficient Ultrashort-Pulse Characterization Using Nanophotonic Parametric Amplification". In: *ACS Photonics* 12.3 (Mar. 19, 2025), pp. 1316–1320. DOI: 10.1021/acsphotonics.4c02620.

[45] Thomas Zacharias, Elina Sendonaris, Robert Gray, James Williams, Ryoto Sekine, Maximilian Shen, Selina Zhou, and Alireza Marandi. *Quantum Frequency Resolved Optical Gating of Few-Cycle Squeezed Vacuum*. Apr. 8, 2026. DOI: 10.48550/arXiv.2604.07637. arXiv: 2604.07637[physics.optics].

[46] Jing-Yuan Zhang, Chao-Kuei Lee, J. Y. Huang, and Ci-Ling Pan. "Sub femto-joule sensitive single-shot OPA-XFROG and its application in study of white-light supercontinuum generation". In: *Optics Express* 12.4 (Feb. 23, 2004), pp. 574–581. DOI: 10.1364/OPEX.12.000574.

[47] Jing-yuan Zhang, Aparna Shreenath, Mark Kimmel, Erik Zeek, Rick Trebino, and Stephan Link. "Measurement of the intensity and phase of attojoule femtosecond light pulses using Optical-Parametric-Amplification Cross-Correlation Frequency-Resolved Optical Gating". In: *Optics Express* 11.6 (Mar. 24, 2003), p. 601. DOI: 10.1364/OE.11.000601.

[48] Han-Sen Zhong, Hui Wang, Yu-Hao Deng, Ming-Cheng Chen, Li-Chao Peng, Yi-Han Luo, Jian Qin, Dian Wu, Xing Ding, Yi Hu, Peng Hu, Xiao-Yan Yang, Wei-Jun Zhang, Hao Li, Yuxuan Li, Xiao Jiang, Lin Gan, Guangwen Yang, Lixing You, Zhen Wang, Li Li, Nai-Le Liu, Chao-Yang Lu, and Jian-Wei Pan. "Quantum computational advantage using photons". In: *Science* 370.6523 (Dec. 18, 2020), pp. 1460–1463. DOI: 10.1126/science.abe8770.

Chapter 6

OUTLOOK

In this chapter, we will discuss future directions in nonlinear quantum optics, and quantum optics in general, with additional technological and theoretical innovations. Here we will focus on the goals of improving sensing, communication, and computation and in particular focus on integrated platforms. As mentioned in Chapter 1, many of these goals can be achieved using quantum light, and scaling these operations up is imperative for achieving an undeniable quantum advantage. This thesis explored some methods of overcoming the electronic measurement bottleneck using integrated nonlinear photonics, which may help with lifting the scaling limit of time- and mode-multiplexed quantum optical systems. These systems are of interest because they have already seen success in large-scale entangled state generation [2, 9] and quantum operations [1, 10] while maintaining a constant physical overhead, and large entangled states are imperative for achieving fault-tolerant quantum information processing. A fast measurement of quantum light may also be beneficial for increasing the operating speed of matter-based quantum systems such as neutral atoms and trapped ions and increasing the number of operations possible before the qubits decohere. For these reasons, lifting the bandwidth limitation on quantum optical measurement has broad-reaching implications across quantum technologies.

6.1 Quantum optical information processing

Looking forward, quantum optical computing and information processing has a few advantages over other quantum computation schemes such as superconducting qubits and trapped ions and atoms, namely, room-temperature operation, ultra-broad available bandwidths, and ready integration with quantum communication systems. Optical quantum computations can also take advantage of the reconfigurability of entanglement and long-range entanglement available to optical time-, temporal mode-, and frequency-bin-multiplexed systems. The downsides are the low nonlinear interaction rates, which leads to an increased difficulty of performing deterministic non-Gaussian operations, and the difficulty of storing information in light. In order for quantum photonics to be a viable alternative to matter-based qubits and qudits, these issues must be addressed, and the benefits must be taken advantage of.

Large-scale entangled states

In terms of large-scale entangled state generation, implementation in the time-multiplexed regime will be improved by multiplexing shorter pulses, as current implementations are limited by the phase coherence time [2, 9]. For example, the temporal widths of the modes in those works is of the order of tens or hundreds of nanoseconds, limited by the bandwidth of their OPO squeezed light source, while squeezed pulses from our OPAs are hundreds of femtoseconds wide, which offers an increase in the number of modes of five orders of magnitude if the full bandwidth is taken advantage of.

Furthermore, performing operations on multimode ultrafast quantum optical states in the temporal mode basis offers a convenient way to generate large and high-dimensional entangled states simply by changing the measurement basis. This is similar to what has been done in frequency-bin cluster states, since the principal mode basis is some superposition of these frequency bins [16]. Mode-selective photon subtraction, an essential building block for any CV quantum optical system, has already been implemented [14], and multi-output quantum pulse gates have been created that separate the modes for better mode-selective operations [17]. Arbitrarily selecting modes for light generation would also increase the capabilities in the spectrotemporal mode basis, and work has been done on this using dispersion engineering and pump pulse shaping [18]. Combining time- and temporal mode-multiplexing with feedback locking for phase stability could provide the possibility for high-dimensional and indefinitely large entangled state generation. The phase stability of integrated photonic chips makes them an attractive alternative to free-space setups. The use case for these states is MBQC [15], a particularly popular scheme in quantum optics due to the convenience and benefits of separating the entangling gates from the single-mode operations. The ability to use time as a dimension sets light apart in terms of scalability from other quantum systems, and ultrafast ultra-broadband photonics may offer a way to push those abilities even farther.

Fault-tolerant quantum optical computing

Using CV cluster states combined with Gottesman-Kitaev-Preskill (GKP) states for fault-tolerant quantum computing has been a topic of recent interest. For topological fault-tolerance through error correction, a three-dimensional cluster state is necessary [12]. One lower limit on the required squeezing to achieve this regime is 12.7 dB [8], which also requires the use of GKP states as the non-Gaussian resource. The greatest measured squeezing in a CV cluster state to date has been 5 dB [24]. Improving squeezing in cluster states, achieving deterministic non-Gaussian operation (such as generating GKP states), and increasing the dimensionality of cluster states to surpass the fault-tolerant limit is therefore of utmost importance for achieving fault-tolerant CV quantum optical computation.

One way to mitigate the difficulty of performing a non-Gaussian operation is to improve the nonlinearity-to-loss rate, as mentioned in Chapter 3. Improving this rate opens the door to non-Gaussian operation of an OPA by entangling the pump with the signal, accessing the true quantum nature of the pump term in the PDC Hamiltonian, making it a cubic Hamiltonian and thus capable of generating non-Gaussian states [21, 22]. One route to achieving this regime is to raise the gain by concentrating the OPA gain in a single mode [6, 13] or by using another pulse to create single-mode dynamics [23], but these require precise dispersion engineering beyond current fabrication capabilities on integrated platforms. Another route is to lower the loss in the system. TFLN seems to be an ideal platform for achieving high-gain amplification due to the low dispersion allowing for extremely high peak power ultrashort pulses without damaging the chip and its high $\chi^{(2)}$, but the sidewall roughness is putting a lower limit on the loss possible, and further engineering is necessary in order to achieve the strong coupling regime ($g/\kappa \approx 1$). Another direction that is being taken is to multiplex many probabilistic non-Gaussian operations to increase the odds of success [3, 7].

6.2 Integrated quantum photonics

In general, experimental limitations to integrated TFLN quantum photonics arise from allowing vacuum to mix in with the quantum states. The sidewall roughness of integrated nanophotonic ridge waveguides, such as the ones considered in this thesis, imposes a continuous loss over the waveguide. The phase noise of the laser mixes the anti-squeezed quadratures in with the squeezed quadratures, and the fabrication imperfections of integrated photonic devices often leads to unnecessary loss on-chip. Furthermore, outcoupling from the chip imposes even more loss, typically over 3 dB, which would destroy any Wigner negativity. Thus, moving all sensitive quantum operations on-chip and amplifying before the outcoupling is necessary. Integrating single-photon detectors onto TFLN can bypass the outcoupling loss issue for detecting photons generated on-chip [19]. Integrating photodetectors onto silicon [11] and TFLN [4] removes the outcoupling loss for other forms of light and, in some cases [11], allows for an ultra-broad photodetector bandwidth. Integrated mode-locked lasers may help overcome the large energy consumption associated with tabletop lasers [5].

One of the main challenges to scaling TFLN chips up to larger circuits, even though functional integrated devices are common, is the difficulty of simultaneously phase-matching multiple devices on-chip due to poling and thin-film thickness imperfections. The dispersion profile of the waveguide is extremely sensitive to the thin-film thickness and waveguide dimensions, and achieving phase-matching over an entire circuit becomes exponentially harder with the number of devices in it. For these reasons, even though integrated photonics on TFLN offers much promise due to high nonlinear efficiency, bandwidth, and fabrication scalability, progress must be made on the fabrication techniques and technology to achieve the platform's full potential.

To mitigate some of each material's specific downsides, heterogeneous material integration allows for combining multiple materials in order to take advantage most fully of the benefits of each [25]. New materials beyond silicon and LN are also being explored, such as lithium tantalate for its low birefringence and higher damage threshold [20] and LN-on-sapphire for its mid-IR absorption properties [26].

There are many approaches to overcoming the limitations of quantum light generation, manipulation, and measurement, and it is likely that a functioning large-scale useful quantum computer will require a combination of them. The progress being made in the design, fabrication, and theory of integrated photonics represents a small fraction of current efforts to better control quantum light, but the improvements that have already been seen on these platforms indicate that the integrated approach has immense promise that has not yet been accessed.

References

[1] Warit Asavanant, Baramee Charoensombutamon, Shota Yokoyama, Takeru Ebihara, Tomohiro Nakamura, Rafael N. Alexander, Mamoru Endo, Jun-ichi Yoshikawa, Nicolas C. Menicucci, Hidehiro Yonezawa, and Akira Furusawa. "Time-Domain-Multiplexed Measurement-Based Quantum Operations with 25-MHz Clock Frequency". In: *Physical Review Applied* 16.3 (Sept. 2, 2021), p. 034005. DOI: 10.1103/PhysRevApplied.16.034005.

[2] Warit Asavanant, Yu Shiozawa, Shota Yokoyama, Baramee Charoensombutamon, Hiroki Emura, Rafael N. Alexander, Shuntaro Takeda, Jun-ichi Yoshikawa, Nicolas C. Menicucci, Hidehiro Yonezawa, and Akira Furusawa. "Generation of time-domain-multiplexed two-dimensional cluster state". In: *Science* 366.6463 (Oct. 18, 2019), pp. 373–376. DOI: 10.1126/science.aay2645.

[3] Sara Bartolucci, Patrick Birchall, Hector Bombín, Hugo Cable, Chris Dawson, Mercedes Gimeno-Segovia, Eric Johnston, Konrad Kieling, Naomi Nickerson, Mi-

hir Pant, Fernando Pastawski, Terry Rudolph, and Chris Sparrow. “Fusion-based quantum computation”. In: *Nature Communications* 14.1 (Feb. 17, 2023), p. 912. DOI: 10.1038/s41467-023-36493-1.

[4] Boris Desiatov and Marko Lončar. “Silicon photodetector for integrated lithium niobate photonics”. In: *Applied Physics Letters* 115.12 (Sept. 20, 2019), p. 121108. DOI: 10.1063/1.5118901.

[5] Qiushi Guo, Benjamin K. Gutierrez, Ryoto Sekine, Robert M. Gray, James A. Williams, Luis Ledezma, Luis Costa, Arkadev Roy, Selina Zhou, Mingchen Liu, and Alireza Marandi. “Ultrafast mode-locked laser in nanophotonic lithium niobate”. In: *Science* 382.6671 (Nov. 10, 2023), pp. 708–713. DOI: 10.1126/science.adj5438.

[6] Martin Houde, Liam Beaudoin, Robert Kwolek, Kazuki Hirota, Rajveer Nehra, and Nicolás Quesada. “Ultrashort-pulse-pumped, single-mode type-0 squeezers in lithium niobate nanophotonics”. In: *Optica Quantum* 3.6 (2025), pp. 560–568.

[7] M. V. Larsen, J. E. Bourassa, S. Kocsis, J. F. Tasker, R. S. Chadwick, C. González-Arciniegas, J. Hastrup, C. E. Lopetegui-González, F. M. Miatto, A. Motamedi, R. Noro, G. Roeland, R. Baby, H. Chen, P. Contu, I. Di Luch, C. Drago, M. Giesbrecht, T. Grainge, I. Krasnokutska, M. Menotti, B. Morrison, C. Puviraj, K. Rezaei Shad, B. Hussain, J. McMahon, J. E. Ortmann, M. J. Collins, C. Ma, D. S. Phillips, M. Seymour, Q. Y. Tang, B. Yang, Z. Vernon, R. N. Alexander, and D. H. Mahler. “Integrated photonic source of Gottesman–Kitaev–Preskill qubits”. In: *Nature* 642.8068 (June 2025), pp. 587–591. DOI: 10.1038/s41586-025-09044-5.

[8] Mikkel V. Larsen, Christopher Chamberland, Kyungjoo Noh, Jonas S. Neergaard-Nielsen, and Ulrik L. Andersen. “Fault-Tolerant Continuous-Variable Measurement-based Quantum Computation Architecture”. In: *PRX Quantum* 2.3 (Aug. 11, 2021), p. 030325. DOI: 10.1103/PRXQuantum.2.030325.

[9] Mikkel V. Larsen, Xueshi Guo, Casper R. Breum, Jonas S. Neergaard-Nielsen, and Ulrik L. Andersen. “Deterministic generation of a two-dimensional cluster state”. In: *Science* 366.6463 (Oct. 18, 2019), pp. 369–372. DOI: 10.1126/science.aay4354.

[10] Mikkel V. Larsen, Xueshi Guo, Casper R. Breum, Jonas S. Neergaard-Nielsen, and Ulrik L. Andersen. “Deterministic multi-mode gates on a scalable photonic quantum computing platform”. In: *Nature Physics* 17.9 (Sept. 2021), pp. 1018–1023. DOI: 10.1038/s41567-021-01296-y.

[11] S. Lischke, A. Peczek, J. S. Morgan, K. Sun, D. Steckler, Y. Yamamoto, F. Korndörfer, C. Mai, S. Marschmeyer, M. Fraschke, A. Krüger, A. Beling, and L. Zimmermann. “Ultra-fast germanium photodiode with 3-dB bandwidth of 265 GHz”. In: *Nature Photonics* 15.12 (Dec. 2021), pp. 925–931. DOI: 10.1038/s41566-021-00893-w.

[12] Nicolas C. Menicucci. "Fault-Tolerant Measurement-Based Quantum Computing with Continuous-Variable Cluster States". In: *Physical Review Letters* 112.12 (Mar. 26, 2014), p. 120504. DOI: 10.1103/PhysRevLett.112.120504.

[13] Shivam Mundhra, Elina Sendonaris, Robert M. Gray, James Williams, and Alireza Marandi. *Optimizing for a Near Single-Mode Type-0 Optical Parametric Amplifier in Nanophotonics*. Jan. 6, 2025. DOI: 10.48550/arXiv.2412.07004. arXiv: 2412.07004[physics.optics].

[14] Young-Sik Ra, Adrien Dufour, Mattia Walschaers, Clément Jacquard, Thibault Michel, Claude Fabre, and Nicolas Treps. "Non-Gaussian quantum states of a multimode light field". In: *Nature Physics* 16.2 (Feb. 2020), pp. 144–147. DOI: 10.1038/s41567-019-0726-y.

[15] Robert Raussendorf and Hans J. Briegel. "A One-Way Quantum Computer". In: *Physical Review Letters* 86.22 (May 28, 2001), pp. 5188–5191. DOI: 10.1103/PhysRevLett.86.5188.

[16] Chan Roh, Geunhee Gwak, Young-Do Yoon, and Young-Sik Ra. "Generation of three-dimensional cluster entangled state". In: *Nature Photonics* 19.5 (May 2025), pp. 526–532. DOI: 10.1038/s41566-025-01631-2.

[17] Laura Serino, Jano Gil-Lopez, Michael Stefszky, Raimund Ricken, Christof Eigner, Benjamin Brecht, and Christine Silberhorn. "Realization of a Multi-Output Quantum Pulse Gate for Decoding High-Dimensional Temporal Modes of Single-Photon States". In: *PRX Quantum* 4.2 (Apr. 12, 2023), p. 020306. DOI: 10.1103/PRXQuantum.4.020306.

[18] Laura Serino, Werner Ridder, Abhinandan Bhattacharjee, Jano Gil-Lopez, Benjamin Brecht, and Christine Silberhorn. "Orchestrating time and color: a programmable source of high-dimensional entanglement". In: *Optica Quantum* 2.5 (Oct. 25, 2024), pp. 339–345. DOI: 10.1364/OPTICAQ.532334.

[19] Sjoerd Telkamp, Odiel Hooybergs, Myriam Rihani, Giovanni Finco, Tummas Napoleon Arge, Robin N. Dür, Victor Mougel, Daniel Scheffler, Filip Krizek, Rachel Grange, Robert J. Chapman, and Werner Wegscheider. *High-temperature growth of ultra thin NbTiN films on lithium niobate for integrated single photon detection*. Version Number: 1. 2025. DOI: 10.48550/ARXIV.2509.07870.

[20] Chengli Wang, Zihan Li, Johann Riemensberger, Grigory Lihachev, Mikhail Churaev, Wil Kao, Xinru Ji, Junyin Zhang, Terence Blesin, Alisa Davydova, Yang Chen, Kai Huang, Xi Wang, Xin Ou, and Tobias J. Kippenberg. "Lithium tantalate photonic integrated circuits for volume manufacturing". In: *Nature* 629.8013 (May 2024), pp. 784–790. DOI: 10.1038/s41586-024-07369-1.

[21] Ryotatsu Yanagimoto, Rajveer Nehra, Ryan Hamerly, Edwin Ng, Alireza Marandi, and Hideo Mabuchi. "Quantum Nondemolition Measurements with Optical Parametric Amplifiers for Ultrafast Universal Quantum Information Processing". In:

PRX Quantum 4.1 (Mar. 29, 2023), p. 010333. DOI: 10.1103/PRXQuantum.4.010333.

[22] Ryotatsu Yanagimoto, Rajveer Nehra, Edwin Ng, Alireza Marandi, and Hideo Mabuchi. *Engineering cubic quantum nondemolition Hamiltonian with mesoscopic optical parametric interactions.* May 4, 2023. arXiv: 2305.03260[physics,physics:quant-ph].

[23] Ryotatsu Yanagimoto, Edwin Ng, Marc Jankowski, Hideo Mabuchi, and Ryan Hamerly. "Temporal trapping: a route to strong coupling and deterministic optical quantum computation". In: *Optica* 9.11 (Nov. 20, 2022), pp. 1289–1296. DOI: 10.1364/OPTICA.473276.

[24] Shota Yokoyama, Ryuji Ukai, Seiji C. Armstrong, Chanond Sornphiphatphong, Toshiyuki Kaji, Shigenari Suzuki, Jun-ichi Yoshikawa, Hidehiro Yonezawa, Nicolas C. Menicucci, and Akira Furusawa. "Ultra-large-scale continuous-variable cluster states multiplexed in the time domain". In: *Nature Photonics* 7.12 (Dec. 2013). Number: 12, pp. 982–986. DOI: 10.1038/nphoton.2013.287.

[25] Can Yu, Meng Zhang, Lei Liang, Li Qin, Yongyi Chen, Yuxin Lei, Yubing Wang, Yue Song, Cheng Qiu, Peng Jia, Dabing Li, and Lijun Wang. "Advancements in transfer printing techniques and their applications in photonic integrated circuits". In: *Light: Science & Applications* 14.1 (Dec. 5, 2025), p. 396. DOI: 10.1038/s41377-025-02064-w.

[26] Selina Zhou, Maximilian Shen, Ryoto Sekine, Nicolas Englebert, Thomas Zacharias, Benjamin Gutierrez, Robert M. Gray, Justin Widjaja, and Alireza Marandi. *Quadratic Supercontinuum Generation from UV to Mid-IR in Lithium Niobate Nanophotonics.* version: 1. Oct. 21, 2025. DOI: 10.48550/arXiv.2510.18844. arXiv: 2510.18844[physics.optics].